Short-pulse propagation in fiber optical parametric amplifiers

Ph.D. Thesis
Valentina Cristofori

July 14th, 2013

DTU Fotonik
Department of Photonics Engineering

DTU Fotonik
Department of Photonics Engineering
Technical University of Denmark
Ørsteds Plads 345A
DK-2800 Kgs. Lyngby
Denmark

Contents

Preface **vii**

Acknowledgements **ix**

Abstract **xi**

Resumé (Danish abstract) **xiii**

PhD publication list **xv**

1 Introduction **1**
1.1 Thesis contributions and structure 4

2 Fiber Optical Parametric Amplification **7**
2.1 Introduction 7
2.2 Nonlinearities in Optical Fibers 8
2.2.1 Fiber Nonlinear Coefficient 9
2.3 Four-Wave Mixing 11
2.3.1 Propagation Constant 13
2.4 Single-Pump FOPAs 15
2.4.1 Coupled Amplitude Equations 15
2.4.2 Phase Matching 17
2.4.3 Modulation Instability 19
2.4.4 Parametric Gain and Amplification Bandwidth . . . 19
2.5 Stimulated Brillouin Scattering 30
2.6 Stimulated Raman Scattering 33
2.7 Summary 35

3 Intensity Modulation Transfer in Single-Pump Phase-

Insensitive FOPAs **37**
3.1 Introduction 37
3.2 Noise Figure and Intensity Modulation Transfer in Single-Pump Phase-Insensitive FOPA 38
3.3 Low-Frequency Intensity Modulation Transfer 42
3.3.1 Theory 43
3.3.2 Experimental Investigation of the Low-Frequency Pump-to-Signal Intensity Modulation Transfer . . . 44
3.4 Saturated FOPA 48
3.5 Experimental Investigation of Saturation Effects on IMT . . 52
3.6 Summary 59

4 Short-Pulse Generation in an All-Fiber Laser Source **61**
4.1 Introduction 61
4.2 Mode-Locking and Q-Switched mode-locking in Fast Saturable Absorbers 62
4.3 Figure-of-Eight Laser 66
4.3.1 Nonlinear amplifying loop mirror 67
4.4 Experimental Setups 68
4.4.1 Q-Switched Mode-Locked F8L 68
4.4.2 Mode-Locked F8L 75
4.5 Summary 80

5 Short-Pulse Propagation in Single-Pump Phase-Insensitive FOPAs **83**
5.1 Introduction 83
5.2 Optical Parametric Chirped Pulse Amplification 84
5.3 Dynamic Characterization of FOPCPAs 85
5.3.1 Numerical Characterization 86
5.3.2 Experimental Characterization 90
5.4 Amplification of 400 fs Pulses in FOPCPA 95
5.5 Summary 97

6 Conclusion **99**
6.1 Future developments 102

A Network Analyzer: Two-Port S-Parameters **105**
A.1 S-parameters matrix 105
A.2 Modulation index calculation 106

Acronyms **109**

Bibliography **112**

Preface

The work presented in this Thesis was carried out as a part of my Ph.D. project in the period April 14th, 2010 to July 14th, 2013. The work took place at DTU Fotonik (Technical University of Denmark, Department of Photonics Engineering).

The Ph.D. project was financed by the Danish Research Council for Technology and Production Sciences and supervised by

- Karsten Rottwitt (main supervisor), Professor, DTU Fotonik, Technical University of Denmark, Kgs. Lyngby, Denmark
- Christophe Peucheret (co-supervisor), Associate Professor, DTU Fotonik, Technical University of Denmark, Kgs. Lyngby, Denmark
- Michael Galili (co-supervisor), Associate Professor, DTU Fotonik, Technical University of Denmark, Kgs. Lyngby, Denmark

Acknowledgements

So many people took part to this project, directly or not, and I want to thank them all from the deepest of my heart.

At first, I would like to thank my supervisors **Karsten Rottwitt**, **Christophe Peucheret** and **Michael Galili** for giving me the opportunity to work at DTU Fotonik as a Ph.D. student, for always supporting me and for helping me with their advices. Without their patience, their kindness and their brilliant intuitions, everything would have been much more difficult.

I want to thank **Zohreh Lali-Dastjerdi**, for her support and brilliant suggestions during the last three years. It has been a pleasure to share with you this work as well as this life experience.

My sincere gratitude goes to **Alessio Stefani**, **Anna Chiara Brunetti**, **Christophe Peucheret**, **Francesco Da Ros**, **Karsten Rottwitt**, **Kristian Nielsen**, **Xiaomin Liu** and **Zohreh Lali-Dastjerdi**, who took the time to proofread parts of this Thesis, point out its weaknesses, and suggest improvements.

I also would like to thank my (past and present) colleagues at DTU Fotonik, especially **Kristian R. Hansen**, for translating the abstract of this Thesis. It has been a pleasure to work with you all.

My deepest thanks go to my family, for always giving without ever asking for anything in return and for giving me strength and support; without them I would feel lost.

Another special thanks goes to **Alessio Stefani**, **Anna Chiara Brunetti** and **Carolina Souza da Conceição**, for your support and your love in

these years, no matter where in the world we are. I will always have to thank Denmark for having you in my life and for the great time spent together.

A special thanks goes to **Silvia** who found a way to be always close, despite the distance.

Finally, I would like to thank all my friends for sharing with me all the good and bad moments and for always bringing me a smile.

Abstract

Fiber optical parametric amplifiers (FOPAs) are attractive because they can provide large gain over a broad range of central wavelengths, depending only on the availability of a suitable pump laser. In addition, FOPAs are suitable for the realization of all-optical signal processing functionalities and can operate with a potentially low noise figure with respect to erbium-doped fiber amplifiers and Raman amplifiers, when working in phase-sensitive configurations. A characterization of the signal distortion mechanisms introduced by FOPAs is relevant for investigating the applicability of FOPAs for the amplification of high speed signals with bit rates in excess of 1 Tbit/s per wavelength channel.

The work presented in this thesis focuses on the distortion mechanisms affecting signals amplified by single-pump phase-insensitive FOPAs. The noise due to the cross coupling between the signal and the pump is also investigated. The pump-to-signal noise transfer has been recognized as one of the major noise source in FOPAs. This is due to the fast response of FOPAs (few fs), because of which intensity fluctuations of the pump cause an instantaneous gain modulation. The intensity modulation transfer from the pump to the signal is experimentally investigated for pump modulation frequencies up to 27 GHz and also in the saturation regime. A good agreement is found both with the theoretical model in the case of an undepleted pump and with the numerical results in the saturation regime, showing that the intensity modulation transfer can be reduced in saturated FOPAs.

In order to characterize propagation impairments such as dispersion and Kerr effect, affecting signals reaching multi-terabit per second per channel, short pulses on the order of 500 fs need to be considered. Therefore, a short pulses fiber laser source is implemented to obtain an all-fiber system. The advantages of all fiber-systems are related to their reliability, long-term stability and compactness. Fiber optical parametric chirped pulse amplifica-

tion is promising for the amplification of such signals thanks to the inherent compatibility of FOPAs with fiber optical systems and high gain over broad bandwidths. In particular, the amplification of 400 fs pulses is investigated in a single-pump fiber optical chirped pulse amplification scheme. First, a dynamic characterization is carried out both in unsaturated and saturated regimes and, then, amplification of short pulses compatible with Tbaud systems is experimentally demonstrated for the first time. This opens the way to the demonstration of a first broadband amplification scheme for high-speed signals reaching multi-terabit per second per channel.

Resumé (Danish abstract)

Fiberoptiske parametriske forstærkere (FPF) er attraktive fordi de kan levere stor forstærkning over et bredt spektrum, afhængigt kun af tilstedeværelsen af en passende pumpelaser. Derudover er FPF velegnede til fuld-optisk signal processering, og kan operere med en potentielt lav støjgrænse, sammenlignet med erbium-doterede og Raman fiberforstærkere, når de arbejder i en fase-følsom konfiguration. En karakterisering af signalforvrængningsmekanismer i FPF er relevant for at undersøge anvendeligheden af FPF til forstærkning af højhastighedssignaler med bitrater over 1 Tbit/s per bølgelængdekanal. Arbejdet præsenteret i denne afhandling fokuserer på forvrængningsmekanismer, der påvirker et signal som forstærkes af enkelt-pumpe fase-ufølsomme FPF. Støj, der skyldes krydskobling mellem signalet og pumpen, undersøges også. Pumpe-til-signal støjoverførsel har vist sig at være en væsentlig støjkilde i FPF. Dette skyldes disse forstærkeres hurtige respons (nogle få fs), som resulterer i at pumpens intensitetsfluktuationer forårsager en øjeblikkelig modulation af forstærkningen. Overførslen af intensitetsmodulation fra pumpe til signalet undersøges eksperimentelt for pumpemodulationsfrekvenser op til 27 GHz, og også i det mættede regime. Der findes god overensstemmelse med den teoretiske model, både i tilfældet med uændret pumpeeffekt, samt med numeriske beregninger i det mættede regime, hvilket viser at intensitetsmodulationsoverførsel kan reduceres i mættede FPF. For at karakterisere forvrængningsfænomener som dispersion og Kerr-effekt, som påvirker signaler med multi-terabit per sekund per kanal, må korte pulser med en størrelsesorden på 500 fs betragtes. En kort-puls fiberlaserkilde er derfor implementeret for at opnå et fuld-fiber-system. Fordelen ved alle fuld-fiber-systemer er relateret til deres pålidelighed, lang-sigts stabilitet og kompakthed, og fiberoptisk parametrisk forstærkning af “chirped” pulser er lovende for forstærkning af sådanne signaler, takket være deres indbyggede

kompatibilitet med fiberoptiske systemer og høje forstærkning over stor båndbredde. I særdeleshed undersøges forstærkning af korte subpicosekund pulser på 400 fs i en enkelt-pumpe fiberoptisk chirped-puls forstærker. Først udføres en dynamisk karakterisering i både umættet og mættet regime, og derefter demonstreres forstærkning af korte pulser, kompatible med Tbaud-systemer, eksperimentelt for første gang.

PhD publication list

Articles in peer-reviewed journals:

1. **V. Cristofori**, Z. Lali-Dastjerdi, L. S. Rishøj, M. Galili, C. Peucheret and K. Rottwitt, "Dynamic characterization and amplification of sub-picosecond pulses in fiber optical parametric chirped pulse amplifiers," submitted to *Optics Express* (2013).

2. **V. Cristofori**, Z. Lali-Dastjerdi,T. Lund-Hansen, C. Peucheret and K. Rottwitt, "Experimental investigation of saturation effect on pump-to-signal intensity modulation transfer in single-pump phase-insensitive fiber optic parametric amplifier," *Journal of the Optical Society of America B*, vol. 30, no. 4, 884–888, 2013.

3. Z. Lali-Dastjerdi, **V. Cristofori**, T. Lund-Hansen, K. Rottwitt, M. Galili and C. Peucheret, "Pump-to-signal intensity modulation transfer characteristics in FOPAs: Modulation frequency and saturation effect," *Journal of Lightwave Technology*, vol. 30, no. 18, 3061-3067, 2012.

Articles in conferences:

4. **V. Cristofori**, Z. Lali-Dastjerdi, L. S. Rishøj, M. Galili, C. Peucheret and K. Rottwitt, "Dynamic characterization of fiber optical chirped pulse amplification for sub-ps pulses,". In *Nonlinear Optics Topical Meeting (NLO) 2013*, Hawaii, USA, paper NW4A.07, 2013.

5. **V. Cristofori**, Z. Lali-Dastjerdi, F. Da Ros, L. S. Rishøj, M. Galili, C. Peucheret and K. Rottwitt, "Fiber optical parametric chirped pulse amplification of sub-picosecond pulses". In *OptoElectronics*

and Communications Conference (OECC) 2013, Kyoto, Japan, paper TuS2-3, 2013.

6. Z. Lali-Dastjerdi, O. Ozolins, Y. An, **V. Cristofori**, F. Da Ros, N. Kan, H. Hu, H. C. H. Mulvad, K. Rottwitt, M. Galili and C. Peucheret, "Demonstration of cascaded in-line single-pump fiber optical parametric amplifiers in recirculating loop transmission". In *European Conference on Optical Communication (ECOC) 2012*, Amsterdam, The Netherlands, paper Mo.2.C.5, 2012.

7. **V. Cristofori**, Z. Lali-Dastjerdi, T. Lund-Hansen, M. Galili, C. Peucheret and K. Rottwitt, "Saturation effect on pump-to-signal intensity modulation transfer in single-pump phase-insensitive fiber optic parametric amplifiers". In *IEEE Photonics Conference (IPC) 2011*, Arlington, Virginia, USA, paper TuO2, 2011.

8. **V. Cristofori**, T. Lund-Hansen, C. Peucheret and K. Rottwitt, "Experimental investigation of pump-to-signal noise transfer in one pump phase insensitive fibre optic parametric amplifiers". In *International Conference on Transparent Optical Networks (ICTON) 2011*, Stockholm, Sweden, paper Tu.C1.4, 2011.

9. T. Lund-Hansen, K. Rottwitt, C. Peucheret, Z. Lali-Dastjerdi, L. S. Rishøj, A. S. Svane, L. M. Andersen and **V. Cristofori**, "Saturation effect on pump-to-signal intensity modulation transfer in single-pump phase-insensitive fiber optic parametric amplifiers," (invited). In *Photonics 2010*, Guwahati, India, 2010.

Chapter 1

Introduction

Optical communications in fibers have undergone rapid progress since the development of the first commercial erbium-doped fiber amplifiers (EDFAs) in the mid-nineties. The development of optical amplification opened the way for the transport of massive amounts of information over long distances. This triggered an increasing demand for broader bandwidth, facilitated by the use of wavelength division multiplexing (WDM), utilizing dozens of transmission channels covering a wide span of optical frequencies. However, in an EDFA the gain bandwidth is limited by the discrete nature of the energy transitions of the dopant material, binding the operational frequencies to two distinct communication bands (C or L-band) [1]. Fiber optical parametric amplifiers (FOPAs) can be valid candidates for high amplification over a broad bandwidth and at any wavelength. The first demonstration of parametric amplification in fibers through phase-matched four-wave mixing was performed by Stolen in 1975 [2], while a first demonstration of a net black-box gain in FOPAs was reported by J. Hansryd and P. A. Andrekson in 2001 [3].

FOPAs rely on the third-order susceptibility of silica fiber, inducing the four-wave mixing (FWM) nonlinear process. Under the fulfillment of a phase matching condition, an intense pump exchanges energy with a co-propagating weak signal, amplifying it. A phase conjugated replica of the signal, called idler, originates from the process at a frequency symmetric to the signal with respect to the pump. Since the parametric amplification in FOPAs relies on energy exchange and not on energy transitions, high gain can be obtained at any wavelength [4–7]. The only constrain, apart from the fulfillment of the phase matching condition, is that the pump should

be placed in the anomalous dispersion region [8]. This allows to obtain amplification also outside the conventional communication bands.
An amplification record of 70 dB has been reported in 2006 by T. Torounidis *et al.* [9] in a continuous wave (CW) pumped FOPA using a single pump. A higher gain can be obtained by means of pulsed pumps [10], since the instantaneous gain depends on the peak power and stimulated Brillouin scattering is no longer limiting the pump power.
Even if Raman amplifiers, similarly to FOPA, can provide gain centered at any arbitrary wavelength, broader bandwidths can be obtained in parametric amplifiers, since the parametric process relies on energy exchange. In particular, the gain bandwidth depends on the dispersion profile of the fiber and on the pump power. An increase of the gain bandwidth with the pump power provides a way to obtain a bandwidths over hundreds nanometers using one or two pumps. In [11], a gain bandwidth of 100 nm with a gain of 11.5 dB and a ± 2 dB gain variation has been demonstrated in a single-pump FOPA. With respect to single-pump FOPAs, double-pump FOPAs allow for a higher gain flatness over broader bandwidths. In [12], a 20 dB gain with a 4.7 dB gain ripple over a bandwidth of 155 nm was reported, while in [13] a gain up to 40 dB over a full-width at half maximum (FWHM) bandwidth of 81 nm was achieved. However over such broadband gains, stimulated Raman scattering (SRS) and the zero-dispersion wavelength (ZDW) variations along the fiber affect the parametric gain and need to be controlled.
Another interesting property of FOPAs is that they can operate with a potentially low noise figure (NF) above the quantum-limited value of 3 dB for high gain amplifiers when operating as phase-insensitive amplifiers. In particular, a NF below 4 dB has been experimentally demonstrated [14] for a phase-insensitive configuration. However, better noise performances can be obtained when operating in a phase-sensitive configuration. In particular, when all the three waves, that is pump, signal and idler, are present at the input of the fiber and their phases are controlled, a phase sensitive amplification can be performed. Depending on the relative phases, amplification or attenuation is achieved [15, 16] and an ideal NF of 0 dB can be obtained. For phase-sensitive configurations the NF can be lower than 3 dB and a record value of 1 dB has been demonstrated experimentally [17]. FOPAs are, thus, good candidates for amplification of signals reaching multi-terabit per second per channel. In order to obtain that, a chirped pulse amplification scheme has been investigated. Fiber optical parametric chirped pulse amplification has recently been the focus of studies as

a promising amplification scheme for picosecond [18, 19] and femtosecond pulses [20, 21]. Fiber optical parametric chirped pulse amplification using 200 fs pulses has been investigated in the 1 μm wavelengths region [22], where high power and broad bandwidth ytterbium lasers are available. The amplified compressed pulses were broader (660 fs) with respect to the input pulses due to uncompensated higher order dispersion terms. In the 1.5 μm wavelengths region, amplification of pulses as short as 750 fs by means of fiber optical parametric chirped pulse amplifier in an all-fiber system has been reported in [23].
The amplification of Tbaud-class pulses (on the order of 500 fs) is becoming increasingly relevant due to recent demonstrations of single wavelength channel systems at bit rates of 1.28 Tbit/s, 5.1 Tbit/s or even 10.2 Tbit/s [24–26]. The implementation of all-fiber amplification systems at 1.5 μm is, thus, of high interest for the realization of stable and compact optical systems. Efficient fiber laser sources emitting short pulses on the order of few tens of femtoseconds at 1.5 μm are available. A common configuration for the emission of soliton pulses is the so-called figure-of-eight laser (F8L), introduced by I. N. Duling III in 1991 [27]. The advantage of employing soliton pulses is their stability against dispersion and nonlinearities during propagation over long distances [8]. Fiber optical parametric oscillators have also been demonstrated to be stable and compact tunable laser sources, mainly for non conventional bands [28, 29].
Besides amplification, FOPAs are suitable for the realization of all-optical signal processing [28, 30]. High-speed signal processing can be realized thanks to the fast response of fiber nonlinearities. If the pump is modulated the modulation is transferred to the signal and the idler. This can be used to implement signal regeneration, demultiplexing of optical time division multiplexed (OTDM) signals and optical sampling. In particular, phase-insensitive FOPAs are able to regenerate the amplitude of intensity- and phase-encoded signals, while phase-sensitive FOPAs are able to regenerate the phase of phase-encoded signals [31]. Phase and amplitude regeneration has been demonstrated for different modulation formats and bit rates [32–36]. Demultiplexing of OTDM signals has also been demonstrated, using pulsed-pump FOPAs with repetition rates synchronized with the OTDM signal repetition rate [37, 38]. Wavelength conversion can also be realized, due to the creation of an idler when the pump and the signal are launched in a FOPA. Signals at not conventional wavelengths can, thus, be generated [7]. Furthermore, considering that if the signal is modulated its modulation is transferred to the idler, this can be used for shifting the

optical frequency of a communication signal. Moreover, another property related to the idler is that its phase is opposite to that of the original signal. The phase conjugation can be used to counteract effects such as dispersion and nonlinear phenomena affecting the phase of the waves [39, 40].

1.1 Thesis contributions and structure

The work behind this thesis focuses on the characterization of distortion mechanisms on a signal amplified by single-pump phase-insensitive fiber optical parametric amplifiers (PI-FOPAs), both in saturated and unsaturated regimes. Among the mechanisms resulting in signal distortion, particularly relevant are the cross coupling between the pump and signal, responsible for the instantaneous transfer of the noise of the pump to the signal, and for the transfer of phase modulation used on the pump to avoid stimulated Brillouin scattering. Also phenomena such as stimulated Raman scattering, self-phase modulation and group-velocity dispersion need to be considered and investigated.

Chapter 2 presents an overview of the theory of parametric amplification in optical fibers in the case of small-signal gain, starting from the process of four-wave mixing and the phase matching condition to be fulfilled in order to obtain parametric gain. The theoretical model for unsaturated FOPAs is then compared with the results obtained both by numerical and experimental investigations. A brief overview on stimulated Brillouin scattering and stimulated Raman scattering is also provided, showing the basic distortion effects due to these inelastic phenomena.

In Chapter 3, the noise affecting the signal due to the cross coupling between the pump and the signal is investigated. The pump-to-signal noise transfer has been recognized as one of the major noise sources in FOPAs, since the gain is modulated instantaneously by the intensity fluctuations of the pump. The intensity modulation transfer from the pump to the signal is experimentally investigated considering a continuous wave signal. In particular, the experimental investigation of the pump-to-signal intensity modulation transfer in single-pump PI-FOPAs is extended, for the first time, to pump modulation frequencies up to 27 GHz and to the gain saturation regime. A good agreement is found with the analytical

model in the small-signal gain case and with the numerical model in case of saturated FOPAs, showing that the intensity modulation transfer can be reduced by operating in the saturation regime.

In order to characterize distortion phenomena such as dispersion and the Kerr effect, short pulses propagating into the FOPA are need to be considered. Therefore, the realization of a short pulses fiber laser source is described in Chapter 4. This source can be conveniently integrated into an all-fiber system. The laser configuration presented is the so-called figure-of-eight laser (F8L). Mode-locked pulses are estimeted to be on the order of 250 fs with a repetition rate of 14 MHz and an estimated peak power of 6.8 W. However, it was not possible to measure an autocorrelation trace because of the low efficiency of the laser due to the use of a low-doped erbium-doped fiber (EDF).

Chapter 5 covers the investigation of the amplification of short subpicosecond pulses with a full-width at half maximum (FWHM) of 400 fs in a single-pump fiber optical chirped pulse amplification scheme. First, a dynamic characterization is carried out both in unsaturated and saturated regimes. A significant broadening of the pulses is experimentally shown due to a combined effect of dispersion, self-phase modulation and limited FOPA gain bandwidth. Finally, amplification of short pulses compatible with Tbaud systems is experimentally demonstrated for the first time. The 400 fs pulses are stretched, amplified by 26 dB and compressed back to 500 fs.

Chapter 6 concludes this Thesis, summing up the contribution of this project to the investigation of the applicability of FOPAs for amplification of high speed signals. Some possible future developments are also presented.

Chapter 2

Fiber Optical Parametric Amplification

2.1 Introduction

In a fiber optical parametric amplifier (FOPA) the amplification is provided by the nonlinear process of four-wave mixing (FWM), which relies on the third-order nonlinearity of the material [8, 28]. FWM is one of those nonlinear processes in fiber that are referred to as parametric processes, because they involve the modulation of one of the material parameters, such as the nonlinear refractive index, and require the fulfillment of a phase-matching condition in order to build up along the fiber. Under the fulfillment of the phase-matching condition, the FOPA can provide large gain and low noise at an arbitrary wavelength, over relatively short fibers in the range of hundreds meters. The operation of the FOPA relies upon specific fiber parameters, which determine the operational spectral area, bandwidth and performance of the amplifier. In fact, in the FWM process the bandwidth can be tuned according to the particular application and amplification at different wavelengths has been demonstrated [4–7]. Furthermore, the parametric gain requires the employment of high pump powers, which became available thanks to the development of high power continuous wave (CW) amplifiers. However, the use of high pump powers gives rise to other nonlinear effects, such as stimulated Brillouin scattering (SBS) and stimulated Raman scattering (SRS), which need to be taken into consideration and characterized in experimental designs, since they

affect the FOPA gain spectrum. An overview of the nonlinear properties of single-mode fibers and of the FWM process is introduced in Sections 2.2 and 2.3, respectively. The focus in Subsection 2.4.4 is on parametric amplification in optical fibers, showing the basics of the gain spectrum theoretically, numerically and also experimentally. SBS is covered in Section 2.5 along with the techniques used for its suppression, which is necessary for the FOPA to operate properly. In Section 2.6 a brief description about SRS and Raman gain is provided.

2.2 Nonlinearities in Optical Fibers

Glass optical fibers are nonlinear media, i.e. the material has a nonlinear response upon the application of a sufficiently intense electric field is applied. The nonlinearity in optical fibers gives rise to the FWM process and, in particular, to parametric amplification. When a sufficiently intense electric field $\mathbf{E}$ is applied, the total induced polarization $\mathbf{E}$ is not linear and can be expressed as

$$P = \varepsilon_0(\chi^{(1)} \cdot \mathbf{E} + \chi^{(2)} : \mathbf{E} + \chi^{(3)} \vdots \mathbf{E} + \ldots), \tag{2.1}$$

where ε_0 is the vacuum permittivity and $\chi^{(j)}$ $(j = 1, 2, \ldots)$ is the j^{th} order susceptibility of the material. $\chi^{(j)}$ is a tensor of rank $j+1$. Due to the symmetric structure of the fiber material, i.e. (SiO_2), the $\chi^{(2)}$ term in Eq. (2.1) vanishes [41], while the $\chi^{(1)}$ term is the linear susceptibility and it is the dominant contribution to the induced polarization. The linear susceptibility is responsible for the propagation losses α and the linear refractive index n_0 [8]. The lowest order nonlinear effect in fiber is associated to the third-order susceptibility $\chi^{(3)}$, also known as Kerr nonlinearity, which gives rise to the FWM process and nonlinear refraction. Since most of the nonlinear effects in optical fibers arise from nonlinear refraction, the Kerr nonlinearity can be introduced by the nonlinear refractive index coefficient n_2. It can be shown that, in fibers, the presence of strong light waves with intensity $\mathbf{I}$ modifies the refractive index according to the relation

$$n = n_0 + n_2\mathbf{I}, \tag{2.2}$$

where n_0 is the linear refractive index. The nonlinear refractive index coefficient n_2 is related to the third-order susceptibility by the following

expression

$$n_2 = \frac{3}{8n} Re(\chi^{(3)}_{xxxx}), \tag{2.3}$$

where the incident electric field is assumed to be linearly polarized so that only one component $\chi^{(3)}_{xxxx}$ of the tensor $\chi^{(3)}$ contributes to the refractive index.

Since a change in the refractive index implies a change in the propagation constant of the wave and therefore a change in phase due to propagation, an intense wave propagating along the fiber induces a change in its own phase, giving rise to the so-called self-phase modulation (SPM), and in the phase of other waves passing through the same region, giving rise to the so-called cross-phase modulation (XPM). SPM refers to the self-induced phase shift experienced by an electric field during its propagation in an optical fiber and it is responsible also for the spectral broadening of ultrashort pulses [42] and formation of solitons [43], that will be discussed in Chapter 4. XPM, instead, refers to the nonlinear phase-shift induced to an electric field by another field having a different wavelength, direction or state of polarization [8]. Both SPM and XPM are elastic processes, i.e. there is no energy exchange between the wave and the medium. However, the nonlinearities in fibers give also birth to nonlinear effects from stimulated inelastic scattering. There are two main inelastic scattering processes: SBS and SRS. Both of them rely on a non-instantaneous material response and are related to the vibrational excitation modes of silica. They will be discussed in Sections 2.5 and 2.6, respectively. However, since silica is a material with a really low n_2 (between 2.2 and 3.4 10^{-20} m^2/W), all nonlinear effects require the application of an intense electric field. This can be achieved by confining a high optical power in a very small cross-section and in order to calculate the effect of n_2, one must know besides the cross-section the beam profile and the total power. Therefore, it is convenient when dealing with optical fibers and also when comparing them, to introduce a parameter that can describe the nonlinear properties of the fiber depending on its geometry and constitutive material. This parameter is introduced in the following section.

2.2.1 Fiber Nonlinear Coefficient

The fiber nonlinear coefficient γ is defined as

$$\gamma = \frac{2\pi}{\lambda} \frac{n_2}{A_{eff}}. \tag{2.4}$$

λ is the wavelength and the mode effective area A_{eff} is defined as

$$A_{eff} = \frac{(\int\int_{-\infty}^{\infty} |F(x,y)|^2 dxdy)^2}{\int\int_{-\infty}^{\infty} |F(x,y)|^4 dxdy}, \tag{2.5}$$

where $F(x,y)$ is the modal distribution of the fundamental fiber mode. The mode effective area depends on fiber parameters, such as the core radius and the core-cladding index difference, and it typically varies between 1 to 100 μm^2 in the 1.5 μm wavelength region. From Eq. (2.4), it is clear that the fiber nonlinear coefficient contains information about the material, through n_2, and about the fiber mode through its effective area A_{eff}. Furthermore, it can be seen that in order to obtain a large nonlinear coefficient and, thus, a large phase-shift, a fiber should be designed to have a large n_2 and a small A_{eff}. In order to increase the nonlinear refractive index coefficient, the fiber core is usually doped with chemical components with higher nonlinear refractive indices than silica such as germania (GeO_2), phosphorus pentoxide (P_2O_5) and alumina (Al_2O_3). The refractive index increases according to the doping concentration [44, 45], but in order to guarantee single mode operation the core-cladding refractive index difference should not exceed a value for which the normalized frequency V is lower than 2.405. The normalized frequency is defined as $V = \frac{2\pi r}{\lambda}(\sqrt{(n_{core}^2 - n_{cladding}^2)}$, where r is the radius of the fiber core and n_{core} and $n_{cladding}$ are the refractive indices of the core and the cladding layer, respectively. However, an increase in fiber doping concentration also results in higher losses, due to an increased Rayleigh scattering [46]. Anyway, the higher core index also increases the mode confinement, reducing the effective mode area and enhancing the nonlinear effects. The so-called highly nonlinear fibers (HNLFs) that are GeO_2 doped [47] represents an example of fibers where the effective mode area is reduced intentionally to enhance the nonlinear effects.

For standard single mode fiber with a core diameter of 10 μm, the core to cladding index difference Δn^+ is typically around 0.4% as shown in Fig. 2.1(b), where a standard single mode fiber (SSMF) with standard step-index profile is considered. The refractive index profile of the SSMF is compared with the profile of an HNLF, shown in Fig. 2.1(a), for which the core is smaller (4 μm) and the Δn^+ is approximately 3%. The W shaped cladding profile with a fluorine-doped depressed cladding has been employed to realize single mode operation and flexibilities in the design of chromatic dispersion. Therefore, a typical HNLF has a nonlinear coefficient γ between 10 to 20 $(W \cdot km)^{-1}$, which is approximately ten times higher

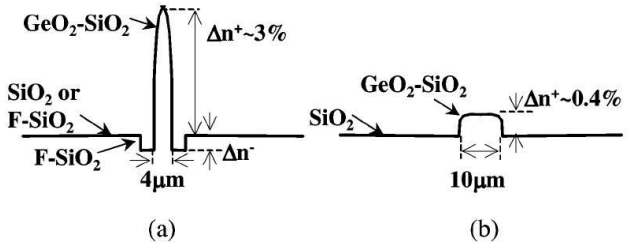

Figure 2.1: Schematic refractive index profile of a typical (a) HNLF and (b) SSMF. From [47].

than that of a SSMF, which is approximately 1.3 $(\mathrm{W} \cdot \mathrm{km})^{-1}$.
GeO_2-doped HNLFs are the most employed fibers in fiber optical parametric amplification due to their high nonlinearities and low losses. However, among novel fibers, it is also worth mentioning the Al_2O_3 doped HNLFs, since they can be used to reduce the SBS threshold by lowering the acoustic index of the core while increasing its optical index [48]. As previously mentioned, SBS is discussed later on in this chapter.

2.3 Four-Wave Mixing

The FWM process relies on the nonlinear response of a material upon the application of an electric field [2]. As mentioned, the induced polarization in the medium can be expressed as in Eq. (2.1), where the terms depend on the magnitude of the electric field and the nonlinear susceptibilities. Since in silica the $\chi^{(2)}$ term vanishes, nonlinear effects in fibers are third-order parametric processes and nonlinear part of the induced polarization becomes

$$P_{NL} = \varepsilon_0 \chi^{(3)} \mathbf{E}. \tag{2.6}$$

Third-order parametric processes involve interactions among four optical waves. In fact, considering four CW waves at frequencies ω_1, ω_2, ω_3 and ω_4, and assuming all wave to be linearly polarized along the same axis, the total electric field can be expressed as

$$\mathbf{E} = \frac{1}{2} \left\{ \sum_{j=1}^{4} E_j exp[i(\beta_j z - \omega_j t)] + c.c. \right\}, \tag{2.7}$$

where β_j is the propagation constant for ω_j ($j = 1, \ldots 4$) and $E_j = F_j(x,y)A_j(z)$ is the slowly varying electric field. $A_j(z)$ is the complex amplitude of the electric field, while $F_j(x,y)$ is the spatial distribution of the fiber mode that takes into account the spatial dependence of the field components E_j. The propagation constant and the evolution of the complex amplitude during the propagation along the fiber is discussed separately later on in this section. By substituting Eq. (2.7) in Eq. (2.6), it is possible to express the induced nonlinear polarization of one of the waves, for example P_4, as follows

$$\begin{aligned} P_4 &= \frac{3\varepsilon_0}{4}\chi^{(3)}_{xxxx}[|E_4|^2E_4 + 2(|E_1|^2 + |E_2|^2 + |E_3|)E_4 + 2E_1E_2E_3\exp(i\theta_+) + \\ &\quad 2E_1E_2E_3^*\exp(i\theta_-) + \ldots]. \end{aligned} \tag{2.8}$$

θ_+ and θ_- account for the phase mismatch between the four waves. The first term in bracket is responsible for SPM, the following three terms are responsible for XPM and the last two terms account for two types of third-order parametric processes. The term depending on θ_+ accounts for third harmonic generation (THG) and it is not considered in this work. The term depending on θ_- represents the FWM process, on which the parametric amplification relies. θ_- is expressed as

$$\theta_- = (\beta_1 + \beta_2 - \beta_3 - \beta_4)z - (\omega_1 + \omega_2 - \omega_3 - \omega_4)t \tag{2.9}$$

and the only significant case for FWMis when the phase mismatch vanishes, that is in case of perfect frequencies and wave vectors matching. Therefore the two conditions that need to be satisfied are energy conservation

$$\omega_1 + \omega_2 = \omega_3 + \omega_4 \tag{2.10}$$

and phase matching

$$\Delta\beta = \beta_3 + \beta_4 - \beta_1 - \beta_2 = 0 \tag{2.11}$$

Based on the number of pump waves employed, there are two main cases of FWM as schematically represented in Fig. 2.2. One is the *non-degenerate* case in which $\omega_1 \neq \omega_2$ and two pumps at two different frequencies must be launched into the fiber. In this case, two photons at frequencies ω_1 and ω_2 are annihilated, while two photons at frequencies ω_3 and ω_4 are created. The second is the *degenerate* case in which $\omega_1 = \omega_2 = \omega_p$ and only one pump is necessary to amplify the small signal. In this case the pump loses two photons to generate a signal and an idler photon at frequencies ω_s

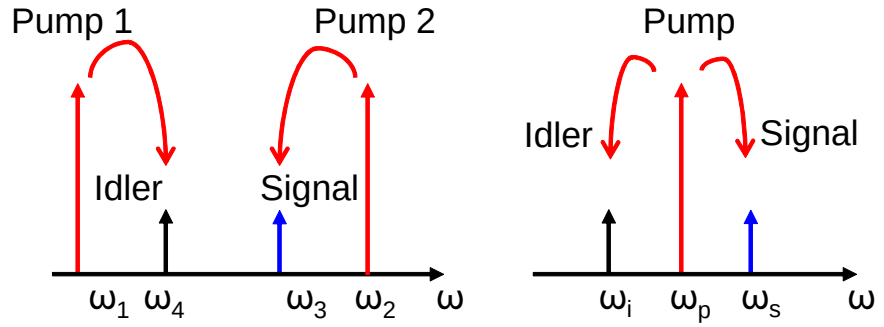

Figure 2.2: Schematic of (a) non-degenerate and (b) degenerate FWM

and ω_i, respectively, placed symmetrically with respect to the pump. In the degenerate case the energy conservation and the phase matching conditions become

$$2\omega_p = \omega_s + \omega_i \tag{2.12}$$

$$\Delta\beta = \beta_s + \beta_i - 2\beta_p = 0 \tag{2.13}$$

where the standard notation for the pump, signal and idler has been adopted. In this work, the *degenerate* case is the only one considered and all the results here presented were obtained considering a single pump configuration for the FOPA.

2.3.1 Propagation Constant

The propagation constant of a mode describes how the phase of the mode varies along the propagation direction and it is expressed as

$$\beta(\omega) = n_{eff}(\omega)\frac{\omega}{c}, \tag{2.14}$$

where n_{eff} is the effective refractive index of the mode, ω is its angular frequency and c is the speed of the light in vacuum. Being a function of frequency, the propagation constant accounts for chromatic dispersion in fibers. In particular, the dispersion is described mathematically by expanding the propagation constant in Taylor series about a reference angular frequency ω_r

$$\beta(\omega) = \beta_0 + \beta_1(\omega - \omega_r) + \frac{1}{2!}\beta_2(\omega - \omega_r)^2 + \frac{1}{3!}\beta_3(\omega - \omega_r)^3 + \ldots, \tag{2.15}$$

where

$$\beta_m = \left(\frac{d^m\beta}{d\omega^m}\right)_{\omega=\omega_0} \qquad (m = 0, 1, 2, \ldots). \tag{2.16}$$

The first order dispersion β_1 is related to the *group-velocity* of the optical wave (i.e. the velocity at which the envelope of the wave propagates) through the relation

$$v_g = \frac{d\omega}{d\beta} = \frac{1}{\beta_1}, \tag{2.17}$$

while the second-order dispersion represents the *group-velocity dispersion (GVD)* and β_2 is known as the GVD parameter. However, in practice the so-called *dispersion parameter* D is often used, for instance in fiber specifications, and is defined as

$$D = \frac{d\beta_1}{d\lambda} = -\frac{2\pi c}{\lambda^2}\beta_2. \tag{2.18}$$

The dispersion parameter is expressed in units of $\mathrm{ps}\cdot\mathrm{nm}^{-1}\cdot\mathrm{km}^{-1}$ and the wavelength at which D (or β_2) is equal to zero is called *zero-dispersion wavelength (ZDW)* and it is indicated with λ_0. In standard fibers, this wavelength is approximately 1.27 μm, while in dispersion shifted fibers (DSFs) it is moved to the 1.55 μm region. Furthermore, the wavelength region where $D > 0$ (i.e. $\beta_2 < 0$) is called *anomalous dispersion* region, while the region for which $D < 0$ (i.e. $\beta_2 > 0$) is named *normal dispersion* region.

Another important parameter practically used is the *dispersion slope* S, defined as $dD/d\lambda$, and depending on the third-order dispersion (TOD) β_3. The dispersion slope is given at the ZDW in the fiber specifications and is expressed in units of $\mathrm{ps}\cdot\mathrm{nm}^{-2}\cdot\mathrm{km}^{-1}$. Similarly to the dispersion slope, the fourth-order dispersion (FOD) term can be extracted from $dS/d\lambda$ and so on for higher order dispersion terms. Usually only the first three terms of Eq. (2.15) are significant. However, higher order terms should only be considered for ultrashort pulses having a really broad spectral bandwidth or for FOPA amplification bandwidth over 100 nm. Fig. 2.3 shows the influence of different dispersion terms up to the fourth-order in a standard HNLF with ZDW at 1550 nm, $S = 0.0185\ \mathrm{ps}\cdot\mathrm{nm}^{-2}\cdot\mathrm{km}^{-1}$ and $dS/d\lambda = -1\cdot10^{-4}\ \mathrm{ps}\cdot\mathrm{nm}^{-3}\cdot\mathrm{km}^{-1}$. $\beta(\omega)$ is expanded about a reference wavelength of 1555 nm. It can be seen that β_4 does not have a significant effect over a bandwidth of 100 nm, though its effect becomes more and more relevant as the broader the frequency range is. The dispersion terms have a strong impact on the parametric gain and the amplification bandwidth of FOPAs [49, 50] as discussed in Sec. 2.4.4.

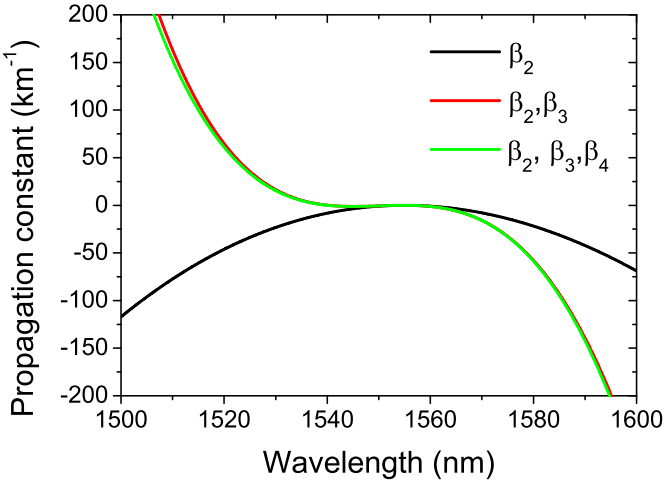

Figure 2.3: Propagation constant $\beta(\omega)$ of a standard DSF-HNLF considering different dispersion terms. *Courtesy of Zohreh Lali-Dastjerdi.*

2.4 Single-Pump FOPAs

The parametric amplification in single-pump FOPAs is described in this section, starting from the coupled amplitude equations and the phase-matching condition. Afterwards, the parametric gain and the amplification bandwidth are first introduced and then characterized by numerical simulations and experimental measurements.

2.4.1 Coupled Amplitude Equations

The evolution of the complex amplitudes $A_j(z)$ $(j = 1, \ldots 4)$ of the four waves involved in the degenerate FWM process ($\omega_1 = \omega_2 = \omega_p$) can be expressed by a set of three coupled equations, obtained by substituting the polarization expressed as in Eq. (2.8) and the total electric field in the the

wave equation [8]

$$\frac{dA_p}{dz} = i\gamma \left\{ \left[|A_p|^2 + 2\left(|A_s|^2 + |A_i|^2 \right) \right] A_p + 2A_s A_i A_p^* \exp(i\Delta\beta z) \right\}, , \quad (2.19)$$

$$\frac{dA_s}{dz} = i\gamma \left\{ \left[|A_s|^2 + 2\left(|A_i|^2 + |A_p|^2 \right) \right] A_s + A_p^2 A_i^* \exp(-i\Delta\beta z) \right\}, , \quad (2.20)$$

$$\frac{dA_i}{dz} = i\gamma \left\{ \left[|A_i|^2 + 2\left(|A_s|^2 + |A_p|^2 \right) \right] A_i + A_p^2 A_s^* \exp(-i\Delta\beta z) \right\}, . \quad (2.21)$$

The first term on the right hand side of each equation is responsible for both SPM and XPM, while the second term is responsible for the power transfer due to FWM. The fiber loss is neglected and can be taken into account by adding a loss term $((\alpha/2)A_j)$ to the right hand side of each equation.

The three coupled equations can be rewritten in terms of power P and phase ϕ of the three waves (pump, signal and idler) assuming that $A_j(z) = \sqrt{P_j}\exp(i\phi_j)$ for $j\epsilon\{p, s, i\}$ [30, 51]. The coupled equations (2.19)-(2.21) become

$$\frac{dP_p}{dz} = -4\gamma \left(P_p^2 P_s P_i \right)^{\frac{1}{2}} \sin\theta, \quad (2.22)$$

$$\frac{dP_s}{dz} = 2\gamma \left(P_p^2 P_s P_i \right)^{\frac{1}{2}} \sin\theta, \quad (2.23)$$

$$\frac{dP_i}{dz} = 2\gamma \left(P_p^2 P_s P_i \right)^{\frac{1}{2}} \sin\theta, \quad (2.24)$$

$$\frac{d\theta}{dz} = \Delta\beta + \gamma \left\{ 2P_p - P_s - P_i + \left[\left(P_p^2 P_i / P_s \right)^{\frac{1}{2}} + \left(P_p^2 P_s / P_i \right)^{\frac{1}{2}} - 4\left(P_i P_s \right)^{\frac{1}{2}} \right] \cos\theta \right\}, \quad (2.25)$$

where P_p, P_s and P_i are the pump, the signal, and the idler powers, respectively, while $\theta(z) = \Delta\beta z + \phi_s(z) + \phi_i(z) - 2\phi_p(z)$, is the relative phase difference between the three waves. $\Delta\beta$ is the linear phase mismatch and ϕ_p, ϕ_s, and ϕ_i are the phases of the pump, the signal, and the idler, respectively, accounting for the nonlinear phase shift. It is worth to notice that by controlling the phase relation θ, it is possible to control the direction of the power flow from the pump to the signal and idler or viceversa, obtaining parametric amplification ($\theta = \pi/2$) or attenuation ($\theta = -\pi/2$), respectively. Therefore, if all the three waves are present at the input of the fiber and the relative phase is adjusted, it is possible to decide if the signal is amplified or attenuated. This allows the realization of phase-sensitive parametric amplification [15, 16]. The phase-matching condition is discussed in the next section.

2.4.2 Phase Matching

The relative phase difference θ between the three involved waves is the key parameter to obtain parametric amplification. In case of phase-matched condition, θ is approximately $\pi/2$ and substituting its value in Eq. (2.25), the last term can be neglected and the phase mismatch is given by

$$\frac{d\theta}{dz} \approx \Delta\beta + \gamma(2P_p - P_s - P_i) \approx \Delta\beta + 2\gamma P_p \doteq \kappa, \tag{2.26}$$

where $2\gamma P_p$ is the nonlinear phase mismatch and the second approximation is valid only when the amplifier is working in undepleted regime ($P_p \gg P_s$). κ is known as the phase mismatch parameter and it is worth noticing that it depends on P_p.
Phase matching between the wave ($\kappa = 0$) is necessary to obtain the maximum of amplification. Since the nonlinear phase mismatch $2\gamma P_p$ is always positive, the only way to compensate for it is through the linear phase mismatch $\Delta\beta$. This can be obtained by selecting a pump wavelength in the anomalous dispersion regime for which $\Delta\beta < 0$ [8]. Expanding the propagation constant $\beta(\omega)$ in Taylor series around the zero-dispersion frequency ω_0, the linear phase mismatch can be rewritten as

$$\Delta\beta = \left\{ \beta_3(\omega_p - \omega_0) + \frac{\beta_4}{2}\left[(\omega_p - \omega_0)^2 + \frac{1}{6}(\omega_p - \omega_s)^2 \right] \right\} (\omega_p - \omega_s)^2 . \tag{2.27}$$

The linear phase mismatch, around the ZDW, is dependent on both the TOD and FOD and it is plotted in Fig. 2.4 for different values of β_4. The nonlinear phase mismatch is $2\gamma P_p = 10\ \mathrm{km}^{-1}$, the reference wavelength is at 1551 nm and the other parameters are the same as the ones used in Fig. 2.3. Whenever $\kappa = 0$, there is a perfect phase matching between the three waves. As κ depends on the value of $2\gamma P_p$, the intersection points for a given $\Delta\beta$ are also depending on it. This results in a power-dependence of the wavelengths at which a perfect phase matching is obtained. Furthermore, it can be seen how β_4 influences the amplification bandwidth as it is explained further down in this section. For signal wavelengths close to the pump wavelength 1551 nm, the difference between the phase mismatch curves for different values of β_4 is small, but as the signal is tuned away from the pump wavelength, the FOD affects strongly the phase matching. In fact, it can be observed that the number of intersections between the phase mismatch curve and $\kappa = 0$ increases for positive β_4 with respect to the negative or zero values. For positive β_4, two other phase matched wavelengths are available

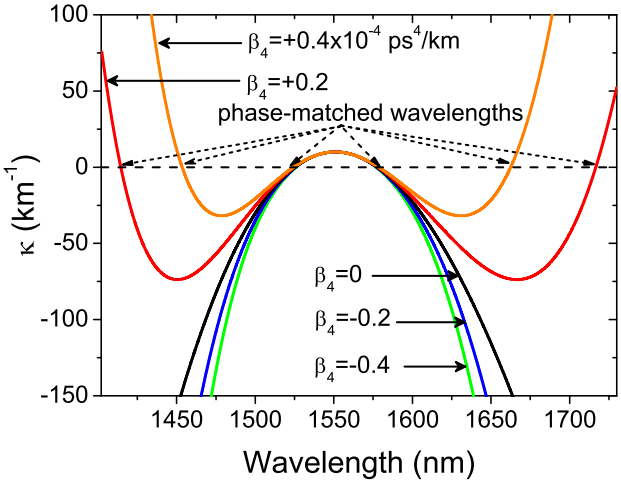

Figure 2.4: Phase mismatch parameter as a function of wavelength for different values of β_4. *Courtesy of Zohreh Lali-Dastjerdi*

farther away from the pump wavelength with respect to those obtained for $\beta_4 \leq 0$. Therefore, the FOD affects also the amplification bandwidth. Broader and flatter amplification bandwidths can be obtained for positive values of β_4. Anyway, the FOD in standard HNLF is typically of the order of 10^{-4} ps$^4 \cdot$ km^{-1} and can therefore be neglected over a bandwidth of less than 100 nm, in which case the linear phase mismatch can be approximated as

$$\Delta\beta = -\frac{2\pi c}{\lambda_0^2}\frac{dD}{d\lambda}\left(\lambda_p - \lambda_0\right)\left(\lambda_p - \lambda_s\right)^2, \tag{2.28}$$

where λ_0, λ_p and λ_s are the ZDW, the pump wavelength and the signal wavelength, respectively. This approximation is valid only for bandwidths where $\lambda_p - \lambda_s \ll \lambda_p$ and in case the approximation $\omega_i - \omega_j = 2\pi c/\lambda_0^2(\lambda_j - \lambda_i)$ is introduced.

As mentioned, the pump wavelength should be placed in the anomalous dispersion regime to compensate for the nonlinear mismatch. This process, in which the GVD ($\Delta\beta$) is negative and is, thus, balanced by the nonlinear Kerr effect ($2\gamma P_p > 0$) is called modulation instability (MI).

2.4.3 Modulation Instability

Modulation instability (MI) is a process in which the amplitude and the phase modulations of an electromagnetic wave grow exponentially because of the interplay between nonlinearities and anomalous dispersion. MI was studied during the 1960s in different fields such as fluid dynamics [52, 53], plasma physics [54] and nonlinear optics [55]. In optical fibers it has been analyzed numerically for the first time in 1980 by Hasegawa and Brinkman [56] and demonstrated experimentally in 1986 by Tai et al. [57].
MI is based on degenerate FWM and is the basis of parametric amplification. In fact, a pump wave at frequency ω_p propagating in the anomalous GVD regime would interact with vacuum fluctuations and develop sidebands centered at $\omega_p \pm \Omega_s$ [8]. The gain spectrum is symmetric with respect to ω_p and the frequency shift Ω_s at which the maximum gain is obtained depends on the input pump power P_p. Ω_s can be expressed as

$$\Omega_s = \pm \left(\frac{2\gamma P_p}{|\beta_2|} \right)^{1/2}, \tag{2.29}$$

where β_2 is the second-order dispersion and γ is the fiber nonlinear coefficient. The gain peak value is given by

$$g(\Omega_s) = 2\gamma P_p. \tag{2.30}$$

The MI gain spectrum is shown in Fig. 2.5 for different values of pump power ($P_p = P_0$). Two sidelobes are formed as a result of FWM that is phase-matched by the nonlinear process of self-phase modulation and both the maximum gain frequency and peak value increase with the input pump power. The frequency shift Ω_s is in the range $1 - 10$ THz for pump powers ranging within $1 - 100$ W. MI has been used as a method to generate a train of soliton pulses with a controllable pulse width and repetition rate [59] and also as a method to convert the wavelength of femtosecond pulses from the 1.5 μm to the 1.3 μm spectral region [60].

2.4.4 Parametric Gain and Amplification Bandwidth

The parametric gain arises from MIwhen a weak signal is propagating along the fiber together with a strong pump. The propagation of the pump, signal and idler can be described by the coupled amplitude equations described in section 2.4.1, usually solved numerically. However, under the assumption of

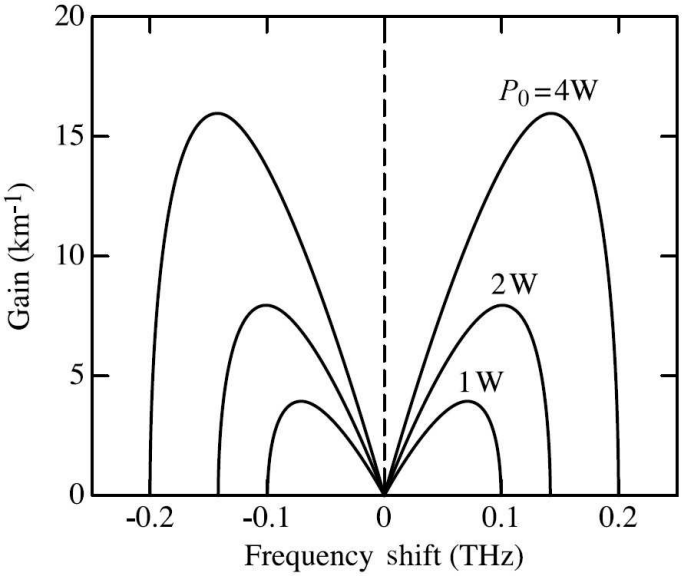

Figure 2.5: Modulation instability gain spectrum. From [58].

undepleted pump (i.e. the pump power incident at the fiber input is much stronger than the signal power), the equations can be solved analytically and a solution of the signal ($P_s(L)$) and idler ($P_i(L)$) powers at the output of the fiber, assuming no loss, can be derived according to

$$P_s(L) = P_s(0)\left(1 + \left[\frac{\gamma P_p}{g}\sinh(gL)\right]^2\right), \tag{2.31}$$

$$P_i(L) = P_s(0)\left[\frac{\gamma P_p}{g}\sinh(gL)\right]^2. \tag{2.32}$$

L is the fiber length and g is the parametric gain coefficient expressed as

$$g^2 = \left[(\gamma P_p)^2 - (\kappa/2)^2\right] = -\Delta\beta\left[\frac{\Delta\beta}{4} + \gamma P_p\right]. \tag{2.33}$$

The unsaturated signal gain is thus given by

$$G_s = \frac{P_s(L)}{P_s(0)} = 1 + \left[\frac{\gamma P_p}{g}\sinh(gL)\right]^2 \tag{2.34}$$

and it is shown in Fig. 2.6. It is noted that, for a fixed pump frequency

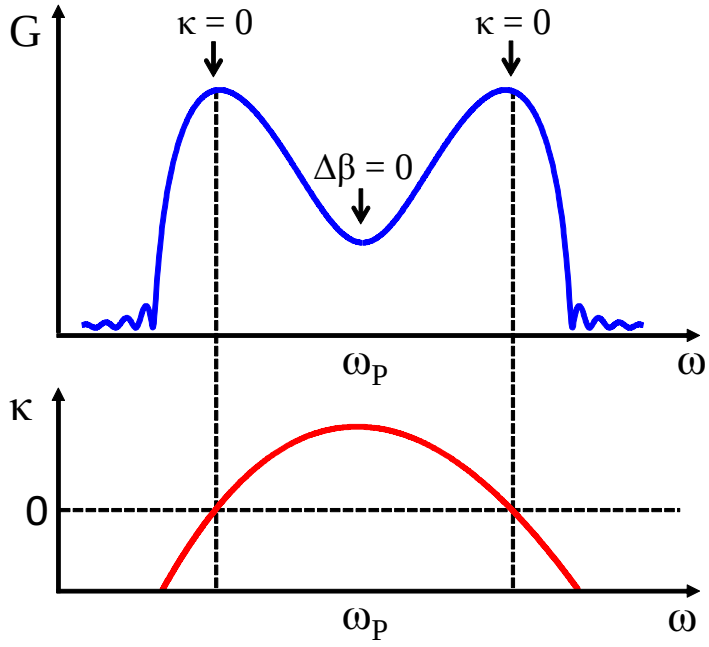

Figure 2.6: Parametric gain and phase-mismatch factor spectra in a single-pump FOPA.

in the anomalous dispersion regime, the gain as a function of the signal frequency is formed by two lobes in each side of the pump, having maxima at signal frequencies for which $\kappa = \Delta\beta + 2\gamma P_p = 0$. In two cases the signal gain in Eq. (2.34) can be simplified. The first case corresponds to signal frequencies close to the pump frequency for which $\Delta\beta \approx 0$; the signal gain can thus be approximated by

$$G_s \approx (\gamma P_p L)^2 . \tag{2.35}$$

The second case is the case for which perfect phase-matching is obtained, $\kappa = 0$, and $\gamma P_p L \gg 1$. The signal gain can then be written as

$$G_s \approx \frac{1}{4} \exp(2\gamma P_p L) . \tag{2.36}$$

Equation (2.36) shows that the maximum gain increases exponentially with $\gamma P_p L$. This is shown in the following subsections, where both a numerical and an experimental characterization of the FOPA have been performed. The gain bandwidth can be defined in terms of linear phase-mismatch $\Delta\beta$

as the separation between the two signal frequencies at which maximum gain is achieved [49]. As a first approximation, the gain bandwidth corresponds to g being real, which implies $-4\gamma P_p \leq \Delta\beta \leq 0$. This shows that, for larger γ and P_p, a larger range of values for $\Delta\beta$ is tolerable. Therefore, a larger wavelength difference between the pump and the signal can be tolerated, which implies amplification over a broader bandwidth. An expression for the gain bandwidth can be found considering the expansion of the propagation constant β in power series up to the fourth-order about ω_p

$$\Delta\beta = \beta_2(\omega_p)(\omega_s - \omega_p)^2 + \frac{\beta_4(\omega_p)}{12}(\omega_s - \omega_p)^4. \tag{2.37}$$

This expression for $\Delta\beta$ can be related to Eq. (2.27) and (2.28) considering that near ω_0, the approximation $\beta_2 \approx \beta_3(\omega - \omega_0)$ is valid. Eq. (2.37) shows that $\Delta\beta$ depends only on the even dispersion terms and on $(\omega_s - \omega_p)^2$, implying that the gain is always symmetric about the pump frequency, as can also be seen from Fig. 2.6. Since β_2 is the dominant term, it has to be reduced in order to obtain small $\Delta\beta$ and larger bandwidths. This can be done by keeping the pump wavelength close to the ZDW at which $\beta_2 = 0$. However, in this case, the gain spectrum is really sensitive to every small variation in the difference $\lambda_p - \lambda_0$, which is common to have in practice. The effect of ZDW variations along the fiber on the parametric gain is shown in the experiment at the end of this section.
Considering that β_4 is usually small, as mentioned in Sec. 2.4.2, it can be neglected and the amplification bandwidth can be calculated as

$$\Delta\omega = 2\sqrt{\frac{2\gamma P_p}{|\beta_2|}}. \tag{2.38}$$

Eq. (2.38) shows that $\Delta\omega$ as well as $\Delta\beta$ scales with the pump power. This dependence of the FOPA gain bandwidth on the pump power is what makes it possible to achieve really broadband amplification in FOPAs. The FOPA gain and bandwidth are characterized both numerically and experimentally in the following part of this section.

Numerical results

The coupled amplitude equations for single-pump phase-insensitive fiber optical parametric amplifier (PI-FOPA) (2.19)-(2.21) are solved numerically using the Matlab function *ode45*. The parameters used in the simulation

Parameter	Unit	Value		
Length	m	300	400	500
D @ 1550 nm	ps/(nm · km)	-0.15	-0.16	-0.16
$dD/d\lambda$ @ 1550 nm	ps/(nm^2 · km)	0.018	0.018	0.018
ZDW	nm	1558.6	1558.9	1558.8
A_{eff} @ 1550 nm	µm^2	11.2	11.2	11.2
γ	(W km)$^{-1}$	11.9	11.9	11.9
α	dB/km	0.8	0.8	0.8

Table 2.1: DSF-HNLF parameters. The dispersion parameters are calculated by OFS-Fitel Denmark based on measurement of the relative group delay.

are listed in Tab. 2.1 and are the same used in the experiment described in the next section. DSF-HNLFs are provided by OFS-Fitel Denmark and three different fiber lengths are used to vary the waves interaction length in order to characterized the fiber optical parametric amplifier (FOPA) gain dependence on the fiber length. Considering Eqs. (2.34) and (2.33), for a fixed fiber (γ and L), the parametric gain depends on two main parameters: the pump wavelength λ_p through the linear phase-mismatch $\Delta\beta$ and the pump input power P_p. Selecting the fiber length of 400 m, the parametric gain is calculated first for different input pump powers at $\lambda_p = 1565$ nm and the results are shown in Fig. 2.7. The choice of pump wavelength are based on the experimental results and is explained at the end of the next subsection. A low input signal power is considered ($P_s = -22$ dBm) in order to satisfy the condition of undepleted pump ($P_p \gg P_s$), for which the approximations previously considered in the section are valid.

Two main effects due to the increase in the pump power are observed. First, as expected from Eq. (2.9), the phase-matched wavelengths are shifted to longer distances from the pump wavelength, since $\Delta\beta$ should compensate for an increase in the nonlinear phase-mismatch ($2\gamma P_p$). This implies that also the amplification bandwidth is broadened, since it depends on the pump power as described in Eq. (2.38). The second effect is the exponential increase of the parametric gain at the phase-matched frequencies, confirming the theoretical prediction. This is better seen in Fig. 2.8, where the peak gain values in Fig. 2.7 are plotted as a function of the input pump power. An exponential fit curve is used to highlight the exponential dependence.

A second set of calculations has been performed for 400 m-long fiber, keep-

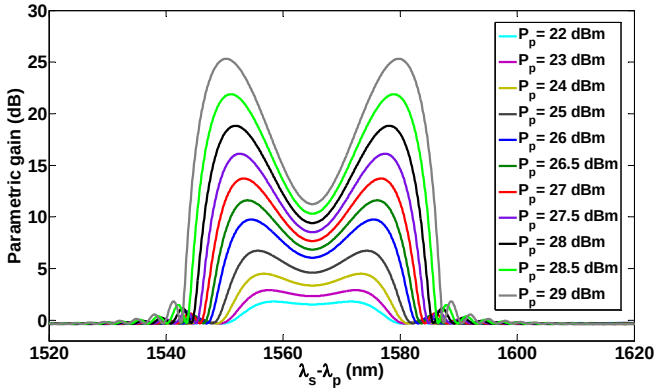

Figure 2.7: Parametric gain for different pump input powers P_p. The simulated data are obtained for a fiber length of 400 m and a pump wavelength $\lambda_p = 1565$ nm. The signal input power is $P_s = -22$ dBm.

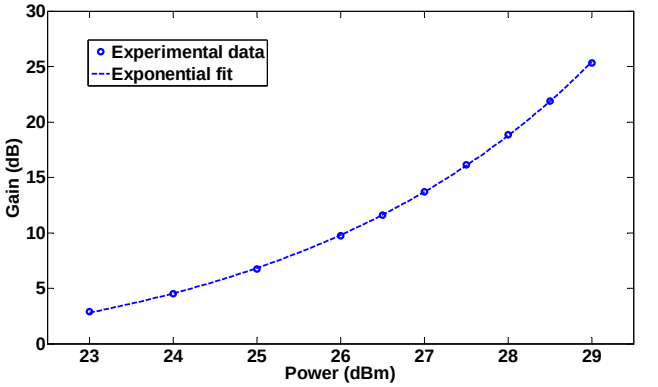

Figure 2.8: Gain value at the phase-matched frequencies for different pump input powers P_p. The simulated data are obtained for a fiber length of 400 m and a pump wavelength $\lambda_p = 1565$ nm. The signal input power is $P_s = -22$ dBm.

ing the pump power at 28 dBm and varying instead the pump wavelength. The calculated gain curves are shown in Fig. 2.9.

As in Fig. 2.7, a shift of the phase-matched frequencies can be observed, because of the linear phase mismatch $\Delta\beta$ dependence on the pump wavelength. For the same reason, a broader amplification bandwidth can be obtained for a pump wavelength closer to the ZDW. However, the simulations are not taking into account the ZDW variations along the fiber, which

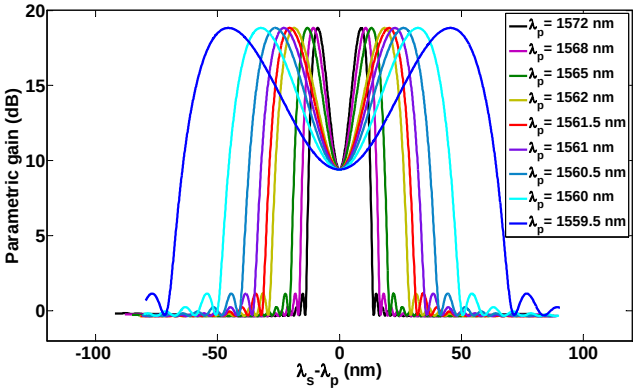

Figure 2.9: Parametric gain for different pump wavelengths λ_p. The simulated data are obtained for a fiber length of 400 m and a pump power $P_p = 28$ dBm. The signal input power $P_s = -22$ dBm.

affect the parametric gain. In particular, for pump wavelengths close to the ZDW, a small variation in the difference $\lambda_p - \lambda_0$ changes the parametric gain significantly. This is shown in the experimental results, where this effect can be observed.

As it can be seen from Eq. (2.34, a third parameter affects the parametric gain, that is the fiber length L. For this reason, a third set of calculations is run, fixing the pump power and the pump wavelength and changing the fiber length. The obtained parametric gain spectra is, thus, compared for three different lengths: $L = 300$ m, $L = 400$ m and $L = 800$ m (obtained in the experiment by splicing together the 300 m and 500 m fiber spools). The numerical results are shown in Fig. 2.10 for a pump wavelength $\lambda_p = 1565$ nm and pump power of 28 dBm, in case of 300 and 400 m-long fiber, and 27 dBm in case of 800 m. The choice to use a smaller power in case of 800 m-long fiber is explained in the section discussing the experimental results.

A relative scaling of the gain peak value is observed, while the position of the phase-matched frequencies is unaffected. In accordance to Eq. 2.38, the bandwidth of the FOPA does not depend on the fiber length.

All the numerical results so far discussed confirm the theoretical prediction. The following step is to compare the theory and the simulated data with experimental results. Therefore, a FOPA characterization experiment has been performed.

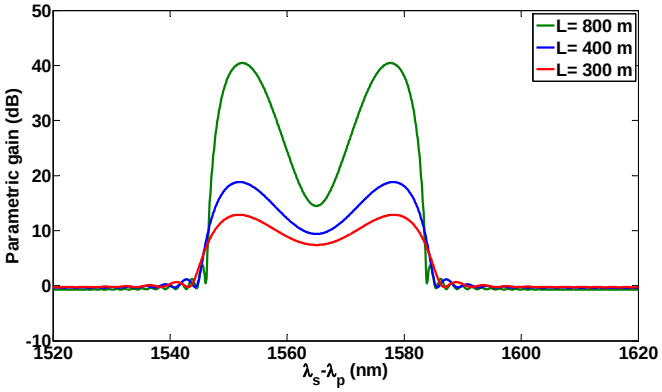

Figure 2.10: Parametric gain for different fiber lengths L. The simulated data are obtained for a pump wavelength $\lambda_p = 1565$ nm and $P_p = 28$ dBm for $L = 300$ m and $L = 400$ m and $P_p = 27$ dBm for $L = 800$ m. The signal input power $P_s = -22$ dBm.

Experimental results

Three sets of measurements have been performed. The parametric gain spectrum has been measured upon the variation of fiber length, pump power and pump wavelength. The experimental setup used to characterize the single-pump FOPA is schematically shown in Fig. 2.11. A CW tun-

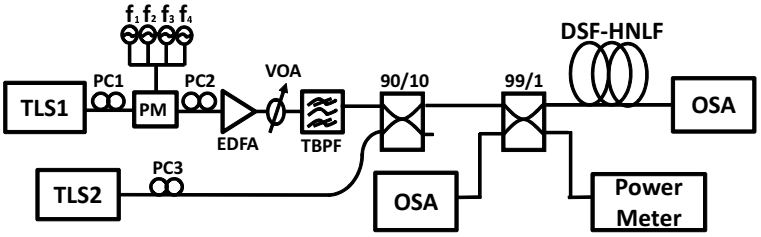

Figure 2.11: Experimental setup of the single-pump FOPA.

able laser source (TLS1) is used as pump source and is subsequently phase modulated to broaden its spectrum in order to increase the stimulated Brillouin scattering threshold. Four combined radio-frequencies (RFs) are used, namely $f_1 = 100$ MHz, $f_2 = 300$ MHz, $f_3 = 900$ MHz and $f_4 = 2800$ MHz. This SBS suppression technique using phase modulation is described in Sec. 2.5. A polarization controller (PC1) is used to align the polarization

of the pump with the phase modulator. The pump is, then, amplified to different power levels by means of an erbium-doped fiber amplifier (EDFA) and a tunable optical bandpass filter (TBPF) with a 2-nm full-width at half-maximum bandwidth is used to suppress the out-of-band amplified spontaneous emission introduced by the EDFA. A variable optical attenuator (VOA) is used to change the pump power level. Another CW TLS (TLS2) is used as signal source and two other polarization controllers (PC2 and PC3) are used to align the polarization of the pump and the signal to achieve the maximum amplification, since the parametric gain is polarization dependent [28, 62]. The pump and the signal are combined by a 10 dB coupler. A 20 dB coupler is used before the DSF-HNLF to monitor the input power and to measure the back reflected power due to the SBS. The pump and the signal are, then, launched into the DSF-HNLF (fiber parameters for the three lengths listed in Tab. 2.1) and the output spectrum is measured by an optical spectrum analyzer (OSA). The signal wavelength was tuned in the range 1520-1620 nm allowed by TLS2.
The first set of measurements is meant to characterized the dependence of the parametric gain from the input pump power and the results are shown in Fig. 2.12. The measurements of the on/off gain, i.e. the difference between the power spectra when the pump is switched on and off, are performed with the pump wavelength at 1565 nm and for a fiber length of 400 m. As

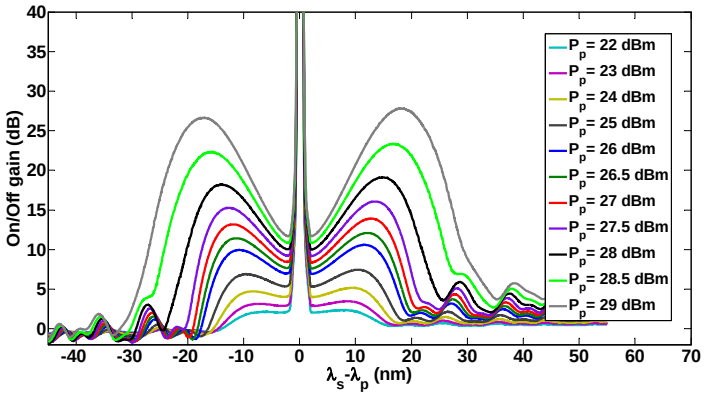

Figure 2.12: Measured on/off gain spectra for different pump input powers P_p as a function of the separation between the signal and the pump wavelengths. The measurement are performed for a fiber length of 400 m and a pump wavelength $\lambda_p = 1565$ nm.

observed in the results of the numerical analysis in the previous subsection,

two main effects due to the increase in pump power are observed. First, the separation between the two phase-matched wavelengths grows and, thus, the amplification bandwidth is increased. Second, the parametric gain peak values increase exponentially with the pump power. As it can be observed in Fig. 2.12, however, a third effect can be noticed that was not observed in the numerical results, that is a small asymmetry of the gain spectrum with respect to the pump wavelength. For signal wavelengths longer than the pump wavelength a slightly higher gain is observed. This is due to the effect of SRS and is discussed in Sec. 2.6.
The results of the measurements performed while changing the fiber length are shown in Fig. 2.13 for a pump wavelength $\lambda_p = 1565$ nm and pump powers of 28 dBm for the 300 m and 400 m-long fibers and $P_p = 27$ dBm for $L = 800$ m. A smaller power was considered for the length of 800 m in order to reduce the impact of SBS. As expected, the parametric gain

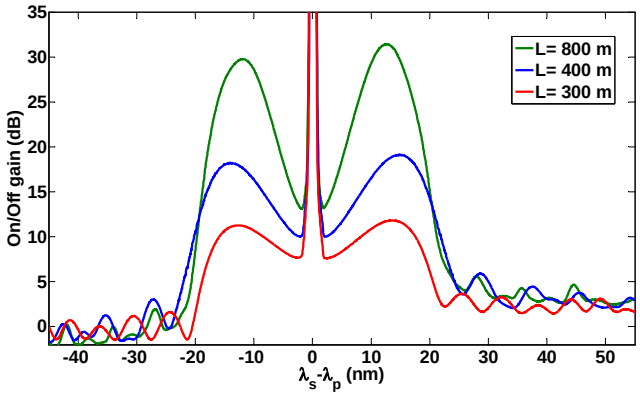

Figure 2.13: Measured on/off gain spectra for different fiber lengths L as a function of the shift between the signal and the pump wavelengths. The measurement are performed for a pump wavelength $\lambda_p = 1565$ nm and $P_p = 28$ dBm for $L = 300$ m and $L = 400$ m and $P_p = 27$ dBm for $L = 800$ m.

increases for longer fiber, while the bandwidth is unaffected. In particular, considering the 300 m and 400 m-long fibers, the phase-matched frequencies do not show a shift far from the pump wavelength. For a length of 800 m, a small shift is observed because of the slightly smaller pump power.
In the last set of measurements, the dependence of the parametric gain on the pump wavelength, with particular focus on the separation $\lambda_p - \lambda_0$, was investigated. The obtained results are shown in Fig. 2.14. A broadening of the amplification bandwidth for a smaller distance $\lambda_p - \lambda_0$ can be ob-

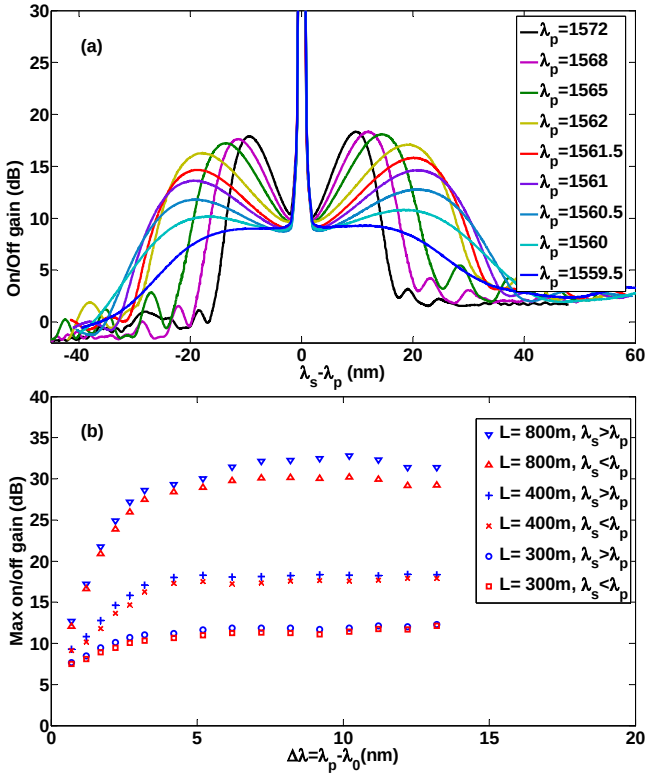

Figure 2.14: (a) Measured on/off gain spectra for different pump wavelengths λ_p as a function of the separation between the signal and the pump wavelengths. The measurements are performed for a fiber length of 400 m and a pump power at the input of the DSF-HNLF $P_p = 28$ dBm. (b) Measured values of the parametric gain at the phase-matched frequencies (λ_{max}) as a function of the separation between the pump wavelength and the ZDW $\Delta\lambda = \lambda_p - \lambda_0$ for different fiber lengths (L).

served in Fig. 2.14(a). The same effect was seen in the numerical results. However, another effect is present in the measured gain spectra, which was not observed in the simulated data. In fact, in the numerical results shown in Fig. 2.9, the peak value of the gain was unaffected by the variation in the pump wavelength, whereas in the measurements a clear decrease of the parametric gain can be observed, implying a higher flatness of the gain spectrum. This is due to longitudinal fluctuations of the ZDW, that needs to be taken into account and modeled [63, 64]. The fluctuations arise from technical limitations in the manufacturing process of fibers, which results

in a core diameter which is not constant along the fiber length [65]. This effect is even stronger for HNLFs, since they have smaller diameter [66, 67]. Fluctuations of ±1 nm have been measured along few kilometers of HNLF [47]. The peak values of the gain are shown in Fig. 2.14(b) as a function of the separation $\Delta\lambda = \lambda_p - \lambda_0$ for the three different fiber lengths considered here. Both the gain maxima for $\lambda_s < \lambda_p$ and $\lambda_s > \lambda_p$ are considered, showing the contribution due to SRS. It can be seen that for a separation $\Delta\lambda = \lambda_p - \lambda_0 \approx 4$ nm the gain reaches its maximum value and stabilizes with respect to the ZDW variations. Based on this observation, the pump wavelength for the numerical investigation and for the previous measurements was chosen 6 nm away from the ZDW, in order to provide a gain over a broad bandwidth, but without reducing the maximum gain attainable. It is also noted that, the shortest lengths experience a smaller decrease in the gain than the 800 m fiber, whose gain decrease of 20dB. Furthermore, the difference of the peak values between the higher-wavelengths lobe ($\lambda_s > \lambda_p$) and the lower-wavelengths lobe ($\lambda_s < \lambda_p$) increases with an increasing length. This is due to the dependence of the Raman gain on the interaction length, that is discussed in Sec. 2.6. The importance of having a flat gain is an issue for the employment of FOPAs in wavelength division multiplexing (WDM) systems, where each channel needs to be amplified by the same gain. Several demonstrations of amplification of WDM channels using single-pump configurations have been presented [68–70]. A way to increase the flatness of the gain spectrum would be to increase the bandwidth by increasing the pump power, but this is limited by SBS and, therefore, short fibers need to be employed. N. El Dahdah *et al.* in [69] reported an amplification up to 20 dB by using a really short fiber of 114 m with 35 dBm of pump power.

2.5 Stimulated Brillouin Scattering

Stimulated Brillouin scattering is a high-gain nonlinear process, based on the inelastic scattering due to the interaction between photons and acoustic phonons. An intense beams propagating in a medium, such as an optical fiber, may produce acoustic vibrations in the medium. Because of these vibrations the beam is partly reflected back by thermally excited acoustic waves. For SBS a power threshold can be defined as the value P_{th} for which the reflected power becomes a certain fraction of the input power. Common fractions are 1 and 10% of the input power [71].

For silica fibers, the Brillouin frequency shift between the propagating beam and the reflected beam is of the order of $10 - 20$ GHz, and the Brillouin gain has an intrinsic bandwidth of typically 50 MHz, which is determined by the strong acoustic absorption (short phonon lifetime). SBS introduces the most stringent power limit for the amplification and the passive propagation of narrow-band optical signals in fibers. In fact, since in FOPAs a high pump power is needed to amplify the weak signal, in order for the FOPA to operate properly SBS needs to be suppressed. Thus, the power threshold has to be increased. Several techniques to increase the threshold have been demonstrated. For example, it is possible to broaden the linewidth of the light beyond the Brillouin gain bandwidth, since the pump frequency component falling outside the Brillouin gain bandwidth (50 MHz) do not generate SBS gain [72, 73].
A common technique to increase the pump linewidth is by phase or frequency modulation. This is the technique used in all the experiments described in the following chapters. A schematic of the SBS suppression setup is shown in Fig. 2.15. Up to four combined radio-frequencies (RFs) are

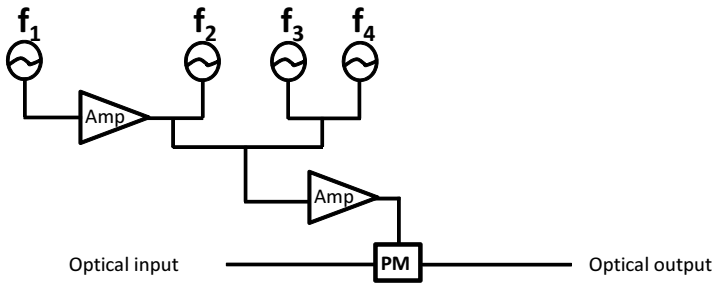

Figure 2.15: Phase modulation setup for SBS suppression. PM: phase modulator. Amp: RF amplifier. $f_1 = 100$ MHz, $f_2 = 300$ MHz, $f_3 = 600$ MHz and $f_4 = 3000$ MHz.

used to broaden the pump linewidth, corresponding to $f_1 = 100$ MHz, $f_2 = 300$ MHz, $f_3 = 900$ MHz and $f_4 = 2800$ MHz. The frequency values were selected by optimizing the back-scattered power to reach its minimum level. The RF signals are combined and subsequently amplified by means of a RF amplifier to reach the right amplitude of the combined RF signals providing the minimum reflected power.
The integrated reflected power is measured by an OSA connected to the 20 dB coupler as shown in Fig. 2.11. Three different RF signal configurations were considered. In particular, the SBS threshold has been mea-

sured using all four RF signals, using only three frequency generators ($f_1 = 100$ MHz, $f_2 = 300$ MHz and $f_3 = 900$ MHz) and without phase modulation. The results are shown in Fig. 2.16. It can be seen that for

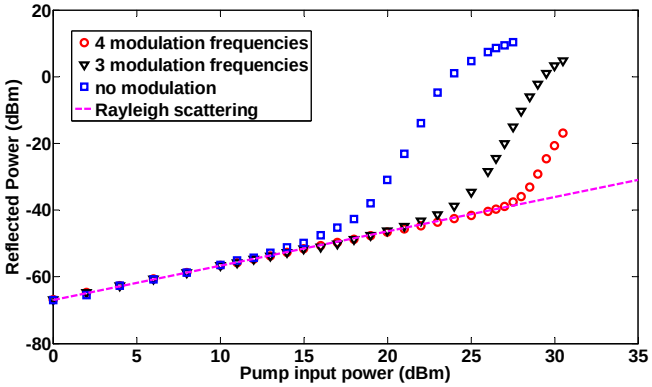

Figure 2.16: Measured reflected power as a function of the power at the input of the DSF-HNLF for different frequency configurations in the SBS suppression scheme. The pump wavelength was fixed at 1564 nm and a fiber length of 400 m was selected (see Tab. 2.1 for fiber specifications).

small input power, the elastic scattering (Rayleigh scattering) is the dominant contribution to the reflected power. By increasing the input power, the reflected power grows linearly until a given value P_{th} of the input power is reached, which corresponds to the SBS threshold for which the reflected power does not depend anymore linearly on the input power. The power threshold is moved from 15 dBm of input power (without SBS suppression) up to 24 dBm and 28 dBm for the case of three and four RF signals, respectively.

The back-scattered spectra corresponding to the case of no phase modulation and phase modulation using three frequency generators are shown in Fig 2.17(a) and (b), respectively. From Fig. 2.17, it can be seen that the Rayleigh-scattered light at the pump frequency depends linearly on the input power and for low input powers no SBS reflected light is visible. However, after the threshold has been reached, the rapid increase of the SBS power (shifted approximately of 10 GHz with respect to the Rayleigh peak) is observed.

Other techniques than the increase of the linewidth of the pump source have been implemented to reduce the stimulated Brillouin scattering. For example, attempts to reduce the overlap between guided optical and acoustic

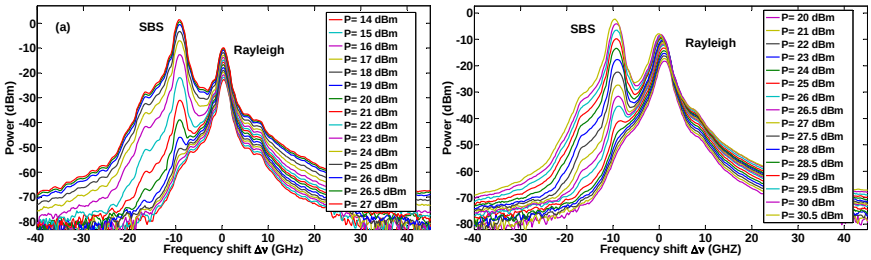

Figure 2.17: Reflected power spectra as a function of the frequency shift from the pump frequency ($\Delta\nu = \nu - \nu_p$) for (a) no phase modulation and (b) phase modulation using three RF signals ($f_1 = 100$ MHz, $f_2 = 300$ MHz and $f_3 = 600$ MHz).

modes by means of novel designs for HNLFs were also reported. Traditional GeO_2 doped fibers with particular designs of the refractive index profile can increase the SBS threshold, having larger acousto-optic effective area [74, 75]. Al_2O_3 doped fibers have also been proposed because they increase the SBS threshold by lowering the acoustic index of the core while increasing the optical index [76], but they also introduce higher losses with respect to standard HNLFs. It has been demonstrated that both methods can increase the SBS threshold by approximately 6 dB. Another technique used to change the acoustic guiding of the optical fiber is to apply a liner or stepwise strain to the fiber [77, 78], increasing the SBS threshold of approximately 7 dB.

2.6 Stimulated Raman Scattering

Stimulated Raman scattering (SRS) is a nonlinear process, based on inelastic scattering due to the interaction between photons and optical phonons. When an intense pump propagates along a fiber, the nonlinear response is fast (order of fs), but not instantaneous, owing to the vibrations of glass lattice. The vibrational response in silica fibers occur over a time scale of 60-70 fs. As a consequence of the vibrational state of the molecule, a small part (typically $\sim 10^{-6}$) of the power of the pump can be transfer to a signal that is frequency down-shifted with respect to the pump. The peak of the Raman gain is frequency down-shifted by approximately 13.2 THz and the Raman gain spectrum is several terahertz wide (up to 40 THz). The Raman gain coefficient g_R is approximately 10^{-13} m/W at 1550 nm and is

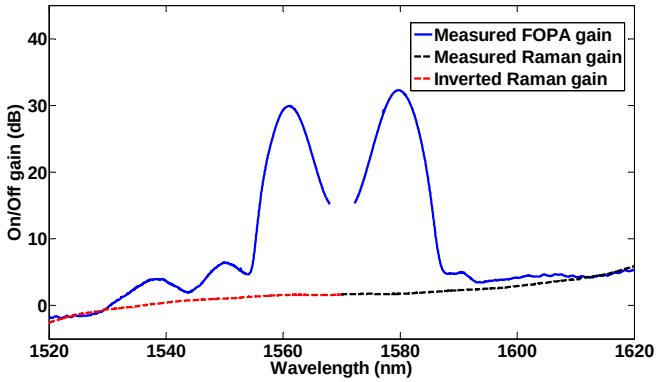

Figure 2.18: Measured Raman gain (dashed blue line), inverted Raman gain (red dashed line) and FOPA gain (solid line) as a function of the difference between the signal and the pump wavelengths. The measurements are performed in the 800 m-long fiber for $P_p = 28$ dBm and pump wavelengths of 1570 nm and 1535 nm for the FOPA and Raman gain respectively.

inversely dependent on the pump wavelength. In the small-signal regime, the Raman gain can be approximated by

$$G_A = \exp\left(\left(g_R/A_{eff}\right) P_p L_{eff}\right) \tag{2.39}$$

where P_p is the pump power and L_{eff} is the effective fiber length, calculated as $L_{eff} = \left[1 - \exp(-\alpha L)\right]/\alpha$, where α is the fiber loss and L is the fiber length. This shows the dependence of the Raman gain on the interaction length, confirming the experimental results, in which the gain spectrum asymmetry is higher for longer fibers. The Raman gain depends also on the pump power and, since in FOPAs a high pump power is required, it becomes relevant to characterize the Raman gain in experimental FOPA setups. The FOPA and Raman gains were measured for $P_p = 28$ dBm in the 800 m-long fiber. The results are shown in Fig. 2.18. The inverted Raman gain is obtained by mirroring and inverting the measured Raman gain and it was plotted together with the Raman gain to show the asymmetry of Raman response, which amplifies the longer wavelengths at the expense of the shorter one. The comparison between the FOPA and Raman gain spectra shows a good correspondence, demonstrating that the asymmetry observed in the FOPA gain spectrum in the experimental results is due to SRS.

2.7 Summary

In this chapter an overview of single-pump fiber optical parametric amplification has been provided. First, nonlinearities and nonlinear processes in fibers have been introduced, focusing on the four-wave mixing process, on which parametric amplification is based. Secondly, the parametric gain and amplification bandwidth have been characterized both numerically and experimentally, validating the theory discussed in the chapter. In particular, the phase-matching condition and its effects on the parametric gain spectrum have been discussed. The dependence of the parametric amplification on fiber parameters and pump parameters has also been shown in simulations and experiments. Furthermore, stimulated Brillouin scattering has been introduced, along with the suppression technique based on phase modulation of the pump signal. A brief description of stimulated Raman scattering and its effect on parametric gain have also been covered.

Chapter 3

Intensity Modulation Transfer in Single-Pump Phase-Insensitive FOPAs

3.1 Introduction

The major noise contribution in fiber optical parametric amplifiers (FOPAs) has been identified in the pump-to-signal intensity modulation transfer (IMT) [14, 79]. In continuous wave (CW) pumped FOPAs, the pump intensity modulation (IM) arises at low and high frequency, up to few GHz, because of different distinct processes. The low frequency contribution originates from the relative intensity noise (RIN) of the pump laser source, inducing fluctuations of the pump intensity that are transferred to the amplified signal. Another contribution at low frequency is due to the amplified spontaneous emission (ASE) of the erbium-doped fiber amplifier (EDFA) used to boost the pump signal. Optical filters are used to reduce the ASE noise generated by EDFAs, but the residual ASE causes fluctuations in the pump power. As for the high frequency contributions, the stimulated Brillouin scattering (SBS) suppression plays an important role in CW pumped FOPAs. In fact, the suppression is usually done by phase modulation of the pump to broaden its linewidth and thereby increase the SBS threshold (see Sec. 2.5 in Chap. 2). However, the phase modulation may induce a residual pump intensity modulation, which will modulate the signal gain and idler conversion efficiency. Moreover, for high-speed communication

systems, the pump may be intentionally modulated at high repetition rates (several tens or hundreds of GHz) to obtain larger gain and broader amplification bandwidths with respect to CW pumped FOPAs [80]. This induces a pump-to-signal IMT at high frequencies, resulting in a signal distortion mechanism which is critical for optical communication systems. Because of that, the IMT [81] and, in general, the noise figure [82, 83] in single-pump phase-insensitive fiber optical parametric amplifiers (PI-FOPAs) have been widely investigated both theoretically and experimentally in the unsaturated regime and for frequencies up to 10 GHz.
It has also been experimentally demonstrated that saturated FOPAs may work as power level equalizers [51, 84], reducing both the impact of the ASE added to the signal by an EDFA at the input of the FOPA, and the beat noise, i.e. the intrinsic noise coming from the interference between the signal and the spontaneous emission inside the FOPA. In this chapter, the experimental investigation of the pump to signal IMT in single-pump PI-FOPAs is extended to pump modulation frequencies up to 27 GHz and to the gain saturation regime.
In the first of the experimental results presented in this chapter, the FOPA is not saturated and the experimental data are compared to the analytical model introduced by M. E. Marhic *et al.* [81]. Then the saturation regime is investigated and the experimental data are fitted with a numerical model based on a split-step Fourier method implemented by Z. Lali-Dastjerdi [85].
First, a brief overview of the main results of the investigation of the noise figure and IMT in PI-FOPAs is given in Sec. 3.2. The low-frequency IMT analytical model in [81] and the experimental investigation in the unsaturated regime are described in Sec. 3.3. The operation of a single pump PI-FOPAs in the saturation regime is covered in Sec. 3.4 and the experimental characterization of the saturation effects on the IMT is described in Sec. 3.5.

3.2 Noise Figure and Intensity Modulation Transfer in Single-Pump Phase-Insensitive FOPA

The noise figure (NF) in FOPAs has been widely investigated both theoretically and experimentally in unsaturated regime. In theory, a quantum-limited NF (3 dB) can be obtained in PI-FOPAs, for which the NF for the

signal and idler can be defined as

$$NF_{sig} = 1 + \frac{G-1}{G} \approx 2, \tag{3.1}$$

$$NF_{idl} = 1 + \frac{G}{G-1} \approx 2, \tag{3.2}$$

where G is the FOPA signal gain and the high-gain limit approximation ($G \gg 1$) has been considered. However, to reach the quantum-limit, a very low noise pump is required, since the noise is directly transferred to the gain because of the ultra-fast (order of fs) response of the FOPAs. To date, up to four different noise contributions have been reported separately, namely *amplified quantum noise (AQN)*, *residual pump noise*, *Raman seeded spontaneous emission* and *pump transferred noise* [86]. The total noise figure is expressed as the sum of these contributions, where the AQN is the fundamental noise mechanism, leading to the quantum-limit, and the others can be treated as excess noise sources. An example of the total noise in a single-pump PI-FOPA is shown in Fig. 3.1, where the measured spectra at the input and at the output of the FOPA are compared. The amplified

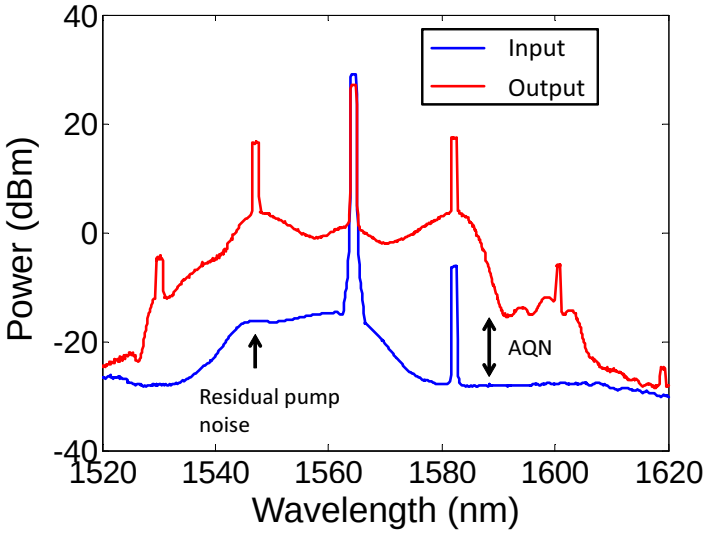

Figure 3.1: Spectra at the input and the output of a single-pump PI-FOPA. AQN: amplified quantum noise.

quantum noise and the residual pump noise, due to an imperfect filtering of the pump at the input of the FOPA, are clearly visible. However, when

applying a good pump filtering, the Raman seeded spontaneous emission and the pump transferred noise have been identified as the major noise factors limiting the performance of FOPAs. Moreover, the main region of interest in single-pump FOPAs is typically at the maximum gain wavelengths where the power flow from the pump to the signal is maximum and the gain depends exponentially on the product of the pump power, the fiber nonlinear coefficient and the fiber length (see Eq. (2.36) in Chap. 2). For typical single-pump FOPAs with broad bandwidths on the order of tens of nanometers, the Raman seeded spontaneous emission noise may be significant at the edges of the gain spectrum, while it is generally insignificant around the maximum gain wavelength and can often be neglected in these regions. This can been seen in Fig. 3.2, where the gain and the NF spectra are calculated with and without Raman contribution. The main

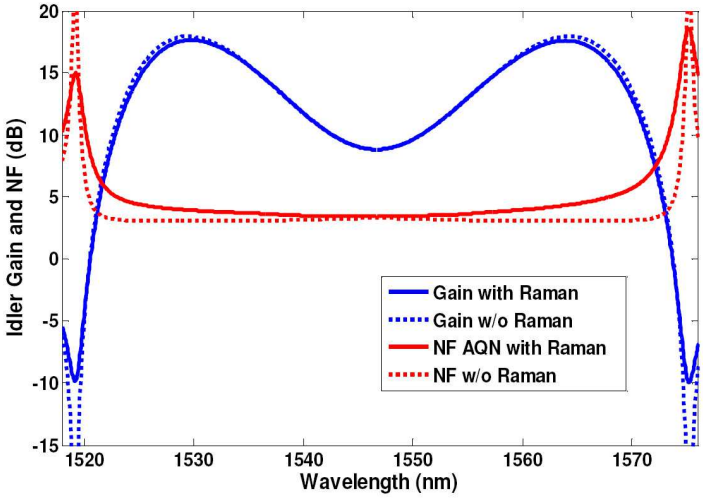

Figure 3.2: Calculated signal gain and NF spectra with or without Raman contribution. From [86].

effect due to the Raman contribution is a sharp NF increase around the gain edge at shorter wavelengths. Therefore, while the Raman contribution can be neglected, the pump transferred noise, i.e. the intensity modulation of the pump transferred to the signal, is significant at the maximum gain wavelengths and consequently becomes the major noise contribution. In fact, the exponential dependence of the amplified signal from the pump power turns small pump power fluctuations into much larger signal and idler power fluctuations. This is discussed in Sec. 3.3, where the analyt-

ical model introduced by Marhic *et al.* [81] is described. The IMT has been investigated for low modulation frequencies and unsaturated FOPAs, demonstrating that the intensity modulation of the signal could reach 10 times that of the pump.
The dependence of the NF on the signal input power and the pump optical signal-to-noise ratio (OSNR) were also demonstrated in the unsaturated regime [87]. A significant increase of the NF with increasing input signal power and with decreasing pump OSNR was shown. In [87], the dependence of the NF on the signal wavelength is also demonstrated, showing that the NF grows with increasing signal wavelength separation from the pump. The same wavelength dependence is shown for the IMT, since the amount of transferred noise, in case of undepleted pump, depends on the derivative of the signal gain with respect to pump power.
Along with the fast nonlinear response and the exponential gain, another important category of effects, influencing the IMT, are the so-called walk-off effects [88], which can improve the OSNR of both the amplified signal and the idler. They are caused by the group-velocity mismatch between the pump and the signal. The walk-off effects can be characterized by introducing the walk-off delay between the pump and the signal as

$$\tau_\omega \approx \beta_3 L \left(\lambda_p - \lambda_s\right)^2 , \tag{3.3}$$

where β_3 and L are the fiber third-order dispersion and length, respectively. Considering τ_c as the pump noise coherence time, for a really small walk-off between the pump and the signal ($\tau_\omega \ll \tau_c$), i.e. for signal and pump traveling with the same group-velocity, the signal and idler experience different pump powers due to the pump intensity fluctuations and, thus, they are amplified by different gains. When, instead, the group-velocity mismatch between the pump and the signal is large enough not to be neglected (τ_ω comparable to or larger than τ_c), the gain experienced by the signal and idler depends on the pump average power. This reduces considerably the IMT transfer, also called RIN transfer. To have a larger reduction of the transfer, the walk-off delay should be higher. The walk-off delay depends on different parameters, including the fiber length. Therefore, to have large τ_ω, L should be big. This means that the RIN transfer is reduced more for longer interaction lengths. From Eq. (3.3) is also clear that the walk-off effects are more significant for signal wavelengths that are farther from the pump, since τ_ω is larger for them. Moreover, the reduction of the RIN transfer is larger for high modulation frequencies of the pump power, since τ_c becomes comparable to τ_ω. The high-frequency averaging effect is shown

in Fig. 3.3 where the RIN spectral density is shown as a function of the noise frequency for different signal wavelengths [88]. The RIN of the signal

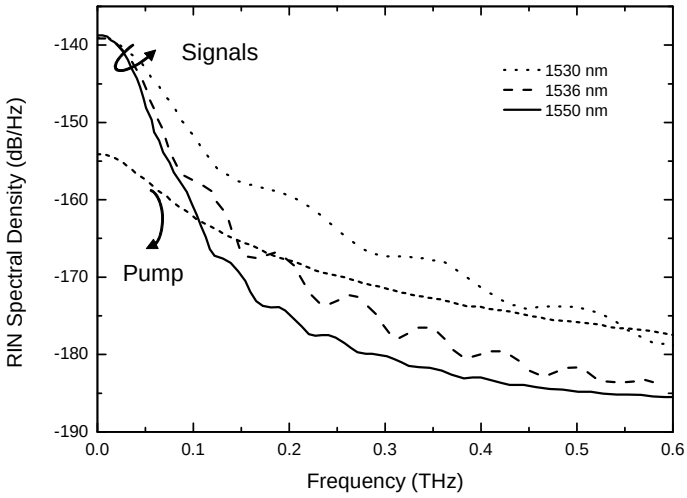

Figure 3.3: RIN spectral density as a function of noise frequency at three signal wavelengths. From [88].

is almost constant for low noise frequencies and also the signal wavelength separation from the pump is not affecting significantly the signal RIN, since τ_c is large enough to neglect the walk-off effects. But the RIN is reduced considerably for noise frequencies over 200 GHz, for which the signal fluctuations are smaller than those of the pump. Also the signal wavelength dependence of the IMT reduction is seen in Fig. 3.3, where the RIN for the signal closer to the pump does not go below the pump RIN, even for really high noise frequencies.

3.3 Low-Frequency Intensity Modulation Transfer

Low-frequency pump-to-signal IMT has been investigated in [81], both theoretically and experimentally, up to a pump modulation frequency of 10 GHz. However, since it has been demonstrated that for higher frequen-

cies the IMT starts to decrease because of walk-off effects, the experimental investigation has been extended up to 27 GHz in this section. The results were presented in [89]. The analytical model introduced in [81], describing the low-frequency modulation transfer in the unsaturated regime, is used to compare the experimental data and is discussed in the following section.

3.3.1 Theory

The theoretical approach is based on the well-known expression for FOPA gain in the small-signal regime (see Eq. (2.34)in Chap. 2), assuming a constant intensity modulation of the pump the fiber in spite of the presence of the parametric gain. Furthermore, to simplify the notations, a quasi-steady-state approach is used by assuming that the pump varies so slowly that it is possible to use the usual steady-state expressions to calculate the gain. This allows to suppress any explicit time dependence and to simply calculate changes in gain by means of derivatives. Thus the pump power P_p and the amplified signal power $P_{s,out}$ can be written as

$$P_p = P_0 \left(1 + m_p\right), \tag{3.4}$$

$$P_{s,out} = G_s P_{s,in} = G_{s0} \left(1 + m_s\right) P_{s,in}, \tag{3.5}$$

where P_0 is the average power, m_p is the intensity modulation index for the pump, G_s is the signal gain, $P_{s,in}$ is the signal input power, G_{s0} is the reference gain, i.e. G_s for $m_p = 0$, and m_s is the signal output intensity modulation index. In order to quantify the intensity modulation transferred from the pump to the signal, the so-called RIN magnification coefficient ρ, defined as the ratio between m_s and m_p, is introduced. Considering the fact that G_s depends on the pump modulation index m_p through P_p as follows

$$G_s = G_{s0} + m_p \frac{dG_s}{dm_p} = G_{s0} + m_p P_0 \frac{dG_s}{dP_p} = G_{s0} \left(1 + m_s\right), \tag{3.6}$$

the relationship between the modulation indices of the pump and the signal can be easily derived, resulting in the following expression for ρ

$$\rho \equiv \frac{m_s}{m_p} = \frac{P_0}{G_{s0}} \frac{dG_s}{dP_p}. \tag{3.7}$$

This shows that the magnification factor essentially varies with the pump power dependence of the gain. Considering the maximum gain region,

the gain exponentially depends on the pump power following Eq. (2.36) in Chap. 2. Therefore, at the maximum gain region, the RIN magnification coefficient becomes

$$\rho \equiv \frac{m_s}{m_p} \propto \frac{dG_s}{dP_p} = \frac{\gamma L}{2} \exp(2\gamma P_p L). \tag{3.8}$$

The exponential growth of the modulation transfer limits considerably the performance of FOPAs.
By solving the system of coupled equations for the three waves involved in single-pump operation of a fiber optical parametric amplifier in the undepleted pump regime (see Eqs. (2.19)-(2.21)in Chap. 2) and differentiating the obtained signal gain G_s with respect to the pump power P_p, it becomes possible to develop a model for the pump-to-signal IMT against to which the experimental results in the next section are compared.

3.3.2 Experimental Investigation of the Low-Frequency Pump-to-Signal Intensity Modulation Transfer

The experimental investigation of the IMT for pump modulation frequencies up to 27 GHz is presented in this section. The pump-to-signal IMT is characterized by applying a small modulation to the pump power corresponding to about the 1% of the average power, and by subsequently evaluating the temporal variations of the output signal. The IMT coefficient ρ is used to quantify the IMT. The two modulation indices of the pump and signal are calculated separately and, then, their ratio is considered. First the setup is described and, then, the results are discussed.

Experimental setup

The experimental setup is shown in Fig. 3.4. A CW tunable laser source (TLS) is used as pump source ($\lambda_p = 1564$ nm) and is subsequently phase modulated using three combined radio-frequencies (RFs) to broaden its spectrum in order to reduce the SBS of the pump. The pump is then intensity modulated with a tunable sinusoidal radio-frequency signal in a Mach-Zehnder modulator with a 28 GHz bandwidth in order to impose intensity fluctuations at different modulation frequencies. The transmission function of the Mach-Zehnder modulator as a function of the applied bias voltage is shown in Fig. 3.5. The modulation strength is chosen such that

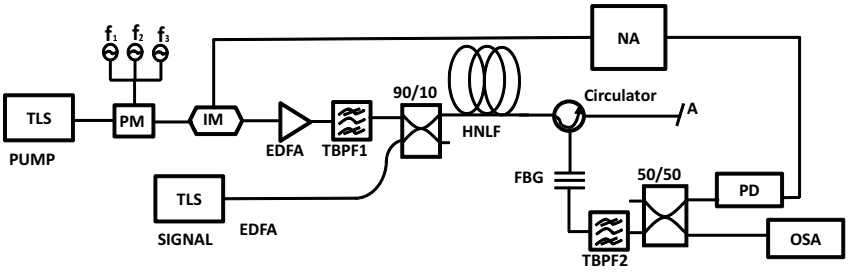

Figure 3.4: Experimental setup of FOPA for pump-to-signal IMT characterization in unsaturated regime. The residual pump is suppressed at location A. IM: Mach-Zehnder modulator.

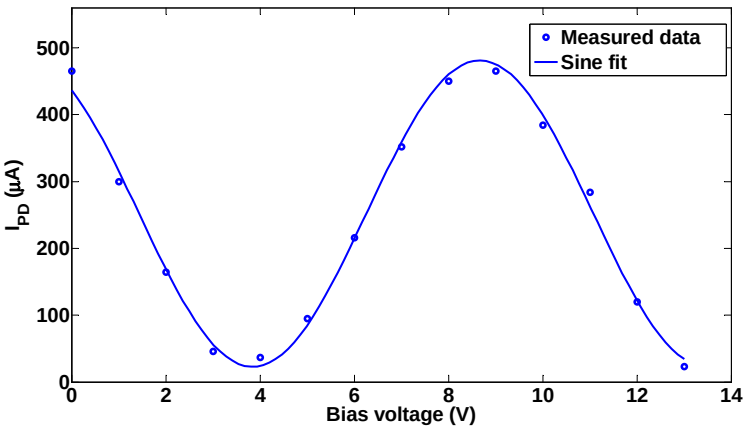

Figure 3.5: Mach-Zehnder transmission curve as a function of the bias voltage applied to the Mach-Zehnder modulator. The data are plotted along with a sine fitting curve.

$m_p = 0.01$ and the intensity modulator is operated at the quadrature point applying a bias voltage of 6 V. The frequencies of the RF signals used for SBS suppression ($f_1 = 100$ MHz, $f_2 = 300$ MHz and $f_3 = 600$ MHz) are distinct from the amplitude modulation frequency imposed on the pump (equal to and above 1 GHz) in order not to impact the results. Once intensity modulated, the pump is amplified to 0.56 W in an EDFA and a tunable optical bandpass filter (TBPF1) with a 2 nm full-width at half maximum (FWHM) is used to suppress the out-of-band amplified spontaneous emission introduced by the EDFA. Another CW TLS is used as signal source and the pump and signal are then combined via a 10 dB

coupler in a 400 m dispersion shifted highly nonlinear fiber (DSF-HNLF), with a zero-dispersion wavelength of 1559.2 nm, a nonlinear coefficient of 11.9 $W^{-1} \cdot km^{-1}$ and a dispersion slope of 0.018 $ps/(nm^2 \cdot km)$. The output signal is, then, selected by means of a fiber Bragg grating (FBG) used in transmission as a notch filter centered at the pump wavelength, followed by an optical bandpass filter (TBPF2) tuned to the signal wavelength. To determine the IMT coefficient, the pump modulation index is measured at the output of the intensity modulator and subsequently compared to the modulation index of the amplified signal measured at the output of the DSF-HNLF. The modulation indices are calculated from the measured S-parameters provided by a network analyzer (NA) after detection by a photodiode (PD) with a 45 GHz bandwidth. To avoid effects, such as saturation, due to the response of the PD, the power at its input is kept small and constant for all the measurements. The modulation index of the pump and the signal respectively, is calculated as

$$m_i = \frac{P_i^{\max} - P_i^{\min}}{P_i^{\text{avg}}} = \frac{\Delta P_i}{P_i^{\text{avg}}}. \tag{3.9}$$

where $P_i^{\max}$, $P_i^{\min}$ and P_i^{avg} are the maximum, minimum and average values of the power, respectively, both for the output signal power ($i = s$) and the input pump power ($i = p$). The peak-to-peak output power variation ΔP_i is extracted from the S-parameters provided by the NA, while the average power P_i^{avg} is obtained from the average value of the photocurrent generated by the high-speed photodiode (see Appendix A).

Results and discussion

First the wavelength dependence of the IMT coefficient is presented. The measured IMT coefficient ρ is shown together with the amplifier signal gain as a function of the signal wavelength in Fig. 3.6, along with the theoretical results obtained as described in Sect. 3.3.1. It can be seen that the IMT coefficient increases with an increasing detuning between the signal and the pump and that the transfer is significant at the maximum gain, which is the region of main interest for FOPAs. A good agreement is obtained between the experimental data and the theoretical results, especially for small detunings of the signal from the pump. However, a small difference is noticed as the separation between the pump and the signal is increased. This is due to the simplified assumptions used in the gain calculation model. In

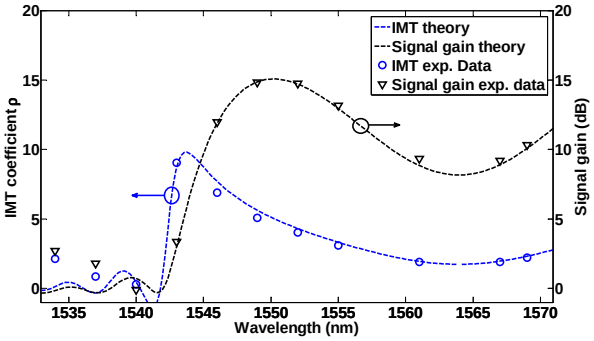

Figure 3.6: Measured wavelength dependence of signal gain (black triangles, right axis) and IMT coefficient at a modulation frequency of 1 GHz (blue circles, left axis). The solid black line shows the calculated gain and the blue dashed line the theoretical IMT coefficient for low modulation frequencies as described in Sect. 3.3.1.

addition, stronger deviations of both the theoretical gain and the IMT are observed at the edge of the gain bandwidth. This deviation is attributed to the variations of the zero-dispersion wavelength along the fiber, which are not taken into account in our model. The IMT coefficient varies from 9 to 2 over the FOPA gain spectrum and at the maximum gain region a significant IMT is obtained. The signal modulation index is 5 times the pump modulation index.
The dependence of the IMT coefficient on the modulation frequency is also considered and it is presented in Fig. 3.7. In particular, Fig. 3.7(a) shows

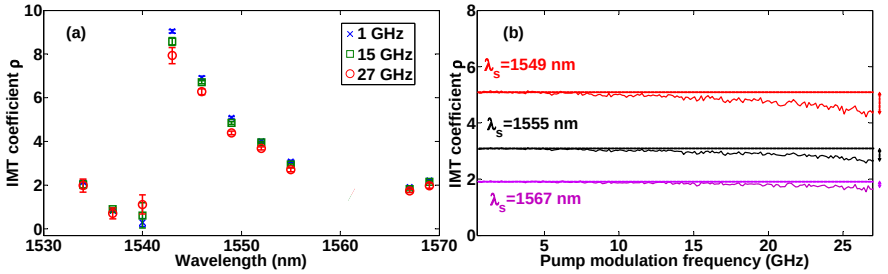

Figure 3.7: (a) IMT coefficient as a function of the signal wavelength for different pump intensity modulation frequencies. (b) IMT coefficient as a function of the pump intensity modulation frequency at different signal wavelengths. The lines are used as guidelines for the reader.

how the IMT coefficient changes for three different modulation frequencies. The error bars show the uncertainty on the averaged values obtained from averaging 20 measurements over a bandwidth of 500 MHz around the indicated modulation frequencies. It can be seen that the modulation transfer is reduced for higher modulation frequencies. This effect is larger for signal wavelengths that are detuned farther from the pump. This effect can also be observed in Fig. 3.7(b), where the IMT coefficient is shown as a function of the modulation frequency of the pump up to 27 GHz for different signal wavelengths. It can be seen from the figure that the modulation transfer starts to decrease with increasing modulation frequency. This is mainly due to the limited Mach-Zehnder bandwidth (28 GHz). However, it is worth noticing that this effect is signal wavelength dependent and is more pronounced for the signal wavelengths with the largest detuning from the pump (1549 nm and 1555 nm). Since the power at the input of the photodiode was kept small and constant, any effect due to the photodiode response and to the network analyzer can be excluded. It is believed that this could be due to a really weak averaging of the noise for high frequencies induced by the walk-off between the signal and the pump due to group-velocity mismatch.

3.4 Saturated FOPA

In the previous sections, small signal powers with respect to the pump power at the input of the FOPA were considered. FOPAs operating in the unsaturated regime are interesting for optical communications, since linear amplification is usually desired. However, for some applications such as optical signal regeneration and wavelength conversion, FOPAs operating in the saturated regime are preferable, since a high conversion efficiency is reached for strong pump depletion [28]. In Chapter 2, the coupled amplitude equations describing the amplitude evolution of the pump, signal and idler along the fiber have been introduced. They are general equations valid for FOPAs operating both in linear and saturated regimes. However, the analytical solutions proposed for the signal output power and gain (see Eqs. (2.31) and (2.34) in Chap. 2) are not valid if the assumption of undepleted pump ($P_p \gg P_s$) is not fulfilled. In this case, the parametric gain is not independent from the input signal power anymore and the coupled equations are normally solved numerically. Semi-analytical approximated solutions have also been proposed both in single-pump [90] and double-

pump [91] configurations for parametric amplification with depleted pump. The effects of pump depletion on the parametric gain and noise perfor-

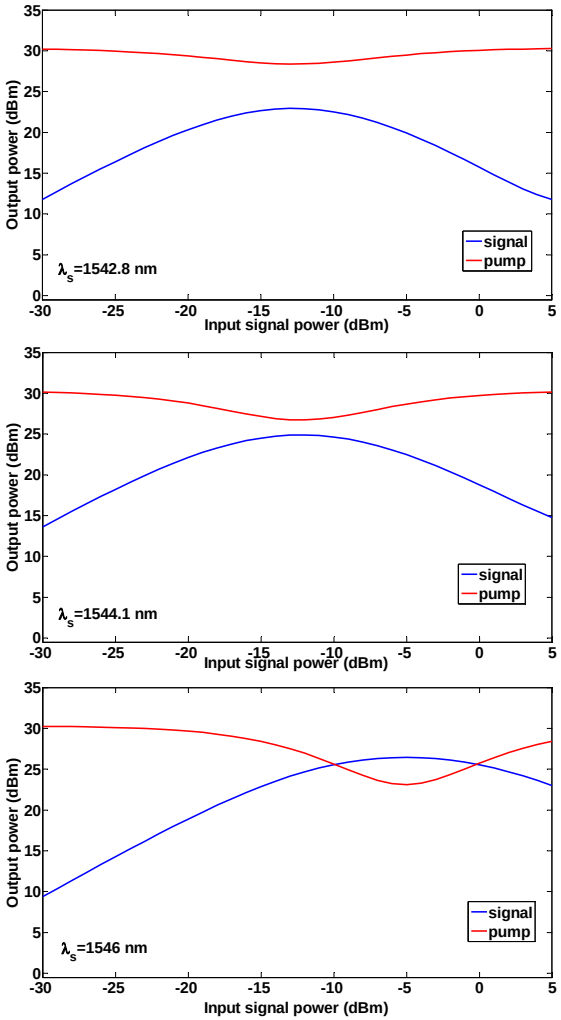

Figure 3.8: Signal and pump powers at the output of a single-pump PI-FOPA as a function of the input signal power for λ_s = 1542.8, 1544.1 and 1546 nm. Simulation parameters taken from [51].

mances of the FOPAs have been investigated in several works [51, 84]. Figure 3.8 shows the behavior of pump and signal powers at the output of the FOPA as a function of the input signal power for three different wavelengths. The simulation parameters are taken from [51]. It is seen

that for small input signal powers, the output power of the pump is almost constant and the signal output power grows linearly with the input power. In this range of signal input powers, the FOPA is working in undepleted or linear regime. A further increase in the signal input power results in a decrease of the output pump power and in the saturation of the gain, i.e. the output signal power is not linear anymore with respect to the input power. At a certain input power level, the signal output power reaches its maximum value whereas the pump output power reaches its minimum. For higher signal input powers, the pump output power begins to grow again. This is due to the fact that for high signal input levels the power is not only transferred from the pump to the signal, but also from the signal to the pump.
Furthermore, the output powers behavior depends on the signal wavelength. The bigger the separation between the signal and pump wavelengths is, the lower the signal input power is required in order for the gain to saturate. The wavelength dependence of gain saturation is also shown in Fig. 3.9(a),

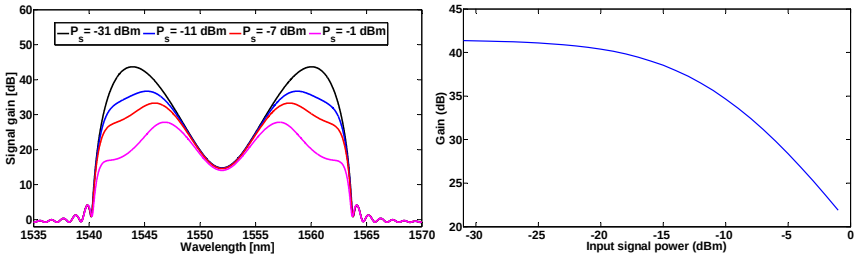

Figure 3.9: (a) Signal gain spectra for four different input signal powers. (b) Signal gain as a function of the input signal power.

where the gain spectra as a function of the signal wavelength is plotted for four different signal power levels. The gain saturation is symmetric with respect to the pump wavelength and is stronger for the signal wavelengths farther detuned from the pump wavelength. The gain dependence on the input power is shown in Fig. 3.9(b) for a signal wavelength of 1544.1 nm, corresponding to the maximum gain wavelength. The gain is constant for small-signal powers and starts to decrease for input signal powers above a certain value for which the output power is not proportional anymore to the signal input power. Thus, for FOPAs operating in the saturated regime the gain decreases, but, as previously mentioned, saturated FOPAs work as power level equalizers. This reduction is understood by considering

that, in the saturation regime, the higher signal power levels are clamped at the FOPA output, while the lower signal levels are amplified, producing a compression of the power fluctuations in the amplified signal waveform. This is shown schematically in Fig. 3.10, where two signal waveforms with different modulation indices are shown. The waveforms maximum power

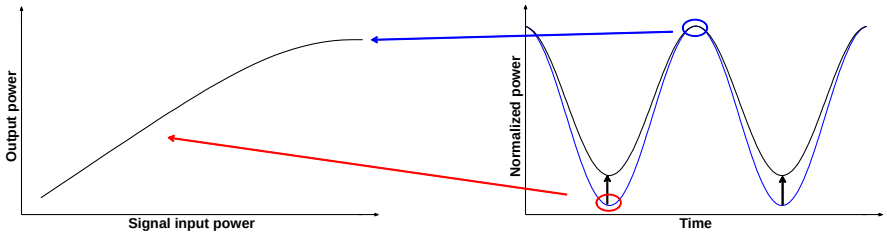

Figure 3.10: Output power as a function of the input signal power and signal waveforms for two different values of modulation index. The arrow indicates the operating regime for each signal power levels.

values are clamped, since the amplifier is saturated, whereas the minimum power values are increased, since the amplifier works in the undepleted regime. This compression effect can lead to reduction or suppression of the pump-to-signal IMT. This has been experimentally demonstrated in [92] and the experimental data are compared with numerical results. The numerical data, provided by Zohreh Lali-Dastjerdi [85], are obtained by solving the nonlinear Schrödinger equation [8] with a split step Fourier method (SSFM). The choice of employing the SSFM is due to the fact that in the saturated regime the higher order idlers become relevant and the coupled amplitude equations do not account for them. The difference between the two methods is shown in Fig. 3.11, where each of them is compared with the corresponding gain for the unsaturated FOPA [93]. In the unsaturated regime, the solutions for the gain spectrum provided by the two models are equivalent. But as soon as the FOPA is operating in saturation regime, the three coupled equations provide only an approximated result because it is not accurate enough to consider only the interactions between the pump, the signal and the first idler. The experiment is discussed in the following section.

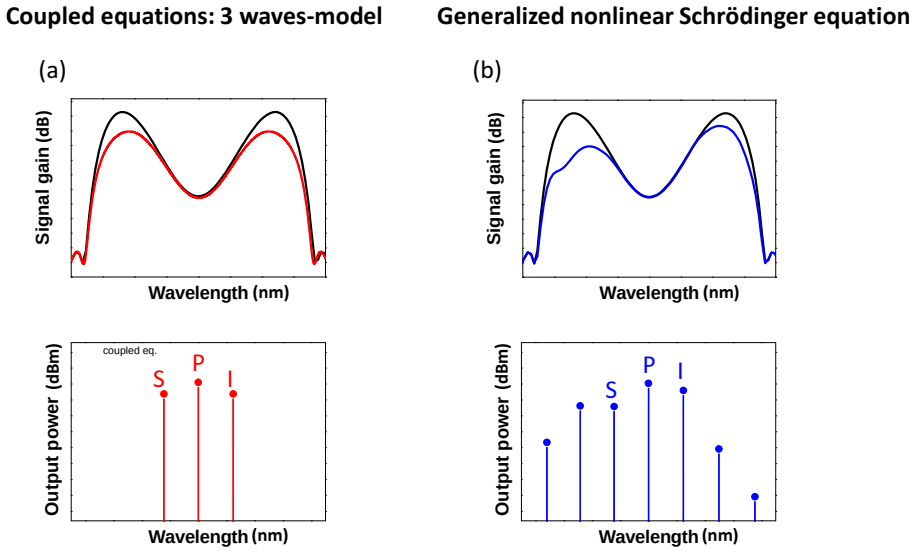

Figure 3.11: Top: Simulated gain spectra in the saturated and unsaturated regimes obtained by solving (a) the coupled amplitude equation and (b) the nonlinear Shrödinger equation using a SSFM. Bottom: Corresponding output power spectra in the saturated regime. Simulation parameters from [93].

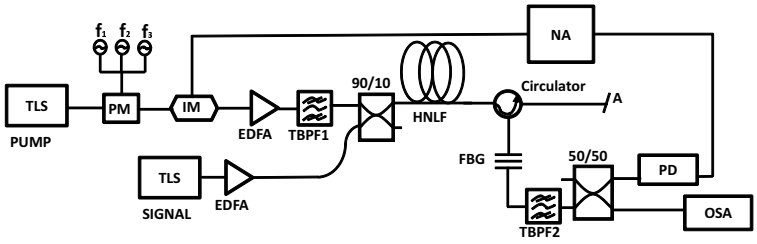

Figure 3.12: Experimental setup of the FOPA for pump-to-signal IMT characterization in pump depletion.

3.5 Experimental Investigation of Saturation Effects on IMT

The experimental setup is shown in Fig. 3.12. It is similar to the setup in Fig. 3.4 with the only difference of an EDFA placed after the signal TLS to be able to saturate the FOPA using different input power levels. As in the previous experiment, the modulation indices are measured with a network

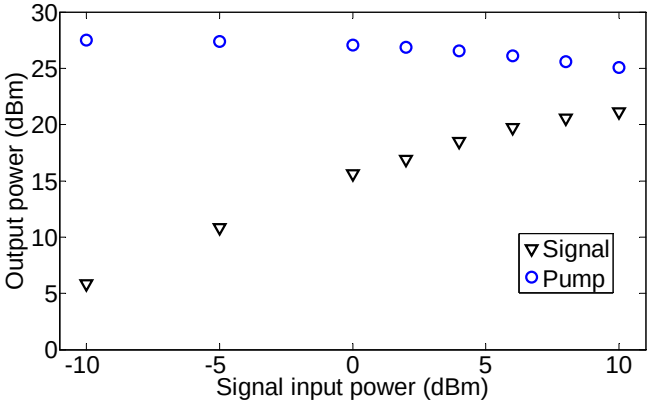

Figure 3.13: Pump and signal output power as a function of signal input power measured at the maximum gain wavelength ($\lambda_s = 1550$ nm).

analyzer after detection by a photodiode.
In the experiment, measurements on the noise spectral density P_{noise} in units of [dBm/nm] were also performed to investigate the total noise performance of the saturated FOPA. This is due to the already mentioned strong dependence of the noise on the input signal power in FOPAs. The noise spectral density includes all the four main contributions: the amplified spontaneous emission, including the pump residual noise and the amplified quantum noise, the Raman seeded spontaneous emission and the pump fluctuations transferred to the signal [86]. Moreover, it also includes the amplified spontaneous emission introduced by the EDFA amplifying the signal at the input of the FOPA. The measurements related to P_{noise} at the FOPA output are obtained by means of an optical spectrum analyzer (OSA) connected directly to the output of the DSF-HNLF. The noise spectral density was measured with an interpolation technique at the ± 1 nm offset interpolation wavelengths. At the maximum gain wavelength ($\lambda_s = 1550$ nm), the output power is measured for both pump and signal as a function of the signal input power. The results are shown in Fig. 3.13. As expected [51], when the signal input power is increased, the pump output power starts to decrease, and the signal output power saturates.

Due to the wavelength dependence of both IMT and gain saturation [51, 81], a characterization over the entire gain bandwidth is necessary. In particular, the gain as a function of the signal wavelength for different signal input power levels is shown in Fig. 3.14(a), along with results of numerical simulations. All the simulated data are obtained using the SSFM. The fig-

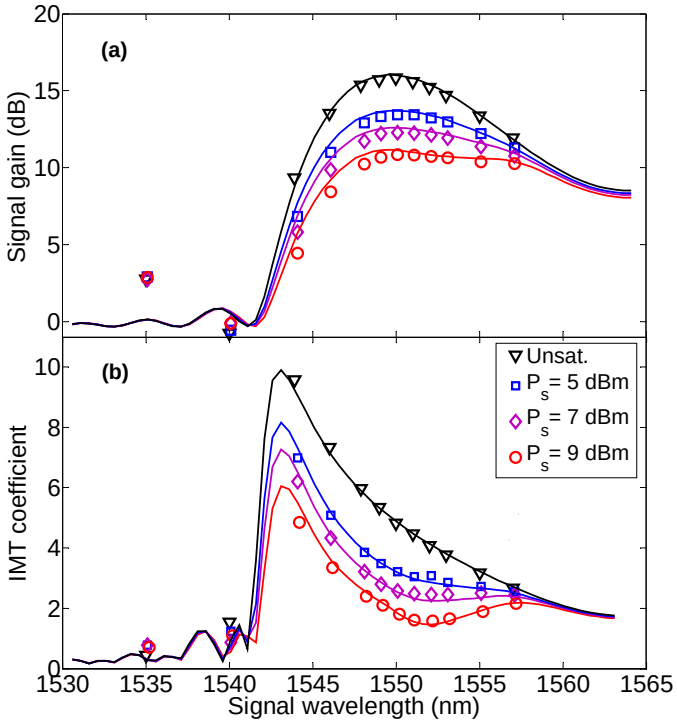

Figure 3.14: (a) Wavelength dependence of the signal gain for different signal power levels. (b) IMT coefficient ρ as a function of signal wavelength for different signal power levels for 10 GHz RF modulation frequency. The marks are the measured data and the lines are the numerical simulation results.

ure shows a decrease of the amplifier gain as the signal power is increased from -10 dBm (unsaturated regime) up to 9 dBm, confirming the gain saturation predicted from the decreasing output power in Fig. 3.13. The saturation effect is notable already for 5 dBm signal power and it becomes stronger when the input signal power increases up to 9 dBm, at which point the maximum gain has decreased from the unsaturated value of 15.8 dB to 11 dB. The flattening effect on the gain spectrum due to saturation is also noticed in the figure. The corresponding IMT coefficients are shown in Fig. 3.14(b). As expected from the theory [81], the IMT coefficient increases with increasing wavelength separation between the signal and the pump, and the transfer is significant (i.e. the modulation index of the signal is almost 5 times the modulation index of the pump in the undepleted regime) at the peak gain wavelength. One important observation from the

experimental data is that the IMT coefficient decreases when the signal input power increases and the gain saturates. Consequently the amount of fluctuations transferred to the amplified signal due to pump power fluctuations is significantly reduced. A good agreement is found between the measurements and the simulations. The good agreement validates our numerical model and hence allows us to predict gain and IMT at other pump power levels, as it is shown in the following subsection.

The usual operation region of single-pump FOPAs is around the wave-

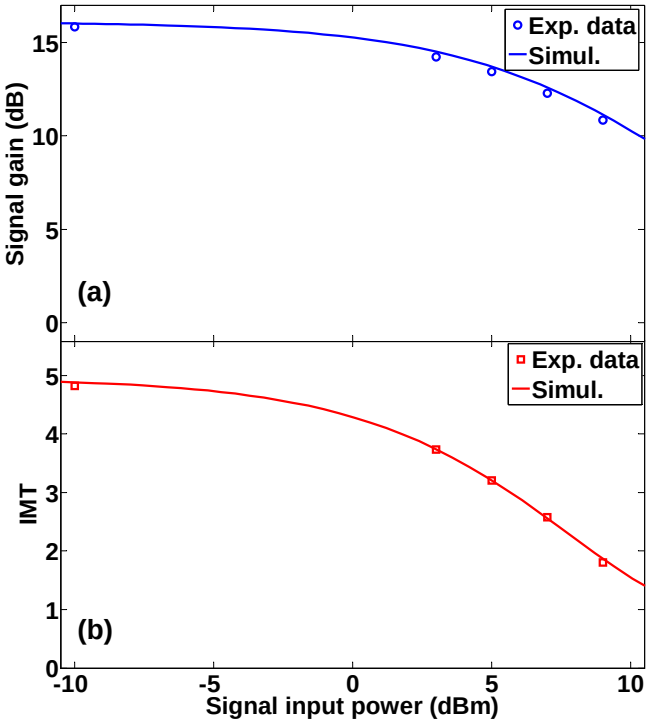

Figure 3.15: (a) Measured signal gain and (b) measured IMT coefficient as a function of the input signal power at the maximum gain ($\lambda_s = 1550$ nm). The RF modulation frequency is 10 GHz. The continuous line are the simulated data using the SSFM.

lengths of maximum gain, where the maximum efficiencies in terms of energy conversion from the pump to the signal and idler are obtained. Therefore, the gain and IMT as a function of signal input power are studied in more details at the gain peak (1550 nm) and the results are shown in Fig. 3.15(a) and (b), respectively. The IMT coefficient around the

maximum gain wavelength is reduced by almost a factor 3, from 4.85 to 1.80, when the signal power is increased from the unsaturated regime to $P_s = 9$ dBm, i.e. the FOPA is 5 dB in depletion. Moreover, it is important to notice that the IMT is reduced below a factor 2 at (1550 nm), while the amplifier gain still remains above 10 dB. Consequently, it is possible to obtain an amplifier with a significantly lower noise contribution due to the intensity modulation transfer between the pump and the signal when the FOPA is operating in depletion as compared to undepletion. However, there are two main issues when operating in the saturation regime: reduced gain and increased noise spectral density.

Gain Reduction

The pump depletion results in a gain reduction, especially at the gain peak, creating the necessity to find a compromise between the reduction of the gain and that of the IMT. However, it should also be taken into account that the gain in parametric amplifiers depends on many factors through which it is possible to optimize the signal gain, for example the pump power or the fiber parameters. Thus it is possible to control the trade off between IMT and signal gain reduction. In fact, considering that higher pump powers provide higher gain, hence stronger saturation with increasing signal input power, it is expected that the saturation effect on the IMT will be stronger when increasing the pump power. To investigate this, a pump power level for which the 3 dB reduction of the saturated gain is equal to 16 dB was considered, i.e. the non-saturated gain of the amplifier with pump power of 27.5 dBm which had been studied experimentally. This can be obtained for a pump power of $P_p = 28.1$ dBm and a signal input power of 4 dBm, as seen in the simulated gain curves of Fig. 3.16. To investigate the trade off between gain and IMT reduction, a set of numerical calculations of the gain and the IMT as a function of the wavelength was performed for these two values of pump power, fixing the signal input power at two different levels as well, $P_s = -30$ dBm and $P_s = 4$ dBm, in order for the amplifier to operate in the unsaturated and saturated regime, respectively. The results for the gain and the IMT coefficient are shown in Fig. 3.17(a) and (b), respectively. As expected, the increase of the pump power level produces a higher reduction of both the gain and the IMT coefficient, due to higher pump depletion. This is shown in Fig. 3.17(a) and (b), respectively. In particular, Fig. 3.17(b) shows that for a pump power level of 28.1 dBm, the IMT coefficient is decreased down to 3, which is a value lower than the

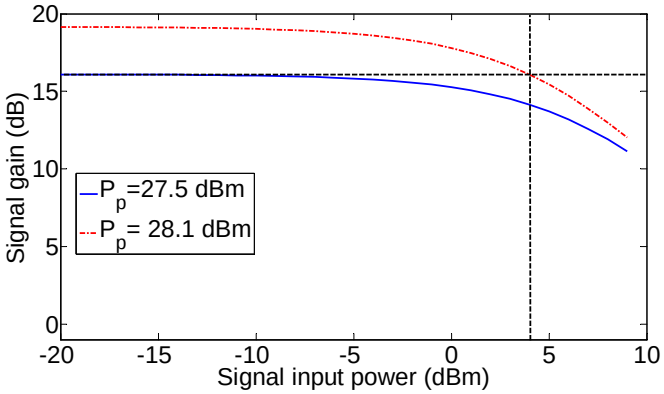

Figure 3.16: Calculated signal gain as a function of the input signal power at $\lambda_s = 1550$ nm for two different pump power levels ($P_p = 27.5$ dBm, 28.1 dBm).

one calculated for a pump power of 27.5 dBm. The improvement is also seen considering the measured data in Fig. 3.14(b). In fact, it is noticed that the IMT coefficient for a pump power of 27.5 dBm and a signal power of 5 dBm is higher than 3, showing that it is possible to obtain a lower IMT coefficient with a lower signal input power, by adjusting the pump power by about 0.6 dB.

Noise Spectral Density

The second issue related to the employment of a saturated FOPA is that the noise performance of the amplifier, i.e. the amplified quantum noise, the residual pump noise, the Raman seeded spontaneous emission, the transferred IMT and the spontaneous emission added to the signal by the EDFA before the FOPA, worsens when the signal input power increases [87]. To characterize this, the noise spectral density P_{noise} has been measured both as a function of the signal wavelength over the entire signal gain bandwidth and as as a function of the signal input power at the wavelength of the gain peak. The measurements are performed for an OSNR of the pump at the input of approximately 50 dB and an OSNR of the signal ranging from 56.2 dB at maximum signal input power to 55.5 dB at minimum signal input power. The results are shown in Fig. 3.18(a) and (b), respectively. The measurements confirm that the noise spectral density in the amplifier increases strongly with the signal input power, reaching values of up to

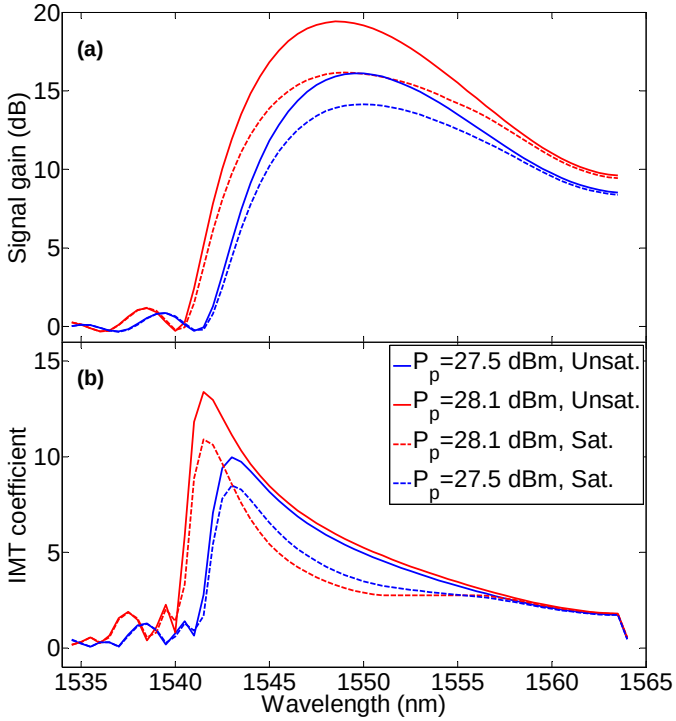

Figure 3.17: (a) Calculated signal gain and (b) calculated IMT coefficient as a function of wavelength for two different pump power levels (P_p = 27.5 dBm, 28.1 dBm), in both cases of unsaturated and saturated amplifier operation. The RF modulation frequency is 10 GHz.

−14 dBm/nm for a high pump depletion at a signal input power level of 9 dBm. A saturation of the noise spectral density is seen in Fig. 3.18(b) for increasing signal input power, which is due to the saturating gain. In summary, it has been shown that the IMT decreases in saturated FOPAs, making operation in saturation attractive for applications for which the intensity fluctuations of the signal constitute a limitation of the performances [32]. However, the operation in pump depletion results in increased noise spectral density and such increase may limit the potential benefit coming from the saturation effect. As a consequence, even if the saturation-induced gain reduction may not be a major limitation for some optical signal processing applications for which a high gain is not necessary, the increase in the amplifier spectral noise density may be a fundamental constraint.

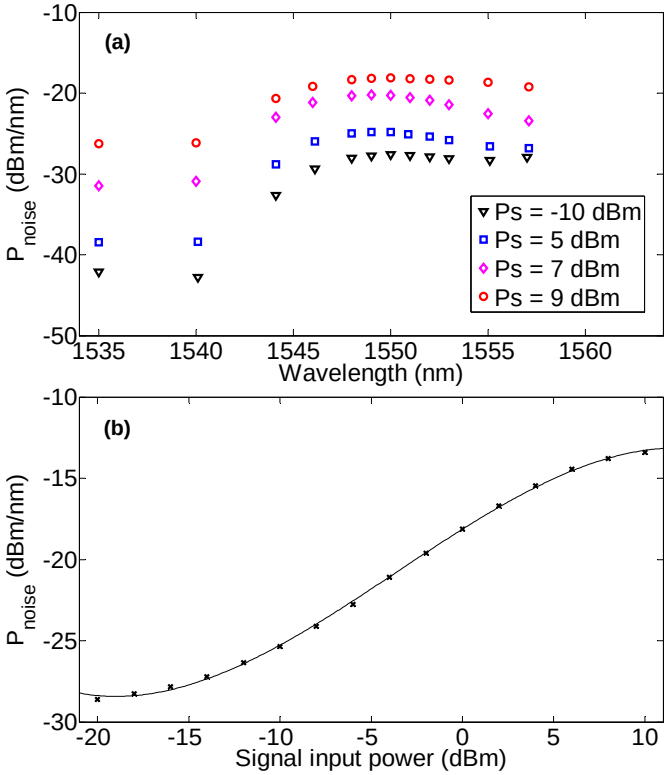

Figure 3.18: (a) Measured noise spectral density as a function of the signal wavelength for different signal power levels and (b) noise spectral density as a function of the input signal power at the maximum gain wavelength ($\lambda_s = 1550$ nm).

3.6 Summary

In this chapter, an overview of the noise figure and the pump-to-signal intensity modulation transfer (IMT) in FOPAs has been provided. The analytical model for low-frequency IMT introduced in [81] was briefly described. This model was used to compare the experimental results obtained by measuring the IMT for modulation frequencies up to 27 GHz in unsaturated FOPAs. The results show a good agreement between the analytical model and the measurements. FOPAs operating in saturation regime were also covered. Furthermore, the IMT from the pump to the signal in saturated FOPAs has been experimentally investigated and a good agreement

between simulations and measurements has been demonstrated. It has been shown that the saturation effect produces a reduction of the IMT coefficient. In the particular FOPA considered in this work, the IMT is reduced below 2, thereby resulting in amplifiers with a significantly lower noise contribution from pump power fluctuations transferred to the signal. The gain is also reduced as a consequence of pump depletion. Nevertheless, it has been shown that a compromise between gain and IMT reduction could be achieved by adjusting, for example, the pump power to a higher level to obtain the same gain with a lower IMT coefficient. However, an investigation on the noise spectral density has shown that, in saturation, the other noise contributions of the amplifier, i.e. amplified spontaneous emission, Raman seeded spontaneous emission and amplified spontaneous emission of the signal EDFA, cannot be neglected. In fact, even though the IMT decreases with increasing signal input power, the noise spectral density of the amplifier increases, which may limit the benefit due to the IMT reduction on the performance of FOPAs.

Chapter 4

Short-Pulse Generation in an All-Fiber Laser Source

4.1 Introduction

In order to proceed with the characterization and amplification of short pulses in fiber optical parametric amplifiers (FOPAs) covered in Chapter 5, a laser source emitting short pulses is needed. The source has to fulfil two mains requirements: it has to emit pulses in the 1.5μm wavelengths region and the laser output needs to be fiber coupled in order to realize an all-fiber optical system. This is due to the fact that all-fiber systems are convenient because of their compactness, reliability and long-term stability. To meet the requirements, an erbium-doped fiber (EDF) laser is built and, among all the configurations, the so-called figure-of-eight laser (F8L) configuration is chosen because of the capability of producing short soliton pulses by means of passive mode-locking. A brief theoretical introduction to mode-locking mechanisms and F8L is provided in Secs. 4.2 and 4.3, respectively. The experimental realization of the laser is covered in Sec. 4.4, describing the two main configurations obtained and their limitations.

4.2 Mode-Locking and Q-Switched mode-locking in Fast Saturable Absorbers

A pulsed laser is composed of three basic elements: the cavity or resonator, which forces the light to pass over the same path again and again; the gain medium, which coherently amplifies the light passing through it; and a modulator, which modulates the cavity loss. To start the laser radiation at one or more frequencies corresponding to the cavity modes frequencies, the gain medium needs to be pumped by an external source, such as a pump diode. This initial CW radiation is amplified at every passage in the gain medium building up an intense beam, which is shortened again and again at every round trip in the cavity by the modulator acting as a shutter [94]. When talking about laser dynamics, it is important to distinguish between small-signal gain and saturated gain. In fact, for weak spontaneous emission in the gain medium to build up and produce a significant laser intensity, the gain has to exceed the cavity loss, but to reach steady-state operation it should be equal to the cavity loss. This is obtained by saturation of the gain, which happens as the laser intensity reaches a threshold defined by the gain medium [94].
It is possible to distinguish between two operational modalities of a laser, depending if one or several cavity longitudinal modes are excited: single mode operation and multimode operation. However, only the multimode operation allows to obtain broad bandwidth. To achieve multimode operation instead of single-mode operation, the gain should slightly exceed the loss for several cavity modes frequencies at the beginning, i.e. before the pulses start to form. The two cases are shown in Fig. 4.1. In Fig. 4.1(a) the single mode operation is depicted. For single mode operation, the small-signal gain should exceed the loss only for a single frequency, i.e. only one cavity mode should be excited, and to obtain this a frequency-dependent loss element (a filter) is inserted in the cavity. The saturated gain is also plotted in Fig. 4.1(a), showing that after the excitation of the mode, the gain should saturate and equal the loss in order to reach steady-state operation. In Fig. 4.1(b), instead, the multimode operation is depicted. In this case, the gain should exceed the loss for several frequencies and all the modes, for which the gain lies above the loss, are excited. Steady-state operation is again reached through saturation of the gain. When several modes are excited, each of them will oscillate independently, with no fixed relationship between each other, in practice like a set of independent lasers all emitting light at slightly different frequencies. The individual phase of

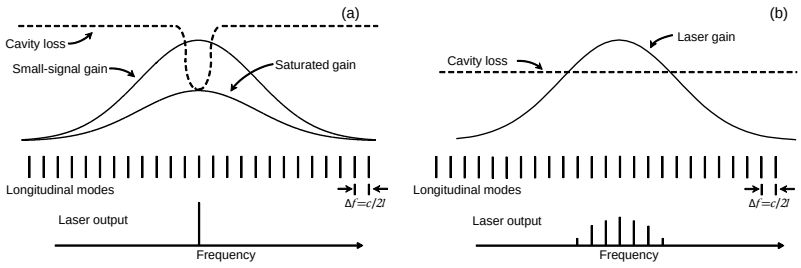

Figure 4.1: Laser gain and cavity loss spectra, longitudinal modes location and laser output for (a) single-mode laser operation and (b) multimode laser operation.

the light waves in each mode is not fixed and the intensity at the output of the laser fluctuates randomly about an average value, i.e. continuous wave (CW) operation is obtained. In order to generate pulses, each mode need to operate with a fixed phase between it and the other modes and this can be achieved by modulating the intra-cavity light through modulation of the cavity loss. The process by which the modes are held with fixed relative phases is known as *mode-locking*.

The modulation of the cavity loss plays a key role in initiating and maintaining mode-locked laser operation, which can be divided into two categories: active mode-locking, i.e. the modulation is provided by an amplitude modulator externally driven, and passive mode-locking, where the laser radiation forms its own modulation through saturable absorbers [95]. The discussion in this work is focused on passive mode-locking.

The important processes involved in passive mode-locking are the saturation dynamics of the gain element, the group-velocity dispersion (GVD), the self-phase modulation (SPM) and the cavity loss, which can be divided into linear loss (the portion of loss independent from the laser power) and intensity-dependent loss also called saturable loss, which changes dynamically in response of the light intensity. This dynamic change of the cavity loss can be obtained by either inserting a real saturable absorbing medium into the cavity, such as semiconductor saturable absorber mirrors [96], or by exploiting the Kerr effect (i.e. implementing an artificial absorber). In the second case, one can talk of *fast saturable absorber*, since the response time of the saturable absorbing element (on the order of few fs) is comparable with the optical cycle. In fast saturable absorber, the cavity loss is

modulated through a combined effect of dispersion and SPM. In particular, due to the modulation instability (MI) in the anomalous dispersion regime (see Subsec. 2.4.3 in Chap. 2), the combined effect of dispersion and SPM in the cavity leads to a self-induced amplitude modulation of the laser radiation (know as self-amplitude modulation (SAM)) [97]. Since the SPM and, then, the SAM are intensity-dependent [8], the higher power levels of the modulated light are enhanced at every passage through the nonlinear medium whereas the lower power levels are attenuated. As a consequence, the laser radiation is shortened and short pulses are generated.
The dynamics of the loss and gain in an artificial fast saturable absorber are schematically shown in Fig. 4.2. The linear loss is indicated with l_0, while

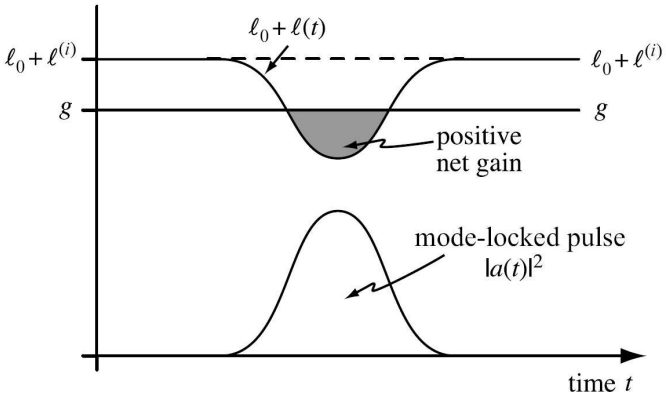

Figure 4.2: Gain and loss dynamics in artificial fast saturable absorber mode-locking. From [94].

the intensity-dependent loss is represented by $l(t)$, for which its small signal value is $l^{(i)}$. The saturated gain g can be consider constant on the pulse-duration time scale, due to the fast response of the saturable absorber. g depends on the small-signal gain g_0 and the gain saturation power P_G and is expressed as

$$g = \frac{g_0}{1 + \langle P \rangle / P_G}, \tag{4.1}$$

where $\langle P \rangle$ is the laser average power. g is intensity dependent as the loss, but on a longer time scale of several pulses and for that it can be considered constant. Before the pulse the loss exceeds the gain, as shown in Fig. 4.2. As the pulse arrives, the total loss starts to decrease from the small-signal value $l_0 + l^i$, due to its dependence on the pulse intensity. Later in the pulse, the gain overcomes the loss and at the center the pulse experiences a

positive net gain, as shown in Fig. 4.2 by the shaded region. After the peak of the pulse, its intensity becomes smaller in the trailing edge and, thus, the saturation of the loss becomes also smaller and the loss increases again. After the pulse, the loss exceeds the gain as before its passage through the saturable element. Therefore, the absorber suppress the leading and trailing edge of the pulse, since the net gain is negative in these regions, while it passes or amplifies, depending if the gain equals or exceeds the loss, the center of the pulse. This has the effect of shortening the pulses until a steady state operation is reached.

Mode-locking is self-sustaining, but not always self-starting. With self-sustaining is meant that, once the mode-locking is initiated, it remains stable until the laser is disturbed. While with self-starting is meant that the laser can mode-lock spontaneously once the pump power is applied. In mode-locked lasers using ultrafast Kerr effect, such as the F8L, the mode-locking is usually not self-starting, but it requires external perturbation to start. This can be explained by using the concept of pulse-shortening velocity, which is defined as the fractional change in pulse duration in a single pass through the pulse shortening element in the laser [98]. The pulse shortening velocity in passive mode-locked laser using fast saturable absorber is strongly pulse width dependent, since the term responsible for pulse shortening (i.e. the term responsible for SAM) is proportional to the peak power and, consequently, to the inverse of the pulse width [94]. As a consequence, the nanosecond time scale intensity fluctuations present in CW operation of an unlocked multimode laser can be more than five orders of magnitude slower than the pulse-shortening velocity for mode-locked operation in the femtosecond regime. The mode-locking of a F8L, therefore, requires small external perturbations, which can be created by mechanical perturbations, by changing the cavity length or by synchronous pumping with pulses from an external actively mode-locked laser.

The F8L can work in two different mode-locked stable regimes: CW mode-locking and Q-switched mode-locking. The term CW mode-locked is often used to distinguish between mode-locked lasers emitting pulses with constant pulse energy and Q-switched mode-locked lasers. Q-switched mode-locking refers to the regime, where the intracavity pulse energy undergoes large oscillations, related to a dynamic instability and this produces a modulation of the mode-locked pulses envelope. The origin of Q-switching instabilities is that the saturable absorber favors pulses with higher energies, which, thus, experience lower resonator losses. As a consequence, the pulses are amplified at different level since they are not subject to the same value

of the net gain. The Q-switching instabilities can be reduced by changing the gain saturation dynamics of the cavity to stabilize the pulse energy. This has been done in the experimental implementation of the F8L when a first configuration was emitting Q-switched mode-locked pulses. This is discussed later on in this chapter, after that the F8L configuration and working principle are introduced in the following section.

4.3 Figure-of-Eight Laser

The F8L was first introduced by I. N. Duling III in 1991 [27]. He presented a two rings laser cavity, shaped as an eight, where short pulses could be generated by passive mode-locking [94]. A schematic layout of the F8L is shown in Fig. 4.3. The laser consists of two fiber loops connected by a 2x2

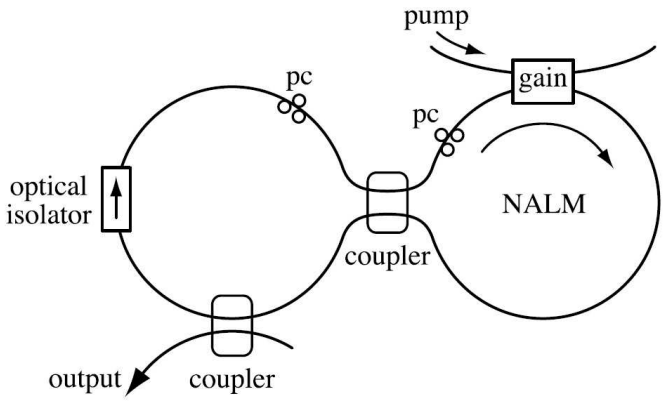

Figure 4.3: Typical layout for a figure-eight laser. PC: polarization controller. From [94]

coupler. The right loop is termed nonlinear amplifying loop mirror (NALM) and is responsible for both the laser gain and for the modulation of the cavity losses, which is necessary for mode-locking. The gain element is typically an erbium-doped fiber amplifier (EDFA), which is pumped at 980 or at 1480 nm and provides gain in the 1.5 μm wavelength region. The left loop is simply a feedback element, which contains an optical isolator to enforce unidirectional operation and takes the output of the NALM and connects it back to the NALM input. In the feedback loop an output

coupler is also present to extract the pulses. Polarization controllers (PCs) are used to bias the polarization of the circulating light appropriately with respect to the small birefringence of the fibers. The NALM is discussed in detail in the following subsection.

4.3.1 Nonlinear amplifying loop mirror

The working principle of a NALM is based on the phase shift accumulated in nonlinear media, such as fibers, due to the dependence of the phase on the propagating field intensity as discussed in Chapter 2. A schematic of the NALM is shown in Fig. 4.4. The gain medium, as mentioned, is an EDF

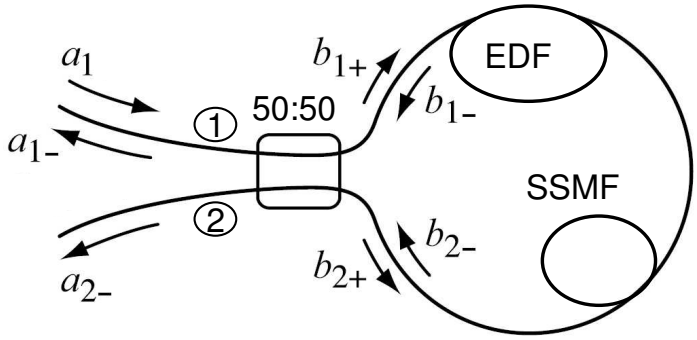

Figure 4.4: Nonlinear amplifying loop mirror geometry using an EDF as gain medium and a balanced coupler (50 : 50). SSMF: standard single mode fiber.

pumped at 980 or at 1480 nm. The nonlinear medium necessary to create the phase shift is typically a SSMF, or in some configurations a highly nonlinear fiber (HNLF) or a dispersion shifted fiber (DSF). A balanced coupler is commonly used to connect the NALM to the feedback loop. Considering the unidirectional operation due to the isolator in the feedback loop, an input field is always incident only at the port 1 of the 50 : 50 coupler. The input field, indicated by the complex amplitude a_1, is split by the coupler

in two counterpropagating components in the loop mirror (b_{1+} and b_{2+}). The clock-wise propagating wave b_{1+} is first amplified by the EDFA and, then, propagates through the fiber, accumulating a nonlinear phase shift ϕ_{12}. The counter clock-wise wave b_{2+}, instead, first propagates through the fiber and then is amplified, accumulating a smaller nonlinear phase shift ϕ_{21} ($\phi_{12} > \phi_{21}$). b_{2-} and b_{1-} corresponds, respectively, to b_{1+} and b_{2+} after the amplification and the propagation in the NALM. If the difference in nonlinear phase shifts $\Delta\phi = \phi_{12} - \phi_{21}$ is π, then the two components interferes in such a way at the coupler that all the light is sent towards the lower arm of the 50 : 50 coupler (port 2) [99, 100]. Anyway, the residual light (a_{1-}) sent in the other direction is eliminated by the isolator. The round-trip gain is very small for low powers, but much larger for high powers, such as the peak power of the pulses. This effect favors the peak of a circulating pulse against the low-power background light, amplifying the central part of the pulse and attenuating the leading and trailing edges of the pulses. The initial laser radiation in the range 1530-1570 nm, due to the pumping of the EDFA, is shorten at every passage through the NALM, until a steady-state operational mode is reached when the peak power of the circulating pulses reaches the fundamental soliton power [8, 94]. It is worth noticing that the key point for the NALM is that the gain element is placed very close to one of the ends of the loop in order to create an unbalanced propagation between the two counterpropagating waves.
The F8L experimental implementation is described in the following section.

4.4 Experimental Setups

In this section, two different F8L configurations are described. The first one provided Q-switched mode-locked pulses, but it is included to describe the process leading to the final laser emitting CW mode-locked pulses.

4.4.1 Q-Switched Mode-Locked F8L

The first F8L configuration is shown in detail in Fig. 4.5. The NALM is realized combining three different kinds of fiber. In particular, it consists of 10 m of EDF, 4.5 m of DSF and 7.5 m of SSMF. The DSF is employed to increase the nonlinear phase shift by increasing the propagation length

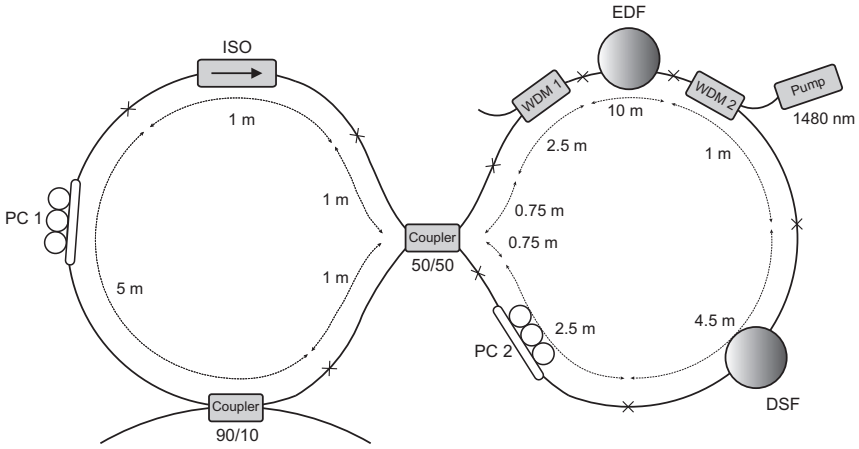

Figure 4.5: Schematic of the F8L setup working in Q-switched mode-locking regime. EDF: erbium-doped fiber; WDM: wavelength division multiplexer; SSMF: standard single mode fiber; DSF: dispersion shifted fiber; ISO: isolator; PC: polarization controller.

in the loop, but without affecting significantly the total cavity dispersion. In fact, the DSF has a dispersion parameter equal to 0.47 ps/(nm · km) at 1560 nm. The EDF has a 1529 nm absorption of 6.89 dB/m and the dispersion parameter at 1560 nm was −29.7 ps/(nm · km). The choice of such a low absorption EDF is made to keep the splicing loss between the EDF and the SSMF low at approximately 0.1 dB per splice. Usually pumping at 980 nm is preferable, even if it provides lower gain, in order to reduce the EDFA spontaneous emission and, thus, the laser intensity noise. However, due to the low absorption, in order to obtain enough gain to overcome the cavity losses, the EDF needs to be pumped with a diode at 1480 nm. The pump diode power as a function of the pump applied current is shown in Fig. 4.6. The pump diode is kept constantly at a temperature of 25 °C. In the rest of the chapter the pump current I_{ld} is considered instead of the power.The resonator is composed only of a SSMF length of 8 m and the total cavity length is approximately 30 m. For the SSMF, a dispersion parameter at 1560 nm approximately equal to 18 ps/(nm · km) is considered. Therefore, the EDF, the SSMF and the DSF have a GVD β_2 equal to 38.3, −23.3 and −0.6 ps^2/km respectively. The calculated dispersion parameter curves of the three fibers are shown in Fig. 4.7. The dispersion curves are calculated from the dispersion slope, the dispersion curvature and the zero-dispersion wavelengths (ZDW) of each fiber. The dispersion

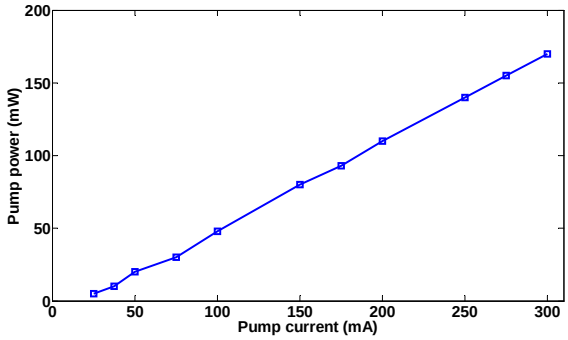

Figure 4.6: Pump power as a function of the current applied to the 1480 nm pump diode at a temperature of $T = 25$ °C.

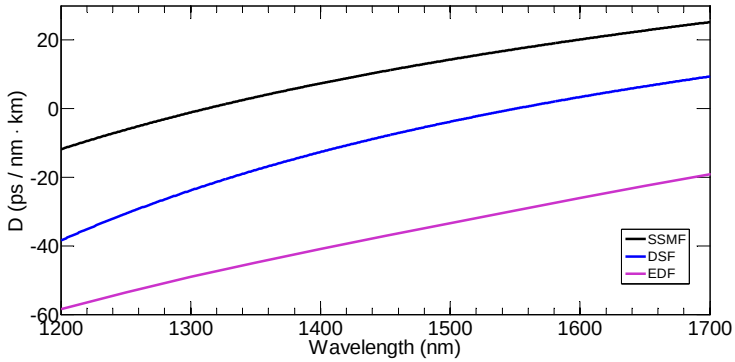

Figure 4.7: Dispersion parameter curves of the SSMF, EDF and DSF used in the laser configuration illustrated in Fig. 4.5. The curves are calculated considering the ZDW, the dispersion slope and the dispersion curvature.

slope parameter for the SSMF is obtained considering an average value for all the SSMF components in the cavity, while for the EDF the calculated dispersion is provided by OFS Fitel Denmark along with the fiber. The total cavity dispersion D_{tot} is calculated as follows

$$D_{tot} = \beta_{2SSMF} L_{SSMF} + \beta_{2EDF} L_{EDF} + \beta_{2DSF} L_{DSF} = 0.0198 \text{ps}^2, \quad (4.2)$$

and in the rest of the chapter, one refers to this quantity with the term cavity dispersion.

The total cavity dispersion is normal. For fundamental soliton propagation, the total cavity dispersion should be anomalous. However, it has been demonstrated that efficient F8L are obtained for small but positive total cavity dispersions [101–103] and also that a more efficient solitonlike propagation can be obtained in dispersion managed cavities if the cavity dispersion is slightly positive [104]. The total linear loss in the cavity is measured to be approximately 5.4 dB without considering the EDF, since the loss depends on the pumping. The EDF should provide a small-signal gain that exceeds the total loss, including the absorption and the EDF loss. To obtain that, the gain can be adjusted by tuning the pump power applied to the EDF until the mode-locking starts. The gain and the amplified spontaneous emission (ASE) spectra of the EDF pumped with different powers are shown in Fig. 4.8. The gain is measured considering as input of the EDFA a signal generated by a CW tunable laser at 1550 nm and input signal power of 0 dBm. The ASE spectra are obtained by pumping the EDF without any input signal. Two peaks can be seen at 1530 and 1560 nm. However, the total cavity dispersion calculated at 1530 nm has a higher positive value, 0.09ps^2, with respect to its value at 1560 nm. In fact, the cavity favored such wavelength and, before that a perturbation is created and the laser is mode-locked, it emits CW light at 1560 nm as it can be seen in Fig. 4.9. From Fig. 4.8(a) it is seen that a pump current between 30 and 50 mA should provide enough gain to reach a stable regime. However, to start the mode-locking a much higher pump power of approximately 250mA is required. This is due to the fact that high spontaneous emission and power fluctuations are necessary for the laser to start the mode-lock. Once the laser is mode-locked, the pump power should be decreased to the minimum value for which the mode-locking is self-sustaining. The laser should be run to the minimum power for the fundamental soliton to exist, in order to avoid higher order solitons or dispersive waves, since the pulse energy is quantized for solitons [8, 94]. The Q-switched mode-locked spectra for a pump current I_{ld} equal to 42.6 mA is shown in Fig. 4.10. It is centered around 1560 nm and the measured average power is approximately 32 μW. The inset shows a detail of the spectrum to highlight the FWHM bandwidth, which is approximately 10.4 nm. If the laser emits transform-limited soliton pulses, the time-bandwidth product (TBP) is equal to 0.315 and the estimated pulse width is 250 fs. The repetition rate, i.e. the inverse of the time necessary for the pulse to make a round in the cavity, for a 30 m-long cavity is 6.8 MHz and considering the measured average power, the estimated peak power is approximately 18.5 W. The high peak

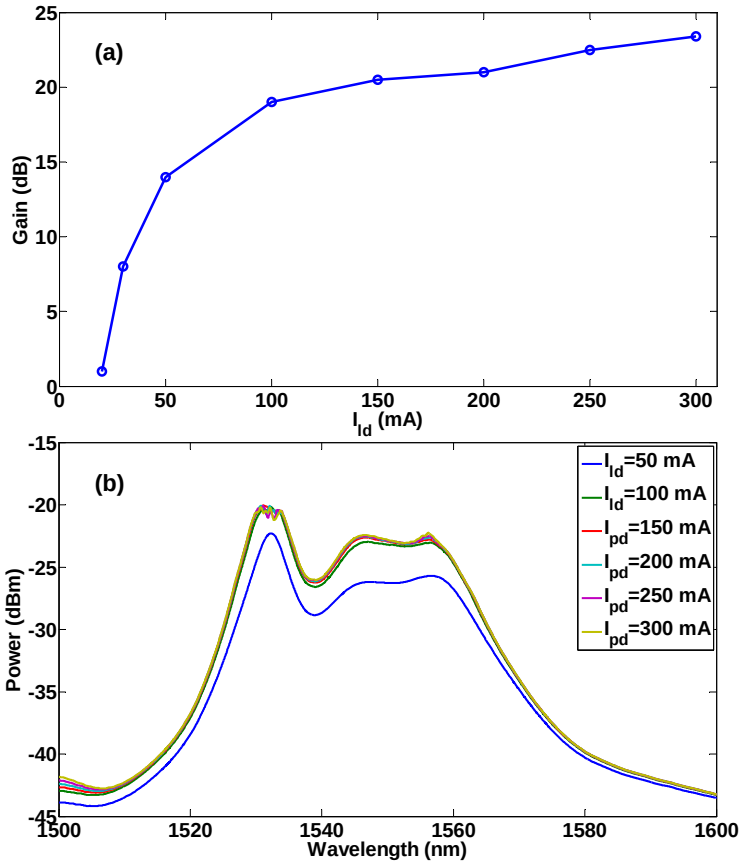

Figure 4.8: (a) EDF gain as a function of the pump power for a signal at 1550 nm and input power $P_s = 0$ dBm. (b) Amplified spontaneous emission of the EDF for different pump currents.

power for such small average power is due to the low repetition rate. The repetition rate is not only estimated, but also measured by means of an oscilloscope and the obtained train of pulses is shown in Fig. 4.11. The measured distance between two consecutive pulses is approximately 215 ps corresponding to a repetition rate of approximately 5 MHz. This difference with respect to the expected value is due to a clear modulation of the amplitude envelope, due to the fact that the laser is Q-switched mode-locked. In fact, due to the different amplitude of the pulses it is difficult to set a trigger level in the oscilloscope, allowing the detection of all the pulses in the train. Therefore, the measured repetition rate is not reliable. As

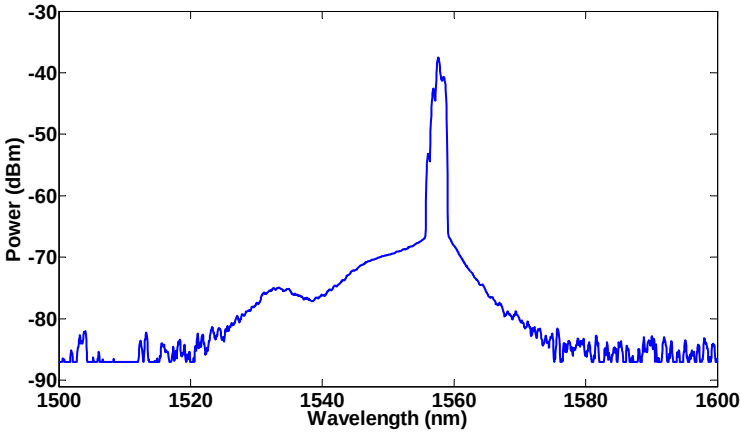

Figure 4.9: F8L emitted spectra in CW regime, i.e. before a perturbation start the mode-locking.

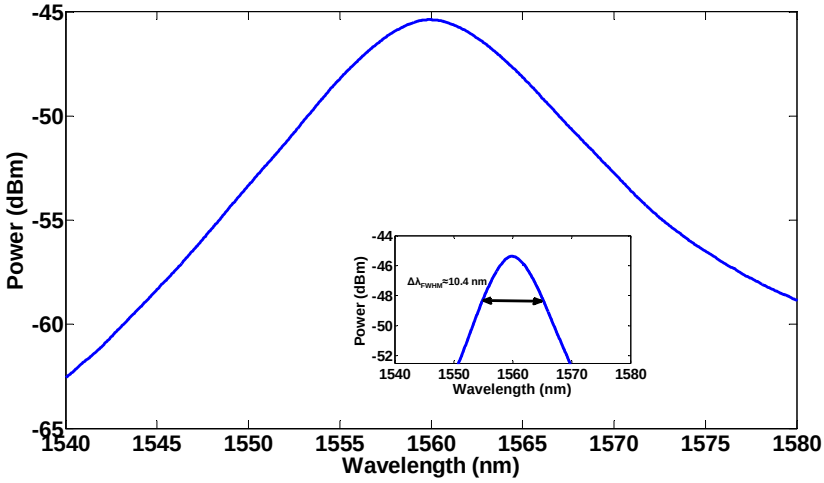

Figure 4.10: Power spectrum of the mode-locked laser for a pump current of 42.6 mA. The inset shows a detail of the spectrum to highlight the FWHM spectrum and the corresponding FWHM bandwidth is approximately 10.4 nm.

mentioned in Sec. 4.2, the Q-switching means that the absorber does not recover for each pulse and, because of this instability, the pulses experience different values of loss. Since adjusting the pump current does not improve the stability of the laser, the cavity needs to be re-designed to suppress the

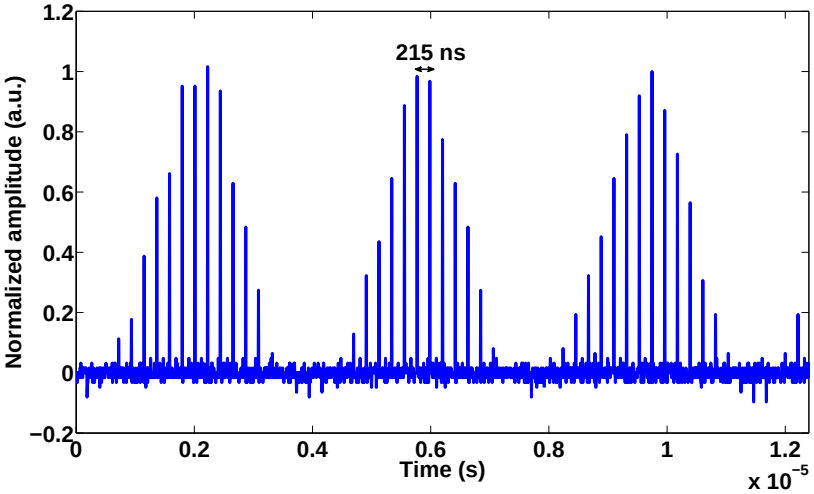

Figure 4.11: Train of pulses emitted by the Q-switched mode-locked F8L, for a pump current of 42.6 mA. The distance between the pulses is approximately 215 ns corresponding to a repetition rate of 5 MHz

Q-switching. First of all, the gain saturation dynamics has been changed and, in particular, the EDF is shortened. The motivation for shortening the EDF can be explained considering that the mode-locked equation for fast saturable absorbers can not have stable solutions for cavities with a too high small-signal gain [94]. To reduce the small-signal gain and also to enhance the saturation of the gain, the length of the EDF needs to be shorter. Along with the shorter EDF, the cavity length is also reduced to keep the total dispersion low and slightly negative in this second configuration. This is done to try to reach a more stable regime for fundamental soliton propagation. For this reason, the SSMF for each component of the F8L is reduced and the DSF is removed from the cavity. The reason to remove the DSF is that it does not have significant impact on the total dispersion cavity, but it is relevant in terms of loss. In particular, the loss per splice between the DSF and the SSMF is around 0.8 dB and, due to the lower gain that can be obtained from a shorter EDF, such an amount of loss can be a limitation. Furthermore, employing only the EDF and the SSMF can ease the dispersion management inside the cavity. However, to keep an asymmetry on the NALM and enhance the accumulation of the nonlinear phase shift, the DSF is substituted by a shorter piece of SSMF. The second configuration is described in the following section.

4.4.2 Mode-Locked F8L

The modified F8L setup is shown in Fig. 4.12. The NALM consists of 5 m

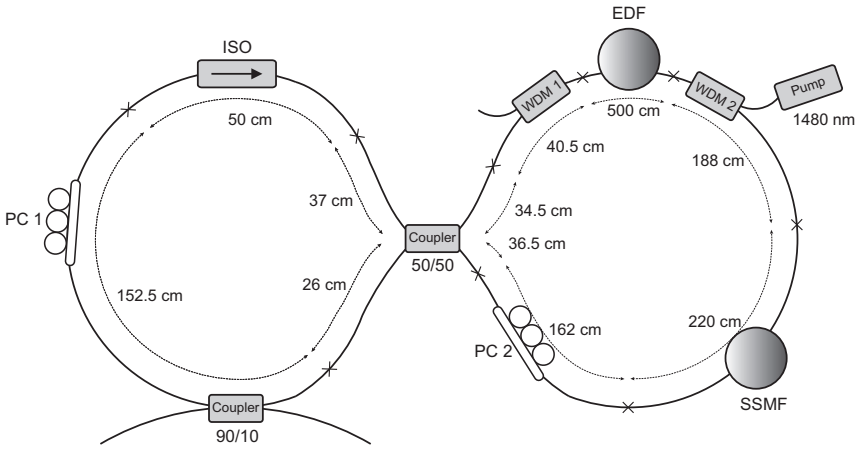

Figure 4.12: Schematic of the F8L setup working in CW mode-locking regime. EDF: erbium-doped fiber; WDM: wavelength division multiplexer; SSMF: standard single-mode fiber. ISO: isolator; PC: polarization controller.

of EDF and 6.82 m of SSMF. The resonator is composed only of a SSMF length of 2.65 m and the total cavity length is approximately 14.47 m. Considering the same dispersion values of Fig. 4.7 for the SSMF and the EDF, and calculating the total cavity dispersion according to Eq. 4.2, the new configuration results in a cavity with a small negative dispersion of -0.0288 ps^2. The negative dispersion should favor the creation of solitons. The 5 m EDF gain and ASE spectra are shown in Fig. 4.13. The main peak is still at 1530 nm, but stable mode-locked operation can be obtained only at 1560 nm. A pump current of 300 mA is used to start the mode-locking and then is decreased to 57 mA, i.e. the minimum current to sustain the mode-locking. In this configuration, a higher pump current is necessary to provide the right amount of gain to compensate the total loss, since the EDF is shorter. However, stable CW mode-locking is achieved and the spectra for different pump current is shown in Fig. 4.14. The spectrum is shown for different currents because, even if it is possible to have a sable CW mode-locking for all of them, for the higher current values (64 mA and 71 mA) a sideband at longer wavelengths is obtained. The sideband, also known as Kelly sideband, can be explained by the fact that now the total cavity dispersion is negative and the laser works in the soliton regime. In

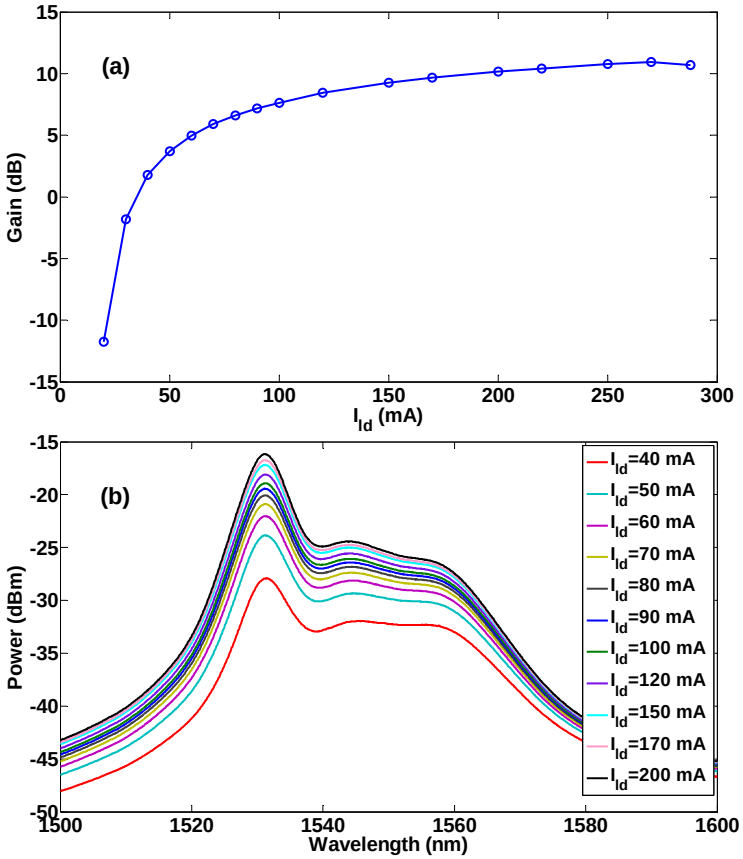

Figure 4.13: a) EDF gain as a function of the pump power for a signal at 1550 nm and input power $P_s = 0$ dBm. (b) Amplified spontaneous emission of the EDF for different pump currents.

particular, due to the discrete or localized nature of the gain and loss, the soliton experienced periodic intensity variations within the cavity, which result in sidebands [105]. The F8L is, then, run at the lower current. The FWHM bandwidth is approximately 10.7 nm, which corresponds to a pulse width of 235 fs for a transform-limited pulse. The expected repetition rate for a cavity of 14.47 m is approximately 14 MHz, which is confirmed by the measurements with an oscilloscope. In particular, a digital oscilloscope with a 10 GS/s real time sampling rate is used to measure the pulse train and the result is shown in Fig. 4.15(a). The pulses are of the same amplitude and they do not show the typical modulation of the Q-switching. This is seen

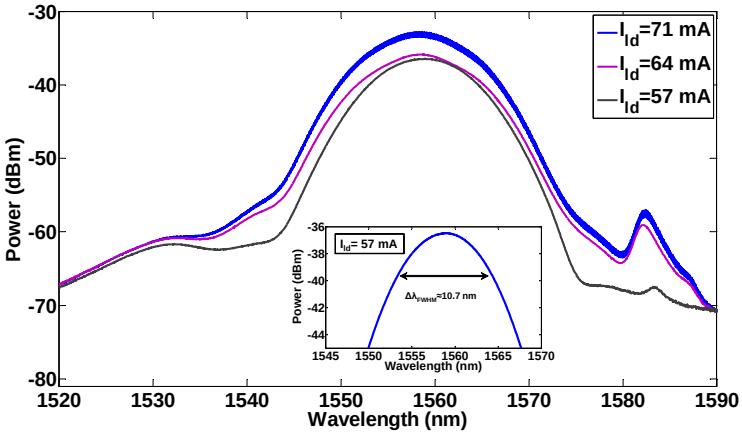

Figure 4.14: Power spectrum of the mode-locked laser for different pump current. The FWHM spectrum for $I_{ld} = 57$ mA is shown in the inset and is approximately 10.7 nm.

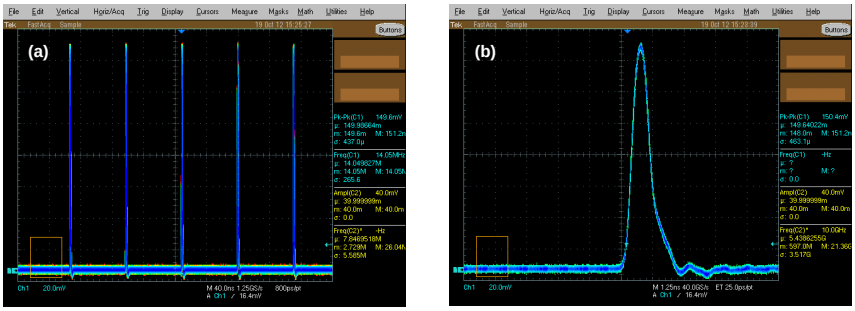

Figure 4.15: Train (a) and single (b) pulses emitted by the mode-locked F8L e for a pump current of 57 mA.

also from the single pulse measurement in Fig. 4.15(b), where the sampled values of the pulse amplitude overlap completely and a clear thin line is displayed by the oscilloscope. The measured average power is 23 μW and, thus, the corresponding peak power is estimated to be 6.8 W, considering transform-limited pulses of 235 fs. In order to measure the pulse width an autocorrelation measurement needs to be performed, but the low average power emitted by the laser complicates this measurement as discussed in the following subsection.

Limitation

The F8L emitted an average power of 23 μW, which is too low to measure a good quality autocorrelation with a high resolution on the order of femtoseconds. In particular, the autocorrelator allows to measure autocorrelation traces with resolutions of 1 fs, 10 fs, 0.1 ps and 0.3 ps. However, it has only been possible to obtain an autocorrelation using a resolution of 0.3 ps. In this case, the photomultiplier in the autocorrelator, which detects the pulses generated by second harmonic generation (SHG), is open for a longer time and is, thus, integrating the power longer. However, for pulses on the order of few hundreds of fs, it is not possible to have a good estimation of the pulse width using such a long resolution. In particular, the pulse autocorrelation is not symmetric and is distorted by a long tail. This is due to the fact that when the photomultiplier is integrating the power for a longer time, the time needed to the power in the saturated photomultiplier to go back to zero is longer than the pulse duration if the pulse is much shorter than the set resolution. Therefore, a higher resolution (few fs) should be used and this means that a higher average power is necessary. To achieve that, a preamplifier is used. In particular, an EDFA emitting up to 17 dBm is employed, setting the output power to 10 dBm. The resulting amplified optical spectrum and autocorrelation using 10 fs resolution are shown in Fig. 4.16. The spectrum is considerably distorted

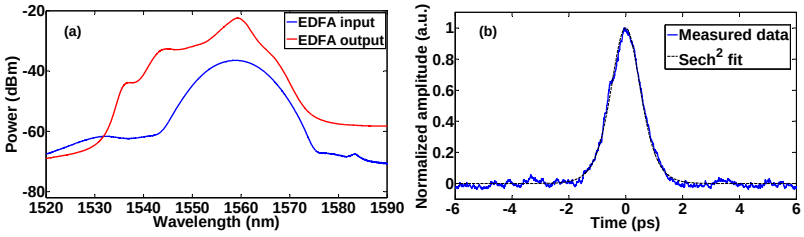

Figure 4.16: (a) Power spectrum of the F8L at the input, i.e. the laser output, and the output of the EDFA. (b) Autocorrelation trace of the pulses at the output of the EDFA.

by the wavelength dependence of the gain of the EDFA, even if the autocorrelation trace does not show any distortion from the soliton (sech^2) pulse shape. Other low power EDFAs are tested, including an EDFA built with the same fiber of the laser, but they do not give any improvement. The obtained amplified spectra are too distorted to be employed for characterizing the amplification effects on short pulses propagating into a FOPA. As

a consequence, for the experiment described in the next chapter another laser source is used. The laser is built by OFS Fitel Denmark and used for supercontinuum generation in highly nonlinear fibers [103]. The laser emits pulses as short as 135 fs with a repetition rate of 28 MHz. The FWHM bandwidth is approximately 32 nm. Such a broad bandwidth is not practical when working with single-pump FOPAs. In fact, the 3 dB bandwidth of the single-pump FOPA employed in the experiment, described in the next chapter, is on the order of 10 to 15 nm, depending on the pump power and wavelength. Therefore, the laser output was filtered to fit the FOPA gain bandwidth. To do that, a Gaussian tunable optical bandpass filter (TBPF) with 9 nm FWHM bandwidth has been employed and the setup is shown in Fig. 4.17. The isolator and the polarization controller are used to block

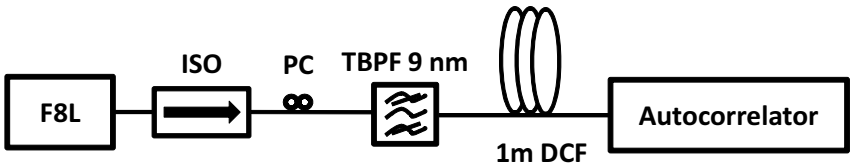

Figure 4.17: Power spectrum (a) and autocorrelation traces(b) of the F8L in [103] at the input, i.e. the laser output, and the output of a 9 nm Gaussian filter.

the reflected light and to align the signal polarization with the crystal for the SHG inside the autocorrelator, respectively. The spectra at the input, i.e. output of the F8L, and output of the TBPF are shown in Fig. 4.18. Since the laser bandwidth is much broader than the TBPF bandwidth, the

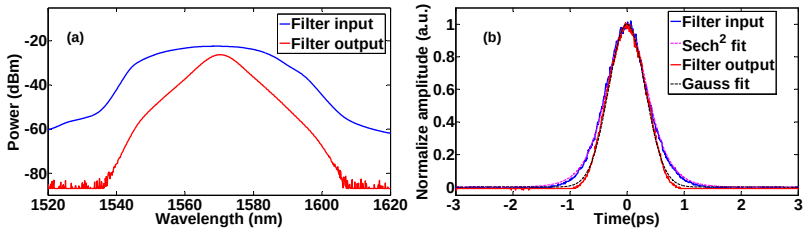

Figure 4.18: Schematic of the setup to generate a short pulses compatible with the experiment described in Chap. 5

pulse spectrum at the output of the filter is determined by its transmission function and is, thus, Gaussian. It is expected that also the filtered pulses autocorrelation is Gaussian and this is confirmed by the measured autocor-

relation traces in Fig. 4.18(b). The autocorrelation of the filtered pulses is slightly narrower than the autocorrelation of the input pulses probably due to the dispersion of the TBPF, compressing part of the pulse. Furthermore, a FWHM pulse width of 530 fs is obtained from the deconvoluted autocorrelation traces, which is broader than the one expected for transform-limited pulses (395 fs). Therefore, the pulses at the output of the filter have a chirp due to the group-velocity dispersion of the fiber connecting the laser with the autocorrelator. In order to compensate for the dispersion and remove the chirp, 1 m of dispersion compensating fiber (DCF) is used after the filter to obtain transform limited pulses for 9 nm FWHM bandwidth. The autocorrelation of the obtained pulses is shown in Fig. 4.19. The measured deconvoluted pulse width after compression is approximately 400 fs. The pulses are used in the next chapter as input signal for the FOPA.

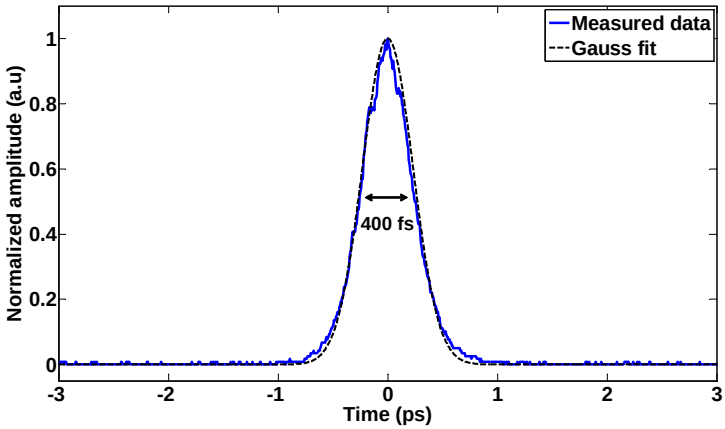

Figure 4.19: Autocorrelation trace of the compressed pulses at the output of the 9 nm Gaussian filter.

4.5 Summary

In this chapter, the realization of a short pulse all-fiber source was described. The laser configuration chosen to obtain the pulses source is the so-called figure-of-eight laser (F8L). First, the F8L working principle, based on the Kerr effect, has been briefly introduced. Second, the laser implementation process was covered, starting from a first setup for which only

Q-switched mode-locking could be obtained to arrive to the final setup providing mode-locked pulses. The spectral bandwidth of the emitted pulses was approximately 10.7 nm for a repetition rate of 14 MHz. However, the laser presented a limitation in the emitted power. In particular, the average power was approximately 23 μW, too low to measure the pulse autocorrelation with a good resolution. Therefore the pulse width of the emitted pulses could not be measured and it was only estimated to be 235 fs for transform-limited pulses, giving 6.8 W of peak power. Due to this limitation, the laser could not be used as a source for the amplification experiment in FOPAs and, therefore, a different laser was used. The laser used has been implemented by OFS Fitel Denmark and employed in [103], as a source for supercontinuum generation. However, due to the too broad bandwidth of the emitted pulses spectrum with respect to the single-pump FOPA gain bandwidth, the laser output has been filtered by means of a 9 nm Gaussian filter and the pulses have been compressed by 1 m of dispersion compensating fiber to provide transform-limited pulses of 400 fs with a 9 nm FWHM broad spectrum.

Chapter 5

Short-Pulse Propagation in Single-Pump Phase-Insensitive FOPAs

5.1 Introduction

Optical amplification of signals reaching multi-terabit per second per channel is becoming increasingly relevant and fiber optical parametric amplifiers (FOPAs) relying on highly nonlinear fibers (HNLFs) are promising candidates thanks to their inherent compatibility with fiber optic systems and their ability to provide gain over a broad bandwidth, limited only by the fulfillment of the phase matching condition (Eq. 2.11) and the availability of a pump laser source. Furthermore, optical parametric chirped pulse amplification (OPCPA) has been demonstrated to be a valid technique for the amplification of ultrashort pulses with high peak powers [106]. Therefore, OPCPA in fiber has attracted attention in the recent years with few demonstrations of its potential for amplification of short pulses both at telecommunication wavelengths [18, 19, 23] and in the 1 μm wavelength region [21, 22].
In this Chapter, a brief overview of OPCPA is provided in Sec. 5.2 together with a description of the achievements obtained by its implementation in optical fibers. The dynamics of fiber optical parametric chirped pulse amplification (FOPCPA) of nearly transform-limited Gaussian pulses with a pulse width on the order of 400 fs are investigated in Sec. 5.3, both nu-

merically and experimentally, considering unsaturated as well as saturated regimes. In Sec. 5.4, FOPCPA of 400 fs pulses is demonstrated for the first time, opening the way to parametric amplification of Tbaud single wavelength channel signals [24–26].

5.2 Optical Parametric Chirped Pulse Amplification

Optical chirped pulse amplification (OCPA) was proposed for the first time by Strickland and Mourou in 1985 [107], in order to produce short pulses ($\lesssim$ 1 ps) at Joule energy level, transposing the chirped pulses amplification techniques employed in RADAR systems to the optical domain. The basic idea behind OCPA is to allow for amplifiers to deal with high peak powers emitted by short pulse lasers, avoiding the effects due to the optical nonlinearities, such as self-focusing and self-phase modulation. This is achieved by stretching in time the input pulsed signal by means of a dispersive element, in order to reduce its peak power. The basic scheme of OCPA is shown in Fig. 5.1. The input signal pulses are first passing through a

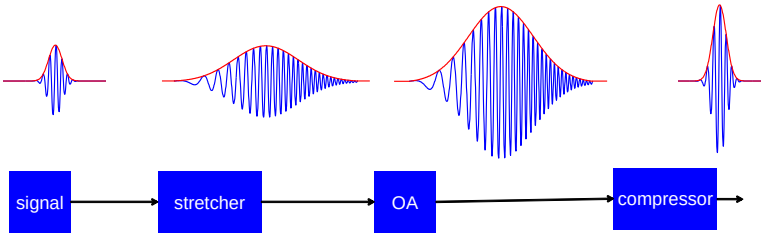

Figure 5.1: Schematic of OCPA.

dispersive media (stretcher), such as diffraction gratings or fibers, in order to be stretched in time, while preserving their spectral characteristics. The chirped pulses at the output of the stretcher have a lower peak power and can be efficiently amplified without distortions. The amplified output pulses are still chirped and with relatively low peak powers. Afterwards, they can be compressed back in order to obtain an amplified copy of the input pulses.

The scheme presented in Fig. 5.1 is also valid for OPCPA, though in this case the optical amplifier is replaced by an optical parametric amplification scheme, which can be realized using nonlinear crystals or HNLFs. OPCPA

was demonstrated for the first time in 1992 by Dubietis *et al.* [108], employing diffraction gratings for the stretching and compression stages and a Barium borate crystal to obtain parametric amplification, providing 70 fs compressed pulses with 0.9 GW of peak power. However, OPCPA systems based on nonlinear crystals are cumbersome and require a careful alignment of the pump and signal waves in order to satisfy the phase matching condition. All-fiber systems can overcome this limitations, bringing advantages in terms of compactness, reliability and long-term stability. Therefore, FOPCPA constitutes a promising technique for the amplification of short pulses. FOPCPA has been presented for the first time in 2006 by Hanna *et al.* [20] in a numerical study, where the advantages of amplification of femtosecond pulses in a FOPCPA scheme were shown. Experimental demonstrations of FOPCPA followed, considering picosecond [18, 19] and subpicosecond [23] pulses in the 1.5 μm region. In [18], 6.4 ps pulses have been investigated both in linear and saturated regime, using a single chirped fiber Bragg grating (CFBG) as both stretcher and compressor. A small-signal gain of ~ 25 dB was obtained and a compression of the pulses in the saturated amplifier was demonstrated. Moreover, distortion effects in the form of pedestals appearing around the signal, due to the saturation of the parametric amplifier, have been reported in [109], where the dynamics of FOPCPA at 1 μm have been numerically investigated. The appearance of pedestals due to excess quantum noise was also reported in case of OPCPA [110]. However, a study of the saturation distortion effects in the 1.5 μm region has not been reported yet. In the next section, a dynamic characterization of FOPCPA of Tbaud-class pulses is presented both numerically and experimentally.

5.3 Dynamic Characterization of FOPCPAs

In this section, a dynamic characterization of a FOPCPA scheme for amplification of short pulses compatible with Tbaud communication systems is presented. First, a numerical investigation of the amplification of nearly transform-limited Gaussian pulses on the order of 400 fs is reported. Then, an experimental characterization is also performed to set the best FOPCPA scheme for the amplification of such short pulses, confirming the general expectations predicted by the numerical model.

5.3.1 Numerical Characterization

The signal, pump and fiber parameters for the numerical characterization of the FOPCPA are set based on the experimental setup, which is described in the next section. In particular, a HNLF with a non-linear coefficient of 10.7 $W^{-1} \cdot km^{-1}$, a zero-dispersion wavelength (ZDW) at 1550.4 nm and a dispersion slope of 0.018 $ps/(nm^2 \cdot km)$ is considered. The pump signal wavelength is 1554 nm and the power is equal to 29 dBm. The pump parameters choice is explained in the following section where the experimental characterization of the HNLF by measuring the continuous wave (CW)-gain (i.e. the gain spectra obtained by using a CW source to generate the input signal) is reported. The signal pulses spectrum is centered at 1571 nm with a full-width at half maximum (FWHM) bandwidth of 9 nm, similarly to the laser source employed in the experimental characterization. The schematic of the setup considered for the implementation of the numerical model is shown in Fig. 5.2. The pulses are at first stretched in a 309 m-long fiber

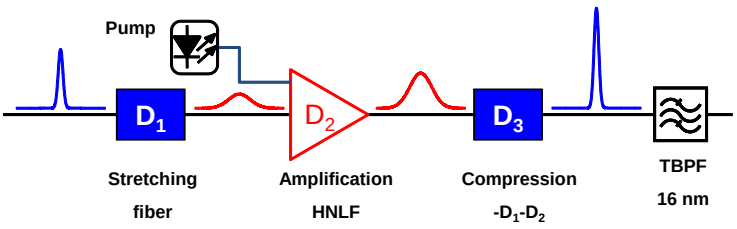

Figure 5.2: Schematic of the setup for the numerical characterization of the FOPCPA. $D_{1,2,3}$ are the dispersion parameters of the stretcher, the HNLF and the compressor, respectively. TBPF:tunable optical bandpass filter

characterized by a dispersion $D_1 = 18$ $ps/(nm \cdot km)$. After the stretching, they propagate into the HNLF with the characteristic parameters specified above and, then, a compressor compensates for the stretcher and the HNLF dispersions ($D_3 = -(D_1 + D_2)$). After the compression stage, a tunable optical bandpass filter (TBPF) with a FWHM bandwidth of 16 nm is employed to select the output pulses. The energy gain and the pulse FWHM are considered for the characterization of the FOPCPA.
First, the dependence of the energy gain on the input pulse energy is investigated for different lengths of the amplification fiber (HNLF) and the results are shown in Fig. 5.3. The energy gain of the pulses starts to decrease as the input pulse energy increases. This effect is dependent on the length of the fiber and, then, on the signal gain of the amplifier (See Sec. 2.4.4). The

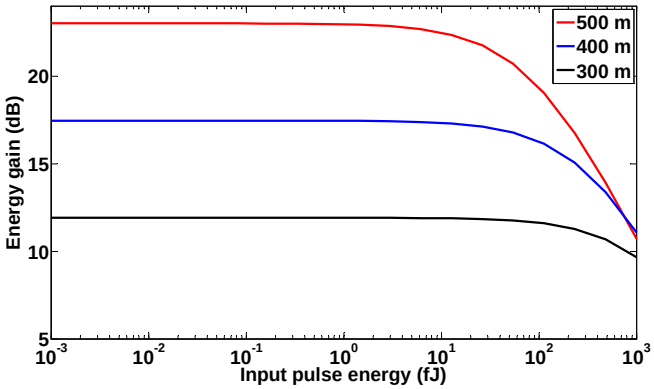

Figure 5.3: Energy gain as a function of the pulse input energy for three different HNLF lengths.

longer the fiber, i.e. the higher the signal gain at the output of the FOPA or the FOPCPA, the stronger are the saturation effects on the pulse energy gain. The consequences of gain saturation on the pulse FWHM are shown in Fig. 5.4(a). A broadening of the pulses is observed for all the three fiber lengths due to the amplification in the FOPCPA. It is also noted that, increasing the input pulse energy, the FWHM is reduced and, thus, the pulses compresses. However, it can be seen from Fig. 5.4(b) that, if the root mean square (RMS) of the pulse widths are considered, they increase with an increasing input energy. This is due to the appearance of pedestals around the signal pulses for saturated FOPCPA. In fact, the FWHMs are smaller, but the pulse energy increases in the trailing and leading edges of the pulses. Therefore, the pulses are distorted and lose their Gaussian pulse shape [109, 110]. This can be seen in Fig. 5.5, where the output compressed pulse for an input pulse energy of 7 pJ (−7 dBm average power) is shown along with the input pulse. A second pulse appears when the amplifier is operating in saturation and its amplitude increases with an increasing input energy.

Secondly, the input pulse energy is fixed at 70 fJ (−27 dBm of signal average power), for which the amplifier is slightly saturated, and the dependence of the energy gain and the pulse FWHM on the HNLF length is investigated. The results are shown in Fig. 5.6. As expected [28], longer HNLFs lead to higher energy gains as shows Fig. 5.6(a). However, after a certain length the energy gain starts to decrease with further increasing of the fiber length. This is due to the change of direction of the power flow from the pump

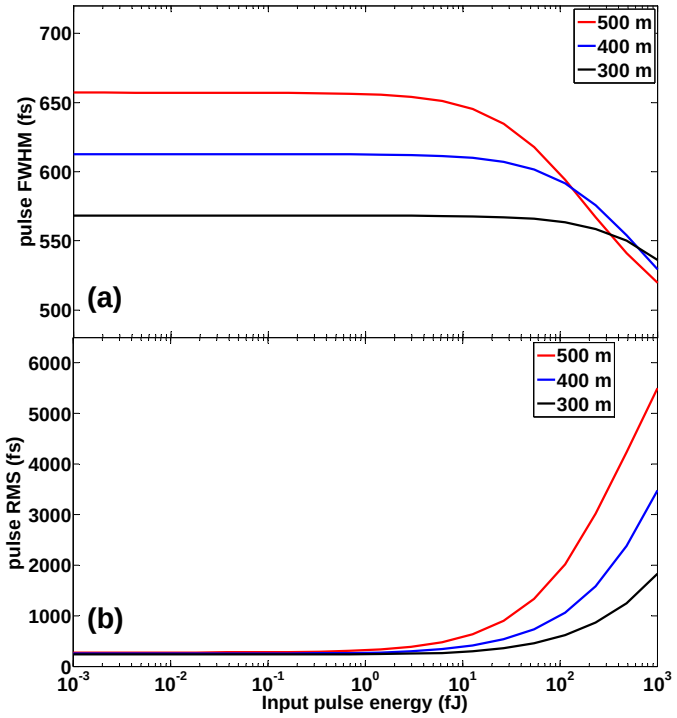

Figure 5.4: Pulse FWHM (a) and RMS pulse width (b) as a function of the pulse input energy for three different HNLF lengths.

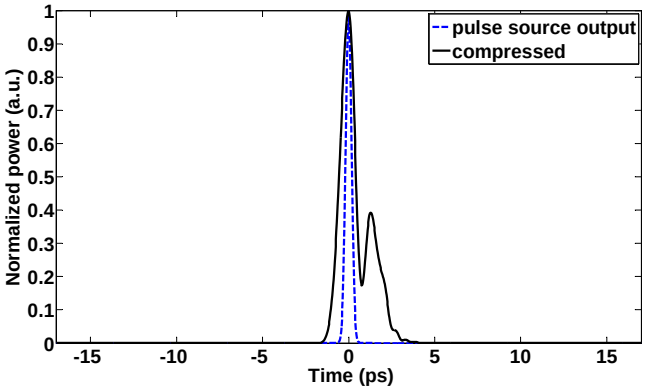

Figure 5.5: Input (dash line) and output compressed (solid line) pulse for an input energy of 7 pJ.

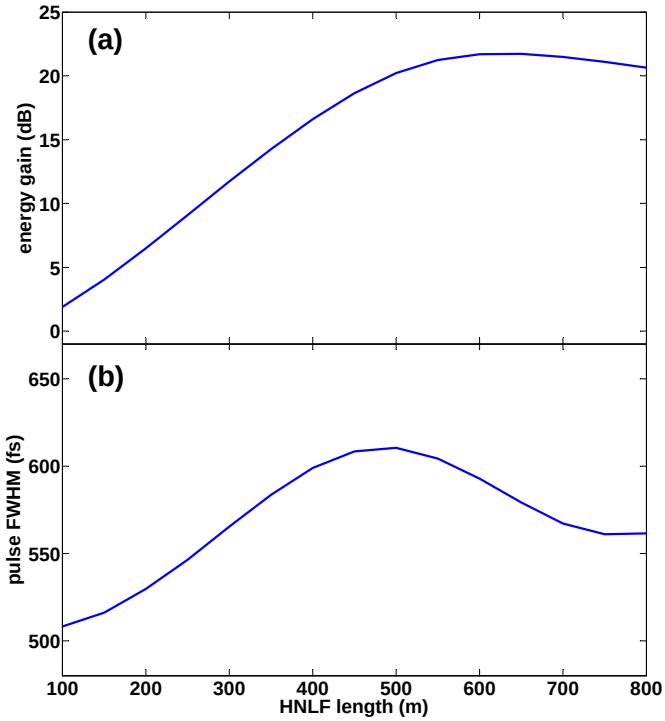

Figure 5.6: Energy gain (a) and pulse FWHM (b) as a function of HNLF length for an input pulse energy of 70 fJ.

to the signal in saturated FOPAs, for which, above a certain interaction length, the power is transferred back from the signal to the pump. Similarly, the pulse FWHM in Fig. 5.6(b) increases with the fiber length until a certain fiber length. After this length, the pulses are still broader with respect to the input pulses but by a smaller amount. This shows a close correspondence between the energy gain and the pulse FWHM behaviors in the FOPCPA.

In conclusion, a broadening of the pulses is expected due to the amplification and this is smaller for FOPCPA operating in the saturated regime. However, pulse distortion is also observed when the saturation of the amplifier is reached. In the next section, these effects are experimentally investigated in terms of on/off signal gain and FWHM of the pulse autocorrelation traces.

5.3.2 Experimental Characterization

In this section, the FOPCPA is experimentally investigated to gain a general notion of its behavior when pulses as short as 400 fs are considered at its input and to find the best configuration for the amplification of the Tbaud-class pulses, which is demonstrated at the end of this chapter.

Experimental Setup

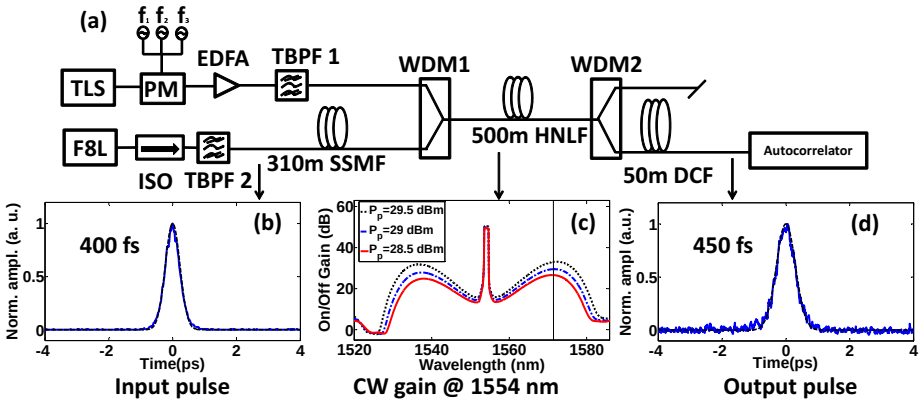

Figure 5.7: (a) Experimental setup of the FOPCPA for the pulses dynamic characterization. (b) Autocorrelation trace of the 400 fs input pulse; (c) CW FOPA gain for two different pump levels (the vertical line indicates the signal central wavelength); (d) compressed output pulse autocorrelation measured with the pump signal switched off.

The experimental setup is shown in Fig. 5.7(a). A CW tunable laser source (TLS) is used as pump source ($\lambda_p = 1554$ nm) and the emitted light is subsequently phase modulated to broaden the pump spectrum in order to increase the stimulated Brillouin scattering (SBS) threshold. The pump is then amplified in an erbium-doped fiber amplifier (EDFA) and a tunable optical bandpass filter (TBPF1) with a 0.8 nm FWHM bandwidth is used to suppress the out-of-band amplified spontaneous emission (ASE) noise introduced by the EDFA. The pump wavelength is chosen only a few nanometers above the HNLF zero-dispersion wavelength (1550.4 nm) in order to have a gain as uniform as possible over a broad bandwidth. On/off CW-gains of the FOPA under investigation are shown in Fig. 5.7(c) for three pump input power levels. The vertical line indicates the signal

central wavelength used for pulse amplification. It is noted that the signal is centered with respect to one of the lobes in the FOPA gain spectrum for a pump input power of 29 dBm, providing a CW on/off gain of 28 dB. Centering the pulses spectrum with respect to the FOPA gain is important to reduce the filtering effect due to the limited FOPA gain bandwidth and, thus, avoid a strong spectral pulse distortion.
The signal is generated by a mode-locked figure-of-eight laser (F8L) [103], filtered with a 9 nm broadband filter (TBPF2) to generate Gaussian pulses at 1571.6 nm with a FWHM of 400 fs and a 28 MHz repetition rate. The autocorrelation trace of the obtained pulses is shown in Fig. 5.7(b). The time-bandwidth product (TBP) of the generated pulses is 0.443, corresponding to that of Gaussian transform-limited pulses. An isolator (ISO) is placed at the output of the F8L to prevent back reflected light from affecting the mode-locking. The signal pulses are stretched to approximately 50 ps in 310 m of standard single mode fiber (SSMF) in order to avoid saturation of the FOPA or supercontinuum generation in the HNLF [103]. They are then combined with the pump via a wavelength division multiplexing (WDM1) into a 500 m-long HNLF, with a non-linear coefficient of 10.7 $\mathrm{W}^{-1} \cdot \mathrm{km}^{-1}$ and dispersion slope of 0.018 $\mathrm{ps}/(\mathrm{nm}^2 \cdot \mathrm{km})$. The signal at the output of the HNLF is filtered by WDM2 and then compressed with a 50 m-long dispersion compensating fiber (DCF), with a total dispersion of 5.89 ps/nm at 1550 nm. To characterize the broadening of the pulses due only to the amplification, the length of DCF is adjusted to achieve the minimum signal pulse width at its output when the pump is turned off. Figure 5.7(d) shows the corresponding autocorrelation trace.

Experimental Results

A characterization of FWHM of the pulses autocorrelations (T_{FWHM}) in unsaturated and saturated regimes, i.e. at signal input average power levels of -27 dBm and -7 dBm respectively, has been performed as a function of the pump input power to the HNLF. The results are shown in Fig. 5.8(a) along with the corresponding on/off gain measurements in Fig. 5.8(b). Figure 5.8(a) shows that T_{FWHM} increases with increasing pump power, i.e. increasing gain, both in the saturated and the unsaturated regimes. When the pump power is off the output pulse width is approximately 450 fs, but, as the pump is turned on and the input pulsed signal is amplified, the pulse width broadens. In particular, considering

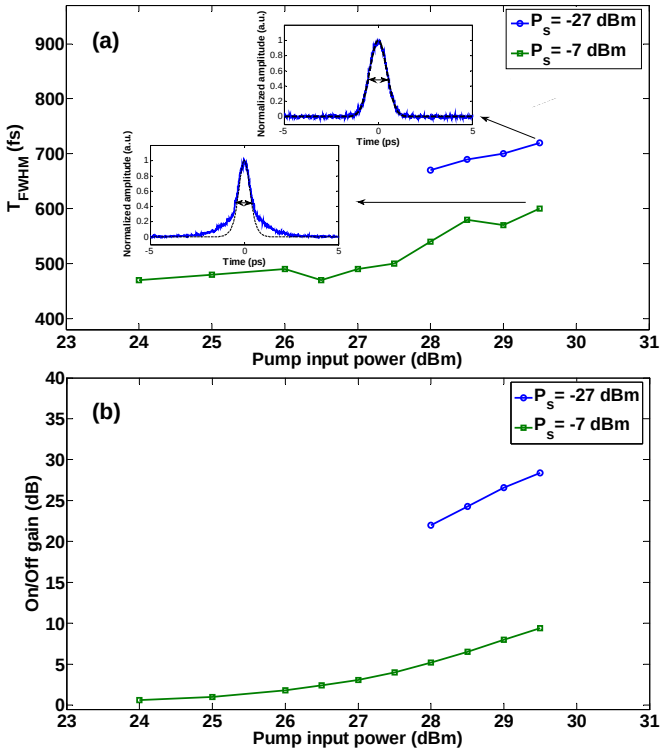

Figure 5.8: (a) pulse width of the amplified signal as a function of pump power at the input of the HNLF in the saturated ($P_s = -7$ dBm) and unsaturated ($P_s = -27$ dBm) regimes. The insets show selected autocorrelation traces. (b) Corresponding measured on/off gain.

the optimal pump power $P_p = 29$ dBm, for which the signal is centered with respect to one of the lobes in the FOPA gain spectrum, T_{FWHM} is 700 fs and 570 fs for signal input average power levels of -27 dBm and -7 dBm, corresponding to 26 dB and 7.5 dB of amplification, respectively. The pulse broadening needs to be compensated for the short pulses amplification experiment. The insets show autocorrelation traces fitted with Gaussian pulse shape curves. When the FOPCPA is saturated, a higher energy with respect to the unsaturated regime is observed in the leading and trailing edges of the pulse and the appearance of these pedestals causes discrepancies with the Gaussian fit. For -7 dBm of signal input average power, T_{FWHM} is reduced by approximately 20% compared to a signal input average power of -27 dBm, considering the same pump input power.

The reduction of the FWHM of the pulses due to saturation in FOPCPAs is confirming the trend shown by the numerical characterization, where the real pulse FWHMs were considered instead of the FWHMs of the pulse autocorrelation traces. As mentioned in Sec. 5.2, the compression of the pulse width in saturated FOPCPA has already been shown in [18]. However, no signs of pulse reshaping were reported. This may be explained by the lower dispersion effects experienced by the 6.4 ps pulses with respect to the 400 fs pulses employed in this experiment. In fact, in [109], where shorter pulses were investigated numerically, the same authors showed the appearance of pedestals when the FOPCPA operated in saturation regime. The increased energy on the leading and trailing edges of the pulses is

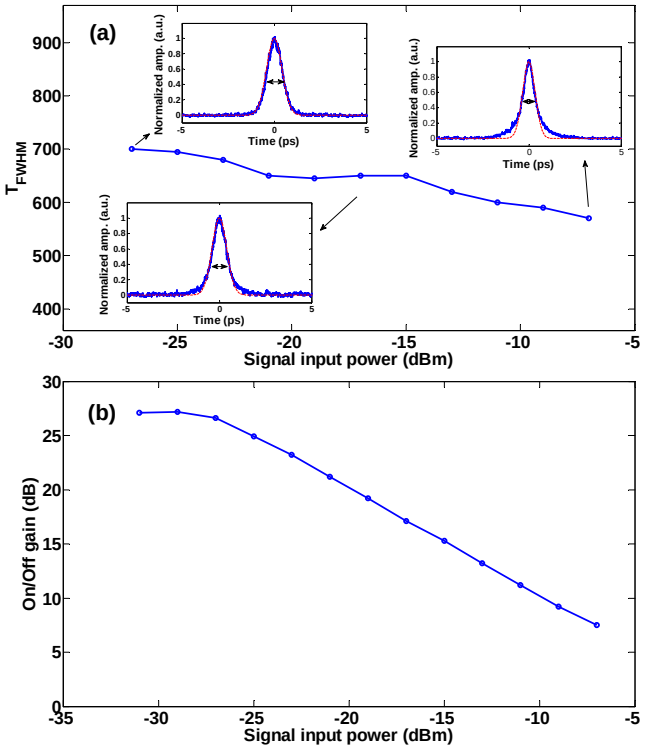

Figure 5.9: (a) pulse widths of the amplified signal as a function of the signal input average power with a pump power of 29 dBm. The insets show selected autocorrelation traces. (b) Corresponding measured on/off gain.

attributed to the interplay between self-phase modulation (SPM), high order dispersion and the limited gain bandwidth in the FOPCPA, reshaping

the pulses and thereby decreasing T_{FWHM}. This effect is better observed in Fig. 5.9(a) and (b), where the pulse width of the amplified signal is shown as a function of the signal input average power together with the corresponding on/off gain. It is noted that T_{FWHM} decreases as the signal power is increased, while pulse reshaping appears as saturation is gradually reached. In fact, from the insets it is observed that the discrepancies with the Gaussian fit increase with increasing signal input average power. To understand the narrowing of the pulses in the time domain, optical spectra at the output of the HNLF are considered in Fig. 5.10. The optical spectra are measured with the pump power (29 dBm) switched on and off for $P_s = -27$ dBm and $P_s = -7$ dBm. The steep edges in the signal spectra

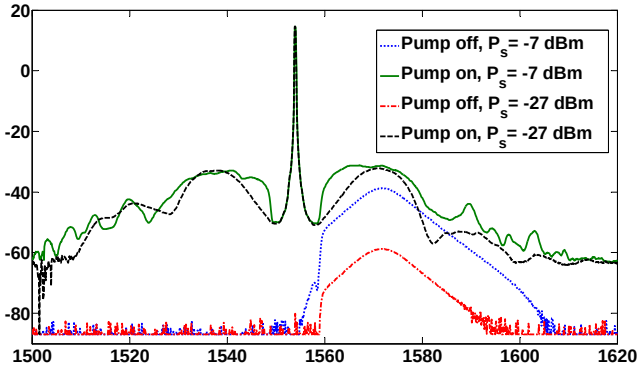

Figure 5.10: Optical spectra measured at the output of the HNLF with the pump switched off and on ($P_p = 29$ dBm) for $P_s = -27$ dBm and $P_s = -7$ dBm.

with the pump turned off are due to WDM1, which couples the signal with the pump (the wavelength dividing the pass band and the reflection band is approximately 1559 nm). A broadening of the signal spectrum is visible when the amplifier operates in the saturated regime compared to the unsaturated regime, validating a narrowing of the pulse width in the time domain. In particular, a broadening of the FWHM spectrum from 9 nm to approximately 14 nm is observed in the spectra for a signal input average power of -7 dBm. In the unsaturated regime (i.e. $P_s = -27$ dBm), the FWHM of the spectrum remains unchanged at 9 nm. This, together with the fact that no reshaping of the pulse is observed, makes the unsaturated regime more suitable for the amplification experiment of very short pulses. Therefore, the amplification scheme of the 400 fs pulses is set by choosing a

signal input power of −27 dBm and a pump input power of 29 dBm. This experiment is described in the next section.

5.4 Amplification of 400 fs Pulses in FOPCPA

In this section, the experimental demonstration of fiber optical parametric amplification of 400 fs pulses in the unsaturated regime is reported. The experimental setup is shown in Fig. 5.11. With respect to the setup shown

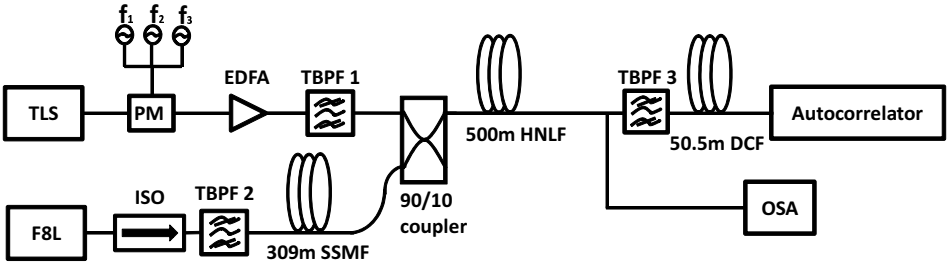

Figure 5.11: Experimental setup of the FOPCPA for the amplification of the 400 fs pulses with a pump input power of 29 dBm and signal input average power of −27 dBm.

in Fig. 5.7, a 10 dB coupler and a filtering stage made by a cascade of three broadband filters (TBPF3) replace here the wavelength division multiplexers WDM1 and WDM2, respectively. The stretching/compression stages are also different, since the compression is now optimized when the signal is amplified and the amplification adds chirp to the pulses, as described in Sec. 5.3.2. The pump wavelength is set at 1554 nm and the pump power is 29 dBm, resulting in an on/off CW-gain of 28 dB. The 400 fs signal is stretched by 309 m of SSMF, amplified by 26 dB and then compressed back to 500 fs by a 50.5 m-long DCF. The spectrum of the pulsed signal at the output of the HNLF is shown in Fig. 5.12 when the pump is either switched off or on. The on/off gain at the signal wavelength is 26 dB, i.e. 2 dB lower than the CW gain. This is due to the fact that the amplifier is working close to the saturated regime. It is necessary to find a compromise between the stretching factor and the saturation of the amplifier. A too low stretching factor, i.e. a too high peak power, saturates the amplifier, while a too high stretching factor makes the dispersion management needed to

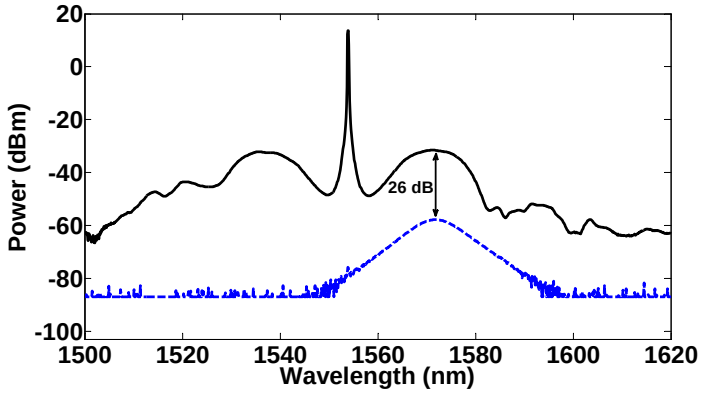

Figure 5.12: Optical spectra measured at the output of the HNLF with the pump switched off (dashed blue line) and on (solid black line) with a pump power of 29 dBm.

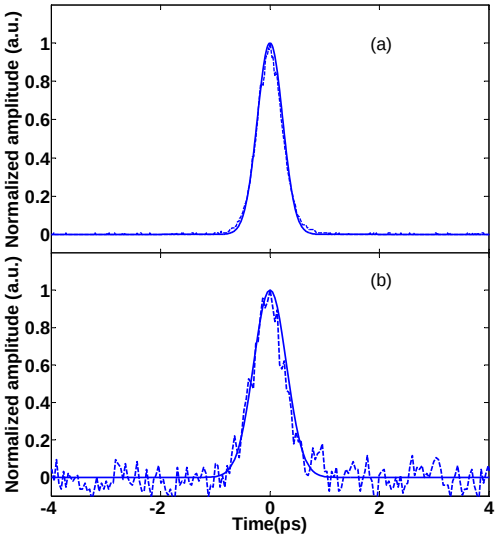

Figure 5.13: Autocorrelation traces of the signal (a) at the input of the SSMF, corresponding to a pulse width of 400 fs and (b) at the output of the DCF, corresponding to a pulse width of 500 fs.

compress back the pulse after amplification challenging. The peak power of the signal after the filtering stage and the compression is measured to be around 9.3 W for a pulse width of 500 fs. The autocorrelation traces

measured before the stretching SSMF and after the amplification and compression in the DCF are shown in Fig. 5.13(a) and (b), respectively. The noise on the output trace is due to the high losses in the filtering stage. The measured data was fitted to a Gaussian curve. The compressed pulse is broader with respect to the input pulse by approximately 100 fs. This is believed to be due to two main factors. First, the lack of compensation of high-order dispersion terms adds some chirp to the pulse. In fact, the pulses were stretched by more than two orders of magnitude in the SSMF and even in the dynamic characterization experiment discussed in Sec. 5.3.2, it was not possible to completely compress the pulses back to 400 fs, but only down to 450 fs. Since other effects, apart from the dispersion, were not acting on the pulses when the pump was switched off, the difference between the pulses at the input of the stretcher and at the output of the compressor can only be explained by the lack of compensation of higher-order dispersion terms. Secondly, a significant pulse broadening was observed possibly owing to the limited gain bandwidth of the FOPA, introducing a frequency filtering effect. This broadening was only partially compensated at the output of the DCF.

5.5 Summary

In this chapter, optical parametric chirped-pulse amplification has been introduced and an overview of the state-of-the-art of its realization in optical fibers has been presented. Nearly transform-limited Gaussian pulses on the order of 400 fs and with a repetition rate of 28 MHz are considered to investigate a fiber optical chirped pulse amplification scheme both in saturation and unsaturation regimes. First, numerical results are presented to provide a general overview on the dynamics of the amplifier with respect to such short pulses. Then, the dynamic characterization of the effects of parametric amplification on 400 fs pulses is performed experimentally, focusing on the distortion of the amplified pulses for different amplification levels. It was shown that the full-width at half maximum of the pulses is increased with increasing gain in the fiber optical parametric chirped pulse amplification. Furthermore, the pulse width compressed as saturation was reached. A broadening of the spectrum was also observed, showing that a chirp has been added to the pulse as the amplifier was saturated and validating the compression of the full-width at half maximum of the amplified pulses in saturation. However, in saturation, a higher energy with respect

to the unsaturated regime is observed in the leading and trailing edges of the pulses. The appearance of the pedestals reshaped the pulses, which cannot be considered Gaussian any longer, and showed that the saturated amplifier is unsuitable for undistorted amplification. Based on these results, we set the best FOPA configuration to demonstrate the amplification of Tbaud-class pulses in a fiber optical parametric amplifier. The 400 fs pulses were first stretched to 50 ps, amplified by 26 dB in a fiber optical parametric amplifier and then compressed back to 500 fs.

Chapter 6

Conclusion

Optical amplifiers are crucial enablers of data communication over long distances. Fiber optical parametric amplifiers (FOPAs) can be valid candidates to provide low noise and high amplification over a broad bandwidth and their inherent compatibility with fiber optical systems allows the realization of all-fiber optical communication systems, which are advantageous because of their reliability and long-term stability. In long-haul transmissions, it is important to maintain a high signal quality in terms of signal-to-noise ratio and distortion of the signal being transmitted. Therefore, the noise and distortion mechanisms for the applicability of FOPAs to the amplification of high speed signals with bit rates in excess of 1 Tbit/s per wavelength channel needs to be investigated.

In this Thesis, the pump-to-signal intensity modulation transfer (IMT), identified as the major noise contribution, and optical parametric chirped pulse amplification (OPCPA) are experimentally investigated in single-pump phase-insensitive fiber optical parametric amplifiers (PI-FOPAs) both in saturation and linear regimes. Furthermore, a laser source emitting short soliton pulses is implemented for the realization of an all-fiber optical system, for the characterization of parametric amplification of pulses compatible with Tbaud systems. However, due to the low efficiency, the laser source couldn't be used and Gaussian pulses emitted by an equivalent laser source has been employed.

Intensity modulation transfer

The IMT from the pump to the signal in PI-FOPAs has been experimentally investigated and the results are presented in Chapter 3. The investigation has first been extended over a 27 GHz modulation frequency range and compared to the analytical model developed in [81], showing a good agreement. A strong wavelength dependence of the IMT was observed. Moreover, the dependence of the IMT on the pump modulation frequency has been experimentally investigated, resulting in a reduction of the IMT with increasing modulation frequency. This can be attributed to a weak effect due to the walk-off between the pump and the signal. The numerical study of the IMT for high modulation frequencies has shown that the IMT can be considered constant and, thus, independent of the modulation frequency up to approximately 50 GHz. However, in the experimental investigation reported here, it has been noted that the IMT reduction is signal wavelength dependent. In particular, the IMT is reduced more for signals with the largest detuning from the pump. This signal wavelength dependence may only be explained by the walk-off effects due to the increasing difference between the pump and signal group velocities for signal wavelengths farther detuned from the pump. A reduction of the IMT has also been measured by operating the FOPA in the saturated regime. In particular, the IMT coefficient around the maximum gain wavelength was reduced by almost a factor 3, resulting in amplifiers with a significantly lower noise contribution from pump power fluctuations transferred to the signal. However, two main issues when operating in the saturation regime have been reported: reduced gain and increased noise spectral density. As regards the first, it has been shown that a compromise between gain and IMT reduction could be achieved by adjusting the pump power to a higher level. In this way, the same gain can be obtained in the FOPA but with a lower IMT coefficient. For the latter, instead, the investigation has shown that, in saturation, the other noise contributions of the amplifier cannot be neglected. In fact, even though the IMT decreases with increasing signal input power, the noise spectral density of the amplifier increases, which may limit the benefit due to the IMT reduction on the performance of FOPAs. The effects experimentally investigated in this work can have relevant implications for the design of single-pump FOPAs, mainly considering applications such as optical signal regeneration and wavelength conversion for which FOPAs operating in saturation regime are preferable.

Subpicosecond pulses amplification in FOPAs: pulses generation and fiber optical parametric chirped pulse amplification (FOPCPA)

A short pulse fiber laser source is implemented and described in Chapter 4 to obtain an all-fiber system. The laser configuration described is the so-called figure-of-eight laser (F8L), emitting soliton pulses centered at 1560 nm with 10.7 nm full-width at half maximum (FWHM) bandwidth. Considering transform limited sech^2 mode-locked pulses, a pulse width of the order of 250 fs is expected. The repetition rate is approximately 14 MHz, which gives an estimated peak power of 6.8 W. The limitations of the laser is the too low average power, which made it impossible to measure a high resolution autocorrelation trace without pre-amplifying the pulses. However, the pre-amplification induced a strong distortion in the pulse spectrum, which made not possible to employ it for the characterization of fiber optical parametric chirped pulse amplification (FOPCPA). Another F8L was employed to realize an all-fiber system [103], adjusting the emitted pulses to fit the FOPA gain bandwidth. Subpicosecond Gaussian pulses on the order of 400 fs, 9 nm bandwidth and centered at 1571 nm were considered to characterize experimentally a FOPCPA scheme, both in saturation and linear regimes. A broadening of the FWHM of the pulses due to amplification has been demonstrated in both regimes. In particular, it was shown that the FWHM of the pulses is increased with increasing gain. This is attributed to a combined effect of group-velocity dispersion (GVD), self-phase modulation (SPM) and limited bandwidth of the FOPA. Furthermore, it was observed that the FWHM of the pulses compressed as saturation was reached. This was due to the appearance of pedestals, which reshaped the pulses, showing that the saturated amplifier is unsuitable for undistorted amplification. Finally, based on the results obtained in the dynamic characterization, the best FOPCPA scheme was set to amplify subpicosecond pulses. Pulses of 400 fs duration were first stretched to approximately 50 ps, in order to operate on the limit of linear regime and avoid supercontinuum generation [103], amplified by 26 dB and compressed back to 500 fs.

6.1 Future developments

Subpicosecond pulses of the order of 400 fs were amplified reporting, however, a broadening of 25% when compressed back. In particular, the compressed pulse was broader with respect to the input pulse by approximately 100 fs. The imperfect compensation has been attributed to two main factors.

- The lack of compensation of high-order dispersion terms added some chirp to the pulse. This could be overcome by implementing a customized compression and delivery systems. This type of systems has been already implemented by means of cutback techniques [111], where a good optimization can be reached to minimize the lack of compensation of third-order dispersion terms.

- A significant pulse broadening was observed possibly due to the limited gain bandwidth of the FOPA, introducing a frequency filtering effect. In fact, the single-pump FOPA under investigation could be operated with a fairly flat gain over approximately 10 nm bandwidth, enough to contain the 3 dB bandwidth, but not the full pulse spectrum. Dual-pump FOPAs can overcome this limitation, since they can provide a flat gain over larger bandwidths. Subpicosecond chirped pulse amplification in double-pump FOPAs has been investigated numerically, showing the potential of exploiting a broader bandwidth for amplification of pulses of tens of femtosecond [112]. However, the applicability of double-pump FOPAs to FOPCPA has never been experimentally investigated so far. In particular, the extension of FOPCPA to dual-pump configurations can be interesting for measuring the saturation effects on the short pulses. In fact, in saturated double-pump FOPAs the creation of higher order idlers can be a significant source of cross-talk and limit the bandwidth for allocation of the signal. As a consequence, this may actually limit the applicability of two-pumps amplification scheme.

An important issue, that was not considered in this Thesis, is the creation of an idler, which is the conjugate copy of the signal. Interesting information can be retrieved by the investigation of the conversion efficiency and

distortion effects on the idler, allowing for a full characterization of the FOPCPA. In particular, it should be noted that wavelength conversion functionalities of FOPAs can be extremely relevant when considering soliton pulses. In fact, solitons can only be generated in anomalous dispersion regime or in case of normal dispersion regime when the total dispersion is really small. The creation of an idler symmetric to the signal with respect to the pump can enable the appearance of short soliton pulses in bandwidths where it is usually not possible to generate them.

The focus of this project was the characterization of pulse distortion mechanisms in FOPAs. This was done by considering 400 fs pulses with a repetition rate which was too low to be employed in optical communication systems reaching multi-terabit per second per channel. Therefore, the next step towards the amplification and long distance transmission of optical time division multiplexed (OTDM) signals at Tbaud data rate is to increase the repetition rate of the pulses under investigation so that it becomes compatible with single wavelength channel systems at bit rates of Tbit/s. In this case, other effects, apart from SPM, GVD and limited FOPA gain bandwidth, will be affecting the pulses, such as the intra-channel cross-phase modulation (XPM) and the intra-channel four-wave mixing (FWM) between adjacent pulses. The characterization and mitigation of these effects are crucial for the demonstration of a first broadband amplification scheme compatible with phase and multilevel modulated signals employed in Tbit/s transmission.

Appendix A

Network Analyzer: Two-Port S-Parameters

In this appendix, the S-parameters matrix is briefly introduced and the calculations performed in Chap. 3 in order to obtain the modulation indices of the pump and signal from the S-parameters are discussed.

A.1 S-parameters matrix

The term S-parameters indicate the elements of a scattering matrix [113]. The scattering matrix is a mathematical construction that quantifies how RF energy propagates through a multi-port network. The S-matrix is what allows to accurately describe the properties of complicated networks as simple "black boxes" [114]. For an RF signal incident on one port, some fraction of the signal bounces back out of that port and some of it scatters and exits other ports. In the context of S-parameters, scattering refers to the way in which the traveling currents and voltages in a transmission line are affected when they meet a discontinuity caused by the insertion of a network into the transmission line. Many electrical properties of networks of components may be expressed using S-parameters, such as gain, return loss, reflection coefficient and amplifier stability. The S-matrix for an N-port device contains a N^2 coefficients, each one representing a possible input-output path. The first number in the subscript refers to the responding port, while the second number refers to the incident port. Therefore, for

the S-parameter subscripts "ij", j is the port that is excited (the input port), and "i" is the output port.
The pump-to-signal intensity modulation transfer (IMT) setups shown in Figs. 3.4 and **??** can be considered as two-port networks as schematically represented in Fig. A.1. a_i are denoting the incident power waves and b_j

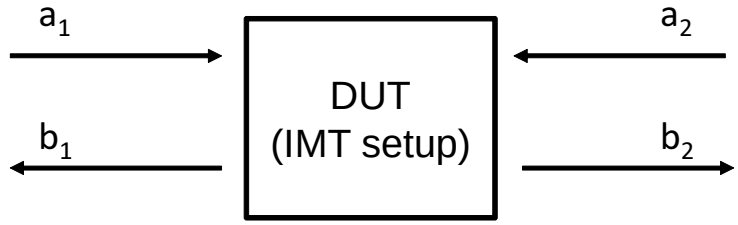

Figure A.1: Schematic of a two-port device. DUT: Device under test.

the reflected power waves, for $i, j = 1, 2$. The S-matrix for the two-port device is thus expressed as

$$\begin{pmatrix} b_1 \\ b_2 \end{pmatrix} = \begin{pmatrix} S_{11} & S_{12} \\ S_{21} & S_{22} \end{pmatrix} \begin{pmatrix} a_1 \\ a_2 \end{pmatrix}, \tag{A.1}$$

where

- S_{11} is the input port voltage reflection coefficient
- S_{12} is the reverse voltage gain
- S_{21} is the forward voltage gain
- S_{22} is the output port voltage reflection coefficient.

To measure S_{11}, a signal at port one is injected and its reflected signal is measured. In this case, no signal is injected into port 2, so $a_2 = 0$; during all laboratory S-parameter measurements, only one signal at a time is injected. The other S-parameters, S_{ij} are measured in a similar way, injecting a signal only at the port j and measuring the port i.

A.2 Modulation index calculation

The S-parameter used for the calculation of the modulation index m is S_{21}, since the power was injected at the port one of the device (Mach-Zehnder modulator) and the output power was measured at the port two,

corresponding to the FOPA output for the signal modulation index m_s or the Mach-Zehnder modulator output for the pump modulation index m_p. The two cases are shown schematically in Fig. A.2. The average

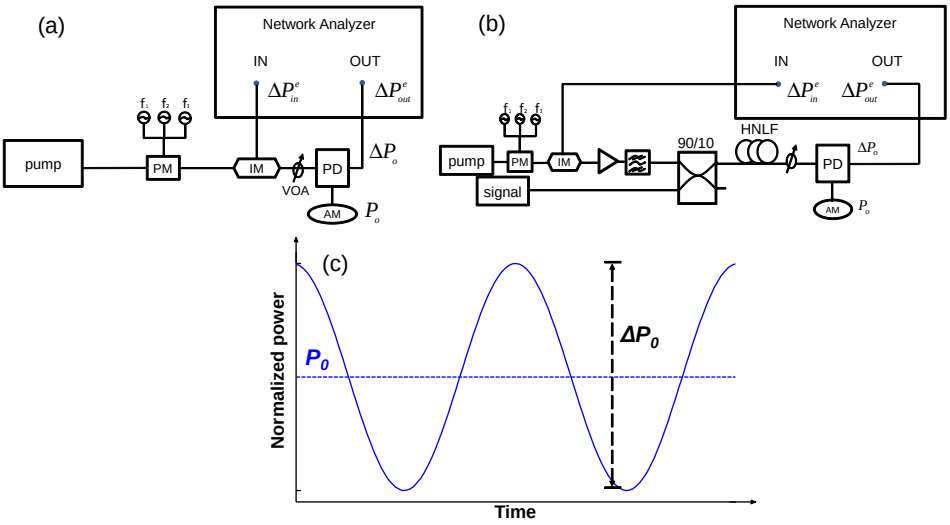

Figure A.2: Schematic of the setup for the measurements of (a) pump modulation index and (b) signal modulation index. PM: phase modulator; IM: intensity modulator; EDFA: erbium-doped fiber amplifier; HNLF: highly nonlinear fiber; VOA: variable optical attenuator; PD: photodiode; 90/10: 10 dB coupler. AM: ammeter. (c) Modulated signal or pump powers as a function of time.

optical power P_0 is calculated from the photocurrent I_{pd}, measured by means of an ammeter, through the relation $P_0 = I_{pd}/\eta$, where η is the photodiode responsivity. The peak-to-peak optical output power variation ΔP_o is calculated by S_{21} measured by the NA. The electrical input power level ΔP^e_{in} is set in the NA in order to have the amount of modulation desired. In case of $m_p = 0.01$, the input power ΔP^e_{in} was set to to -18dBm. This value was obtained by measuring the modulation index varying ΔP^e_{in} until the 1% modulation was reached. Based on the selected value for ΔP^e_{in}, the NA displays the S_{21} value as a function of frequency by considering the relation

$$S_{21} = \frac{b_2}{a_1} = \frac{\Delta P^e_{out}}{\Delta P^e_{in}} \tag{A.2}$$

valid when the port two is terminated in a load identical to the system impedance, for which b_2 will be totally absorbed making a_2 equal to zero.

To obtain an expression for the modulation index depending on S_{21}, it is useful to consider the optical power expressed as follows

$$P = P_o + \Delta P_o = (1 + m)P_o, \tag{A.3}$$

and the relation between electrical and optical powers

$$\Delta P^e = \eta^2 \Delta P_o R, \tag{A.4}$$

$$P_o = \sqrt{\frac{P^e}{\eta^2 R}} = \sqrt{\frac{R I_{pd}^2}{\eta^2 R}} = \frac{I_{pd}}{\eta}, \tag{A.5}$$

where R is the value of the system impedance, typically 50 or 75 Ω, and η is the photodiode responsivity. Considering all the equations, the modulation index can be obtained in terms of the output electrical powers as

$$m = \frac{\Delta P_o}{P_o} = \sqrt{\frac{\Delta P_{out}^e}{R I_{pd}^2}}. \tag{A.6}$$

Therefore, substituting the electrical output power of Eq. A.2 in Eq. A.6, the modulation index is calculated from S_{21} as follows

$$m = \sqrt{\frac{S_{21} \Delta P_{in}^e}{R I_{pd}^2}}. \tag{A.7}$$

It is important to notice that the value for ΔP_{in}^e is known and for the NA (Agilent HP8722c) employed the impedance is 50 Ω. Usually, the NA needs to be calibrated to be sure that the absolute values correspond to the selected values. However, since the intensity modulation coefficient ρ is defined as the ratio between the signal and pump modulation indices, all the parameters apart from the measured S_{21} and I_{pd} can be neglected. Moreover, if the photocurrent is kept constant in order to avoid a dependence of the results on the photodiode response, the modulation index depends only on the ratio between the signal and pump S_{21} parameters.

Acronyms

AQN amplified quantum noise

ASE amplified spontaneous emission

CW continuous wave

CFBG chirped fiber Bragg grating

DCF dispersion compensating fiber

DSF dispersion shifted fiber

DSF-HNLF dispersion shifted highly nonlinear fiber

EDF erbium-doped fiber

EDFA erbium-doped fiber amplifier

F8L figure-of-eight laser

FBG fiber Bragg grating

FOD fourth-order dispersion

FOPA fiber optical parametric amplifier

FOPCPA fiber optical parametric chirped pulse amplification

FWHM full-width at half maximum

FWM four-wave mixing

GVD group-velocity dispersion

HNLF highly nonlinear fiber

IM intensity modulation

IMT intensity modulation transfer

MI modulation instability

NA network analyzer

NALM nonlinear amplifying loop mirror

NF noise figure

OCPA optical chirped pulse amplification

OPCPA optical parametric chirped pulse amplification

OSA optical spectrum analyzer

OSNR optical signal-to-noise ratio

OTDM optical time division multiplexed

PC polarization controller

PD photodiode

PI-FOPA phase-insensitive fiber optical parametric amplifier

RADAR radio detection and ranging

RF radio-frequency

RIN relative intensity noise

RMS root mean square

SAM self-amplitude modulation

SBS stimulated Brillouin scattering

SHG second harmonic generation

SPM self-phase modulation

SRS stimulated Raman scattering

SSFM split step Fourier method

SSMF standard single mode fiber

TBP time-bandwidth product

TBPF tunable optical bandpass filter

THG third harmonic generation

TLS tunable laser source

TOD third-order dispersion

VOA variable optical attenuator

WDM wavelength division multiplexing

XPM cross-phase modulation

ZDW zero-dispersion wavelength

Bibliography

[1] E. Desurvire, "Erbium-Doped Fiber Amplifiers: Principles and Applications". Wiley, 1994.

[2] R. H. Stolen, "Phase-Matched-Stimulated Four-Photon Mixing in Silica-Fiber Waveguides," *Journal of Quantum Electronics*, vol. Q-E 11, no. 3, 100–103, 1975.

[3] J. Hansryd and P. A. Andrekson , "Broad-Band Continuous-Wave-Pumped Fiber Optical Parametric Amplifier with 49-dB Gain and Wavelength-Conversion Efficiency," *Journal of Quantum Electronics*, vol. 13, no. 3, 194–196, 2001.

[4] M. W. Lee, T. Sylvestre, M. Delqué, A. Kudlinski, A. Mussot, J.-F. Gleyze, A. Jolly, and H. Maillotte, "Demonstration of an All-Fiber Broadband Optical Parametric Amplifier at 1 μm," *Journal of Lightwave Technology*, vol. 28, no. 15, 2173–2178, 2010.

[5] J. E. Sharping, "Microstructure Fiber Based Optical Parametric Oscillators," *Journal of Lightwave Technology*, vol. 26, no. 14, 2184–2191, 2008.

[6] R. Tang, J. Lasri, P. Devgan, J. E. Sharping and P. Kumar, "Microstructure-Fibre-Based Optical Parametric Amplifier with Gain Slope of $\sim$ 200dB/W/km in the Telecom Range," *Electronics Letters*, vol. 39, no. 2, 195–196, 2003.

[7] R. Tang, J. Lasri, P. Devgan, J. E. Sharping and P. Kumar, "Tunable Parametric All-Fiber Short-Wavelength IR Transmitter," *Journal of Lightwave Technology*, vol. 28, no. 4, 443–447, 2010.

[8] G. P. Agrawal, *Nonlinear Fiber Optics* 4th edition. Academic Press, 2007.

[9] T. Torounidis, P. Andrekson and B.-E. Olsson, "Fiber-optical parametric amplifier with 70-dB gain," *IEEE Photonics Technology Letters*, vol. 18, no. 10, 1194–1196, 2006.

[10] G. Kalogerakis, K. Shimizu, M. E. Marhic, K. K.-Y. Wong, K. Uesaka and L. G. Kazovsky, "High-Repetition-Rate Pulsed-Pump Fiber OPA for Amplification of Communication Signals," *Journal of Lightwave Technology*, vol. 24, no. 8, 3021–3027, 2006.

[11] T. Torounidis and P. A. Andrekson, "Broadband Single-Pumped Fiber-Optic Parametric Amplifiers," *IEEE Photonics Technology Letters*, vol. 19, no. 9, 650–652, 2007.

[12] J. M. Chavez Boggio, S. Moro, E. Myslivets, J. R. Windmiller, N. Alic, and S. Radic, "155-nm Continuous-Wave Two-Pump Parametric Amplification," *IEEE Photonics Technology Letters*, vol. 21, no. 10, 612–614, 2009.

[13] J.M. Chavez Boggio, C. Lundström, J. Yang, H. Sunnerud and P.A. Andrekson , "Double-pumped FOPA with 40 dB flat gain over 81 nm bandwidth ," *European Conference and Exposition on Optical Communications (ECOC) 2010*, paper Tu.4.D.3, 2010.

[14] P.L. Voss and P. Kumar, "Raman-induced noise figure limit for χ^3 parametric amplifiers," *Optics Letters*, vol.29, no. 5, 445–447, 2004.

[15] C. J. McKinstrie and S. Radic, "Phase-sensitive amplification in a fiber," *Optics Express*, vol. 12, no. 20, 4973–4979, 2004.

[16] P. Andrekson, "Phase Sensitive Fiber Optic Parametric Amplifiers," *European Conference and Exposition on Optical Communications (ECOC) 2011*, Th. 11, 2011.

[17] Z. Tong, C. Lundström, P. A. Andrekson, C. J. McKinstrie, M. Karlsson, D. J. Blessing, E. Tipsuwannakul, B. J. Puttnam, H. Toda and L. Grüner-Nielsen, "Towards ultrasensitive optical links enabled by low-noise phase-sensitive amplifiers", *Nature Photonics*, vol. 5, 430–436, 2011.

[18] D. Caucheteur, E. Bigourd, E. Hugonnot, P. Szriftgiser, A. Kudlinski, M. Gonzalez-Herraez and A. Mussot, "Experimental demonstration of optical parametric chirped pulse amplification in optical fiber," *Optics Letters*, vol. 35, no. 11, 1786–1788, 2010.

[19] Y. Zhou, K. K. Y. Cheung, P. C. Chui, and K. K. Y. Wong, "Experimental demonstration of fiber optical parametric chirped-pulse amplification," *SPIE Proceedings*, 7582, 75820T, 2010.

[20] M. Hanna, F. Druon and P. Georges, "Fiber optical parametric chirped-pulse amplification in the femtosecond regime," *Optics Express*, vol. 14, no. 7, 2783–2790, 2006.

[21] A. Mussot, A. Kudlinski, P. Beaure d'Augères, and E. Hugonnot, "Amplification of ultra-short optical pulses in a two-pump fiber optical parametric chirped pulse amplifier," *Optics Express*, vol. 21, no. 10, 12197–12203, 2013.

[22] D. Bigourd, L. Lago, A. Mussot, A. Kudlinski, J.-F. Gleyze and E. Hugonnot, "High-gain fiber, optical-parametric, chirped-pulse amplification of femtosecond pulses at 1 μm," *Optics Letters*, vol. 35, no. 20, 3480–3482, 2010.

[23] Y. Zhou, Q. Li, K. K. Y Cheung, S. Yang, P. C. Chui and K. K. Y. Wong, "All-fiber based ultrashort pulse generation and chirped pulse amplification through parametric processes," *IEEE Photonics Technology Letters*, vol. 22, 1330–1332, 2010.

[24] H. C. Hansen Mulvad, L. K. Oxenløwe, M. Galili, A. T. Clausen, L. Grüner-Nielsen and P. Jeppesen, "1.28 Tbit/s single-polarisation serial OOK optical data generation and demultiplexing," *Electronics Letters*, vol. 45, no. 5, 280–281, 2009.

[25] H. C. Hansen Mulvad, M. Galili, L. K. Oxenløwe, H. Hu, A. T. Clausen, J. B. Jensen, C. Peucheret and P. Jeppesen, "Demonstration of 5.1 Tbit/s data capacity on a single-wavelength channel," *Optics Express*, vol. 18, no. 2, 1438–1443, 2010.

[26] T. Richter, E. Palushani, C. Schmidt-Langhorst, R. Ludwig, L. Molle, M. Nölle, and C. Schubert, "Transmission of single-channel 16-QAM data signals at Terabaud symbol rates," *Journal of Lightwave Technology*, vol. 30, no. 4, 504–511, 2012.

[27] I. N. Duling III, "All-fiber ring soliton laser mode locked with a nonlinear mirror," *Optics Express*, vol. 16, no. 8, 539–541, 1991.

[28] M. E. Marhic, *Fiber Optical Parametric Amplifiers, Oscillators and Related Devices.* Cambridge University Press, 2008.

[29] S. Yang, K. K. Y. Wong, M. Chen and S. Xie, "Fiber optical parametric oscillator based on highly nonlinear dispersion-shifted fiber," *Frontiers of Optoelectronics*, vol. 6, no. 1, 25–29, 2013.

[30] J. Hansryd, P. A. Andrekson, M. Westlund, J. Li and P. Hedekvist, "Fiber-based optical parametric amplifiers and their applications," *IEEE Journal of Selected Topics in Quantum Electronics*, vol. 8, no. 3, 506–520, 2002.

[31] R. Slavik *et. al*, "All-optical phase and amplitude regenerator for next-generation telecommunications systems," *Nature Photonics*, vol. 4, 690–695, 2010.

[32] C. Peucheret, M. Lorenzen, J. Seoane, D. Noordegraaf, C. V. Nielsen, L. Grüner-Nielsen and K. Rottwitt, "Amplitude regeneration of RZ-DPSK signals in single-pump fiber-optic parametric amplifiers," *IEEE Photonics Technology Letters*, vol. 21, no. 13, 872–874, 2009.

[33] X. Guo, K. P. Lei, X. Fu, H. K. Tsang and C. Shu, "Amplitude Regeneration of 80-Gb/s Polarization-Multiplexed RZ-DPSK Signals in a Dual-Orthogonal-Pump Fiber Optical Parametric Amplifier," *Optical Fiber Communication Conference (OFC) 2013*, paper OTu2D, 2013.

[34] F. Futami, R. Okabe, S. Ono, S. Watanabe, R. Ludwig, C. Schmidt-Langhorst and C. Schubert, "All-Optical Amplitude Noise Suppression of 160-Gb/s OOK and DPSK Data Signals Using a Parametric Fiber Switch," *Optical Fiber Communication Conference (OFC) 2007*, paper OThB, 2007.

[35] J. Kakande, A. Bogris, R. Slavík, F. Parmigiani, D. Syvridis, P. Petropoulos and D. J. Richardson, "First demonstration of all-optical QPSK signal regeneration in a novel multi-format phase sensitive amplifier," *European Conference and Exposition on Optical Communications (ECOC) 2010*, paper PD3.3, 2010.

[36] J. Kakande, A. Bogris, R. Slavík, F. Parmigiani, D. Syvridis, P. Petropoulos, D. Richardson, M. Westlund and M. Sköld,, "QPSK phase and amplitude regeneration at 56 Gbaud in a novel idler-free non-degenerate phase sensitive amplifier," *Optical Fiber Communication Conference (OFC) 2011*, paper OMT4, 2011.

[37] J. Hansryd and P. A. Andrekson, "O-TDM Demultiplexer with 40-dB

Gain Based on a Fiber Optical Parametric Amplifier," *IEEE Photonics Technology Letters*, vol. 13, no. 7, 732–734, 2001.

[38] G.-W. Lu, K. S. Abedin, T. Miyazaki, M. E. Marhic, "RZ-DPSK OTDM demultiplexing using fibre optical parametric amplifier with clock-modulated pump," *Electronics Letters*, vol. 45, no. 4, 221–222, 2009.

[39] J. Boggio, A. Guimarães, F. Callegari, J. Marconi, M. Rocha, M. debarros, and H. Fragnito, "Parametric amplifier for mid-span phase conjugation with simultaneous compensation of fiber loss and chromatic dispersion at 10 Gb/s," *Microwave and Optical Technology Letters*, vol. 42, no. 6, pp.503–505, 2004.

[40] B.-P. Kuo, E. Myslivets, A. O. Wiberg, S. Zlatanovic, C.-S. Brès, S. Moro, F. Gholami, A. Peric, N. Alic and S. Radic, "Transmission of 640-Gb/s RZ-OOK channel over 100-km SSMF by wavelength-transparent conjugation," *Journal of Lightwave Technology*, vol. 29, no. 4, 516–523, 2011.

[41] Y. R. Shen, *The Principles of Nonlinear Optics* 1st edition. Wiley, 1984.

[42] R. H. Stolen and C. Lin, "Self-phase-modulation in silica optical fibers," *Physical Review A*, vol. 17, no. 4, 1448–1453, 1978.

[43] A. Hasegawa and F. Tappert, "Transmission of stationary nonlinear optical pulses in dispersive dielectric fibers. I. Anomalous dispersion," *Applied Physics Letters*, vol. 23, no. 3, 142–144, 1973.

[44] A. Boskovic, S. V. Chernikov, J. R. Taylor, L. Grüner-Nielsen and O. A. Levring, "Direct continuous-wave measurement of n_2 in various types of telecommunication fiber at 1.55μm," *Optics Letters*, vol. 21, no. 24, 1966–1968, 1996.

[45] V. M. Mashinsky, V. B. Neustruev, V. V. Dvoyrin, S. A. Vasiliev, O. I. Medvedkov, I. A. Bufetov, A. V. Shubin, E. M. Dianov, A. N. Guryanov, V. F. Khopin, and M. Yu. Salgansky, "Germania-glass-core silica-glass-cladding modified chemical-vapor deposition optical fibers: optical losses, photorefractivity, and Raman amplification," *Optics Letters*, vol. 29, no. 22, 2596–2598, 2004.

[46] Evgeny M. Dianov and Valery M. Mashinsky, "Germania-Based Core

Optical Fibers," *Journal of Lightwave Technology*, vol. 23, no. 11, 3500–3508, 2005.

[47] Masaaki Hirano, Tetsuya Nakanishi, Toshiaki Okuno, and Masashi Onishi, "Silica-Based Highly Nonlinear Fibers and Their Application," *IEEE Journal of Selected Topics in Quantum Electronics*, vol. 15, no. 1, 3500–3508, 2009.

[48] Lars Grüner-Nielsen, Søren Herstrøm, Sonali Dasgupta, David Richardson, Dan Jakobsen, Carl Lundström, Peter A.Andrekson, Martin E.V.Pedersen, and Bera Pálsdóttir, "Silica-Based Highly Nonlinear Fibers with a High SBS Threshold," *IEEE Photonics Society Winter Topical Meeting (WTM) 2011*, pages 171–172, 2011.

[49] M. E. Marhic, N. Kagi, T.-K. Chiang, and L. G. Kazovsky, "Broadband fiber optical parametric amplifiers," *Optics Letters*, vol. 21, no. 8, 2596–2598, 1996.

[50] M. E. Marhic, Y. Park, F. S. Yang and L. G. Kazovsky, "Broadband fiber-optical parametric amplifiers and wavelength converters with low-ripple Chebyshev gain spectra," *Optics Letters*, vol. 21, no. 17, 1354–1356, 1996.

[51] K. Inoue and T. Mukai, "Signal wavelength dependence of gain saturation in a fiber optical parametric amplifier," *Optics Letters*, vol. 26, no. 1, 10–12, 2001.

[52] G. B. Whitham, "Non-linear dispersive waves," *Proceedings of the Royal Society of London A*, vol. 283, no. 1393, 238–261, 1965.

[53] T. B. Benjamin and J. E. Feir, "The disintegration of wave trains on deep water," *Journal of Fluid Mechanics*, vol. 27, no. 3, 417–430, 1967.

[54] A. Hasegawa, "Theory and Computer Experiment on Self-Trapping Instability of Plasma Cyclotron Waves ," *Physics of Fluids*, vol. 15, no. 5, 870–881, 1972.

[55] L. A. Ostrovskii, "Electromagnetic waves in nonlinear media with dispersion," *Soviet Physics*, vol. 8, 1964.

[56] A. Hasegawa and W. F. Brinkman, "Tunable Coherent IR and FIR Sources Utilizing Modulational Instability," *Quantum Electronics Letters*, vol. QE-16, no. 7, 694–697, 1980.

[57] K. Tai, A. Hasegawa, and A. Tomita, "Observation of Modulational Instability in Optical Fibers," *Physical Review Letter*, vol. 56, no. 2, 135–139, 1986.

[58] G. P. Agrawal, *Nonlinear Fiber Optics* 2nd edition. Academic Press, 1995.

[59] A. Hasegawa, "Generation of a train of soliton pulses by induced modulational instability in optical fibers," *Optics Letters*, vol. 9, no. 7, 288–290, 1984.

[60] Z. Su, X. Zhu, and W Sibbett, "Conversion of femtosecond pulses from the 1.5- to the 1.3-μm region by self-phase-modulation-mediated four-wave mixing," *Journal of the Optical Society of America B*, vol. 10, no. 6, 1050–1053, 1993.

[61] A. Chraplyvy, "Limitations on Lightwave Communications Imposed by Optical-Fiber Nonlinearities," *Journal of Lightwave Technology*, vol. 8, no. 10, 1548–1557, 1990.

[62] Q. Lin and G. P. Agrawal, "Vector theory of four-wave mixing: polarization effects in fiber-optic parametric amplifiers," *Journal of the Optical Society of America B*, vol. 21, no. 6, 1216–1224, 2004.

[63] M. Karlsson, "Four-wave mixing in fbers with randomly varying zero-dispersion wavelength," *Journal of the Optical Society of America B*, vol. 15, no. 8, 1216–1224, 1998.

[64] J.M. Chavez Boggio, F.A. Callegari, J.D. Marconi, A. Guimarães and H.L. Fragnito, "Influence of zero dispersion wavelength variations on cross-talk in single-pumped fiber optic parametric amplifiers," *Optics Communications*, vol. 242, no. 8, 471–478, 2004.

[65] J.M. Eiselt, R. M. Jopson and R. H. Stolen, "Nondestructive position-resolved measurement of the zero-dispersion wavelength in an optical fiber," *Journal of Lightwave Technology*, vol. 15, no. 1, 135–143, 1997.

[66] M. E. Marhic, K. K. Y. Wong, G. Kalogerakis, and L. G. Kazovsky, "Recent advances in the design and experimental implementation of fiber optical parametric amplifiers," *SPIE Proceedings*, vol. 5623, 691–704, 2005.

[67] A. Mussot, E. Lant, A. Durécu-Legrand, C. Simonneau, D. Bayart, T. Sylvestre and H. Maillotte, "Zero-dispersion wavelength mapping

in short single-mode optical fibers using parametric amplification," *IEEE Photonics Technology Letters*, vol. 18, no. 1, 22–24, 2006.

[68] T. Torounidis, H. Sunnerud, P. O. Hedekvist and P. A. Andrekson, "Amplification of WDM Signals in Fiber-Based Optical Parametric Amplifiers," *IEEE Photonics Technology Letters*, vol. 15, no. 8, 1061–1063, 2003.

[69] N. El Dahdah, D. S. Govan, M. Jamshidifar, N. J. Doran, and M. E. Marhic, "1 Tb/s DWDM Long-Haul Transmission Employing a Fiber Optical Parametric Amplifier," *IEEE Photonics Technology Letters*, vol. 22, no. 5, 1171–1173, 2010.

[70] N. El Dahdah, D. S. Govan, M. Jamshidifar, N. J. Doran, and M. E. Marhic, "Optically Powered WDM Signal Transmission System With Distributed Parametric Amplification," *IEEE Photonics Technology Letters*, vol. 22, no. 16, 1232–1234, 2010.

[71] A. Kobyakov, M. Sauer and D. Chowdhury, "Stimulated Brillouin Scattering in Optical Fibers," *Advances in Optics and Photonics*, vol. 2, no. 1, 1–59, 2009.

[72] K.i Shiraki, M. Ohashi and M. Tateda, "SBS Threshold of a Fiber with a Brillouin Frequency Shift Distribution," *Journal of Lightwave Technology*, vol. 14, no. 1, 50–57, 1996.

[73] J. B. Coles, B. P.-P. Kuo, N. Alic, S. Moro, C.-S. Bres, J. M. Chavez Boggio, P.A. Andrekson, M. Karlsson and S. Radic, "Bandwidth-efficient phase modulation techniques for Stimulated Brillouin Scattering suppression in fiber optic parametric amplifiers," *Optics Express*, vol. 18, no. 17, 18138–18150, 2010.

[74] A. Kobyakov, S. Kumar., D. Q. Chowdhury, A. B. Ruffin, M. Sauer, S. R. Bickham and R. Mishra, "Design concept for optical fibers with enhanced SBS threshold," *Optics Express*, vol. 13, no. 14, 5338–5346, 2005.

[75] S. Bickham, A. Kobyakov and S. Li, "Nonlinear Optical Fibers with Increased SBS Thresholds," *Optical Fiber Communication Conference (OFC) 2006*, paper OTuA3, 2006.

[76] L. Grüner-Nielsen, S. Dasgupt, M. D. Mermelstein, D. Jakobsen, S. Herstrøm, M. E. V. Pedersen, E. L. Lim, S. Alam, F. Parmigiani, D. Richardson and B. Pálsdóttir, "A Silica Based Highly Nonlinear Fibre

with Improved Threshold for Stimulated Brillouin Scattering," *European Conference and Exposition on Optical Communications (ECOC) 2010*, paper Tu.4.D.3, 2010.

[77] N. Yoshizawa and T. Imai, "Stimulated brillouin scattering suppression by means of applying strain distribution to fiber with cabling," *Journal of Lightwave Technology*, vol. 11, no. 10, 1518–1522, 1993.

[78] M. Takahashi, M. Tadakuma and T. Yagi, "Dispersion and brillouin managed HNLFs by strain control techniques," *Journal of Lightwave Technology*, vol. 28, no. 1, 59–64, 2010.

[79] P. Kylemark, P. O. Hedekvist, H. Sunnerud, M. Karlsson and P. A. Andrekson, "Noise Characteristics of Fiber Optical Parametric Amplifiers," *Journal of Lightwave Technology*, vol. 22, no. 2, 409–416, 2004.

[80] G. Kalogerakis, K. Shimizu, M. E. Marhic, K. K.-Y. Wong, K. Uesaka and L. G. Kazovsky, "High-Repetition-Rate Pulse-Pump Fiber OPA for Amplification of Communication Signals," *Journal of Lightwave Technology*, vol. 24, no. 8, 3021–3027, 2006.

[81] M. E. Marhic, G. Kalogerakis, K. K. Wong and L. G. Kazovsky, "Pump-to-signal transfer of low-frequency intensity modulation in fiber optic parametric amplifiers," *Journal of Lightwave Technology*, vol. 23, no. 3, 1049–1055, 2005.

[82] A. Durécu-Legrand, C. Simonneau, D. Bayart, A. Mussot, T. Sylvestre, E. Lantz and H. Maillotte, "Investigation of Electrical Noise Figure for Fiber Optical Parametric Amplifiers," *Optical Fiber Communication Conference (OFC) 2005*, paper OWN7, 2005.

[83] P. Kylemark, P. O. Hedekvist, H. Sunnerud, M. Karlsson and P. A. Andrekson, "Noise Characteristics of Fiber Optical Parametric Amplifiers," *Journal of Lightwave Technology*, vol. 22, no. 2, 1255–1257, 2006.

[84] K. Inoue, "Optical level equalisation based on gain saturation in fibre optical parametric amplifier," *Electronics Letters*, vol. 36, no. 12, 1016–1017, 2000.

[85] Z. Lali-Dastjerdi, V. Cristofori, T. Lund-Hansen, K. Rottwitt, M.l Galili and C. Peucheret, "Pump-To-Signal Intensity Modulation

Transfer Characteristics in FOPAs: Modulation Frequency and Saturation Effect," *Journal of Lightwave Technology*, vol. 30, no. 18, 3061–3067, 2012.

[86] Z. Tong, A. Bogris, M. Karlsson and P. A. Andrekson, "Full characterization of the signal and idler noise figure spectra in single-pumped fiber optical parametric amplifiers," *Optics Express*, vol. 18, no. 3, 2884–2893, 2010.

[87] P. Kylemark, M. Karlsson and P. A. Andrekson, "Gain and wavelength dependence of the noise figure in fiber optical parametric amplification," *IEEE Photonics Technoly Letters*, vol. 18, no. 11, 1255–1257, 2006.

[88] F. Yaman, G. P. Agrawal and S. Radic, "Pump-noise transfer in dual-pump fiber-optic parametric amplifiers: walk-off effects," *Optics Letters*, vol. 30, no. 9, 1048–1050, 2005.

[89] V. Cristofori, T. Lund-Hansen, C. Peucheret and K. Rottwitt, "Experimental Investigation of Pump-to-Signal Noise Transfer in One Pump Phase Insensitive Fibre Optic Parametric Amplifiers". In *International Conference on Transparent Optical Networks (ICTON) 2011*, paper Tu.C1.4, 2011.

[90] P. Kylemark, H. Sunnerud, M. Karlsson and P. A. Andrekson, "Semi-Analytic Saturation Theory of Fiber Optical Parametric Amplifiers," *Journal of Lightwave Technology*, vol. 24, no. 9, 3471–3479, 2006.

[91] H. Steffensen, J. R. Ott, K. Rottwitt and C. J. McKinstrie, "Full and semi-analytic analyses of two-pump parametric amplification with pump depletion," *Optics Express*, vol. 19, no. 7, 6648–6656, 2011.

[92] V. Cristofori, Z. Lali-Dastjerdi,T. Lund-Hansen, C. Peucheret and K. Rottwitt, "Experimental investigation of saturation effect on pump-to-signal intensity modulation transfer in single-pump phase-insensitive fiber optic parametric amplifier," *Journal of the Optical Society of America B*, vol. 30, no. 4, 884–888, 2013.

[93] Z. Lali-Dastjerdi, K. Rottwitt, M. Galili and C. Peucheret, "Asymmetric gain-saturated spectrum in fiber optical parametric amplifiers," *Optics Express*, vol. 20, no. 14, 15530–15539, 2012.

[94] A. M. Weiner, "Ultrafast Optics". Wiley, 2009.

[95] B. K. Garside and T. K. Lim, "Laser mode locking using saturable absorbers," *Journal of Applied Physics*, vol. 44, no. 5, 2335-2342, 1973.

[96] U. Keller, K.J. Weingarten, F.X. Kartner, D. Kopf, B. Braun, I.D. Jung, R. Fluck, C. Honninger, N. Matuschek and J. Aus der Au, "Semiconductor saturable absorber mirrors (SESAM's) for femtosecond to nanosecond pulse generation in solid-state lasers," *IEEE Journal of Selected Topics in Quantum Electronics*, vol. 2, no. 3, 435–453, 1996.

[97] M. J. Potasek and G. P. Agrawal, "Self-amplitude-modulation of optical pulses in nonlinear dispersive fibers", *Physical Review A*, vol. 36, no. 8, 3862–3868, 1987.

[98] M. S. Stix and E. P. Ippen, "Pulse Shaping in Passively Mode-Locked Ring Dye Lasers," *Journal of Quantum Electronics*, vol. Q-E 19, no. 4, 520–525, 1983.

[99] N. J. Doran and D. Wood, "Nonlinear-optical loop mirror," *Optics Letters*, vol. 13, no. 1, 56–58, 1988.

[100] K. J. Blow, N. J. Doran and B. K. Nayar, "Experimental demonstration of optical soliton switching in an all-fiber nonlinear Sagnac interferometer," *Optics Letters*, vol. 14, no. 14, 754–756, 1989.

[101] O. Pottiez, B. Ibarra-Escamilla and E. A. Kuzin, "High-Energy Pulses from a Figure 8 Fiber Laser with Normal Net Dispersion," *Laser Physics*, vol. 19, no. 2, 371–376, 2009.

[102] X. H. Li, Y. S. Wang, W. Zhao, W. Zhang, Z. Yang, X. H. Hu, H. S. Wang, X. L. Wang, Y. N. Zhang, Y. K. Gong, C. Li and D. Y. Shen "All-Normal Dispersion, Figure-Eight, Tunable Passively Mode-Locked Fiber Laser with an Invisible and Changeable Intracavity Bandpass Filte," *Laser Physics*, vol. 21, no. 5, 940–944, 2011.

[103] L. Grüner-Nielsen, B. Pálsdóttir, "Highly nonlinear fibers for very wideband supercontinuum generation," *SPIE Proceedings*, vol. 6873, 68731B, 2008.

[104] K. Tamura, L. E. Nelson, H. A. Haus and E. P. Ippen, "Soliton versus nonsoliton operation of fiber ring lasers," *Applied Physics Letters*, vol. 64, no. 2, 149–151, 1994.

[105] M. L. Dennis and I. N. Duling III, "Role of dispersion in limiting pulse width in fiber lasers ," *Applied Physics Letters*, vol. 62, no. 23, 2911–2913, 1993.

[106] A. Dubietis, R. Butkus and A. P. Piskarskas, "Trends in Chirped Pulse Optical Parametric Amplification," *IEEE Journal of Selected Topics in Quantum Electronics*, vol. 12, no. 2, 163–172, 2006.

[107] D. Strickland and G. Mourou, "Compression of amplified chirped optical pulses," *Optics Communications*, vol. 56, no. 3, 219–221, 1985.

[108] A. Dubietis, G. Jonušauskas and A. Piskarskas, "Compression of amplified chirped optical pulses," *Optics Communications*, vol. 88, no. 4–6, 437–440, 1992.

[109] D. Bigourd, L. Lago, A. Kudlinski, E. Hugonnot and A. Mussot, "Dynamics of fiber optical parametric chirped pulse amplifiers," *Journal of the Optical Society of America B*, vol. 28, no. 11, 2848–2854, 2011.

[110] C. Manzoni, J. Moses, F. X. Kärtner and G. Cerullo, "Excess quantum noise in optical parametric chirped-pulse amplification," *Optics Express*, vol. 19, no. 9, 8357–8366, 2011.

[111] F. Eichhorn, R. K. Olsson, J. C. D. Buron, L. Grüner-Nielsen, J. E. Pedersen and P. U. Jepsen, "Optical fiber link for transmission of 1-nJ femtosecond laser pulses at 1550 nm," *Optics Express*, vol. 18, no. 7, 6978–6987, 2010.

[112] A. Mussot, A. Kudlinski1 and E. Hugonnot, "Twofold enhancement of the gain bandwidth in two pumps fiber optical parametric chirped pulse amplifiers". In *Advanced Photonics Congress (2012)*, paper JM5A.18, 2012.

[113] R. H. Dicke, "A Computational Method Applicable to Microwave Networks," *Journal of Applied Physics*, vol. 18, no. 10, 873-878, 1947.

[114] M. E. Van Valkenburg, *Circuit theory: foundations and classical contributions.* Dowden, Hutchinson & Ross, 1974.